ICFO-INSTITUT DE CIÈNCIES FOTÒNIQUES &

UPC-UNIVERSITAT POLITÈCNICA DE CATALUNYA

Mid-Infrared Surface Sensing Based on Two-Dimensional Materials

Nestor Jr. Bareza

Dissertation Advisors:
Prof. Valerio Pruneri
Dr. Bruno Paulillo

PhD Dissertation – 2022

In loving memory of my father,

Nestor A. Bareza

Abstract

Mid-infrared (mid-IR) spectroscopy in the wavelength region between 2 and 20 μm is a powerful technique to identify vibrational absorption signatures of molecules, finding in this way extensive applications in healthcare, environmental monitoring, and chemical analysis. Enhanced IR light-molecules interactions can be achieved by exploiting nanostructured surfaces supporting polaritons – hybrid excitations of light and dipolar elements of matter. Recently, polaritons of two-dimensional van der Waals (2D-vdW) materials unveiled a vibrant playground for mid-IR spectroscopy as they possess remarkable properties such as light trapping at deep nanoscale. This dissertation aims to investigate 2D-vdW materials for technological sensing applications. Hence, we explore the mid-IR sensing performance of nanostructures of widely studied 2D-vdW crystals: graphene (the pioneering vdW material with tunable plasmon polaritons) and hexagonal boron nitride (*hBN*, sustaining ultralow-loss phonon polaritons). Relevant functionalization layers, such as polymer adsorber and antibodies, are combined with the 2D-vdW nanostructures to create gas and bio-molecular sensors, respectively.

Here, we present three main experimental works of 2D-vdW-based mid-IR molecular sensing. First, we investigate the CO_2 detection using graphene nanoribbons functionalized with ultrathin CO_2-chemisorbing polyethylenimine (PEI). The localized surface plasmon resonance (LSPR) of graphene is modulated by varying CO_2 gas concentration, whose substantial shifts are influenced by the reversible PEI-induced doping of graphene. Second, we examine the phonon-enhanced CO_2 detection of hBN nanoresonators functionalized with thin PEI layer. The phonon-polariton resonance is modulated by varying CO_2 levels with high signal-to-noise ratio signals. Third, we present a quantitative bioassay by transducing different vitamin B12 target concentrations into LSPR shifts of bio-functionalized graphene nanostructures (subsequent addition of pyrene linkers and recombinant anti-vB12 antibody fragments). Additionally, we observed the same result-trends for the same bioassay using graphene nanostructures fabricated both by small-scale (i.e.,

electron beam lithography) and large-scale (i.e., nanoimprint lithography) methods.

Our proof-of-concept mid-IR sensing experiments show quantitative results for the detection of gas and biomarker with functionalized 2D-vdW nanostructures. The opportunity of combining the mid-IR spectroscopy with industrially large-scale 2D-vdW nanostructures (e.g., nanoimprinted GNH in this dissertation) would enable cost-effective technologies in future developments. This dissertation contributes to the field of 2D-vdW-based mid-IR spectroscopic sensors towards exploring novel designs and improved sensitivity, which eventually could lower the limit of detection for molecular analytes in various applications.

Resumen

La espectroscopia infrarroja de onda media (mid-IR en inglés) en el rango óptico entre 2 y 20 µm es una potente técnica para identificar las huellas vibracionales de las moléculas, permitiendo así su uso en múltiples aplicaciones como salud, monitoreo medioambiental y análisis químico. Aumentar las interacciones luz-molécula en el IR es posible explotando superficies nano-estructuradas que soportan polaritones – excitaciones hibridas entre la luz y dipolos en la materia. Recientemente, polaritones en materiales bidimensionales de van der Waals (2D-vdW) han revelado un escenario interesante para la espectroscopia en el mid-IR, ya que poseen propiedades remarcables como la de confinar la luz a escala nanométrica. Esta tesis pretende investigar materiales 2D-vdW para su uso tecnológico en aplicaciones de detección. De esta manera, exploramos el rendimiento de la detección en el mid-IR de nanoestructuras de cristales 2D-vdW ampliamente estudiados: grafeno (el material vdW pionero con plasmones-polaritones sintonizables) y el nitruro de boro hexagonal (hBN, que soporta fonones-polaritones con muy bajas perdidas). Capas adicionales para la funcionalización, como polímeros absorbentes y anticuerpos, son combinadas con las nanoestructuras 2D-vdW para crear sensores de gas y biomoleculares, respectivamente.

Aquí presentamos tres principales trabajos experimentales para la detección de moléculas con materiales 2D-vdW en el mid-IR. Primero, investigamos la detección de CO_2 usando nanoribons de grafeno funcionalizado con una capa ultrafina de polietilenimina (PEI), dada su quimisorción de CO_2. La resonancia de plasmón de superficie localizada (LSPR) del grafeno es modulada variando la concentración del CO_2, cuyos desplazamientos dependen de un efecto de dopaje quimico reversible inducido por el PEI. Después, examinamos la detección realzada de CO_2 con fonones a partir de nanoresonadores de hBN funcionalizados con una capa fina de PEI. La resonancia fonón-polaritón es modulada variando los niveles de CO_2 con una gran relación señal/ruido. Finalmente, presentamos un bioensayo cuantitativo a partir de la transducción de distintas concentraciones de vitamina B12 a desplazamientos de LSPR con nanoestructuras bio-funcionalizadas de grafeno (con la posterior adición de enlazadores de pireno y anticuerpos fragmentos de recombinante anti-vB12) Adicionalmente, observamos la misma tendencia de resultados

para el mismo bioensayo usando nanoestructuras de grafeno fabricadas con métodos no escalables (i.e., litografía por haz de electrones) y escalable (i.e., litografía por nanoimpresión).

Nuestras pruebas de concepto con experimentos de detección con luz mid-IR muestran resultados cuantitativos para la detección de gas y biomarcadores con nanoestructuras 2D-vdW funcionalizadas. La oportunidad de poder combinar la espectroscopia mid-IR con nanoestructuras de materiales 2D-vdW industrialmente escalables (ej., GNH via nanoimpresión en esta tesis) podrían permitir desarrollar tecnologías rentables en el futuro. Esta tesis pretende contribuir en el campo de los sensores para espectroscopia mid-IR basados en materiales 2D-vdW, explorando novedosos diseños y mejorando su sensibilidad, los cuales podrían eventualmente reducir el límite de detección para analitos moleculares en varias aplicaciones.

Acknowledgments

I decided to fly across continents to embark on a PhD journey in Spain. After years of battling through uncertain paths, here I stand, feeling extremely grateful to the countless people who inspired and supported me to reach this milestone.

I have my sincere gratitude to my supervisor **Valerio**, who emanates never-ending passion and dedication. Thank you for giving me the opportunity to be a part of the OPTO family and for allowing me to grow professionally with your support. I deeply appreciate your random knocks in the office to uplift our spirits by sharing your wisdom and funny stories.

To my other supervisor, **Bruno**, I am truly honored to have learned from you. Thank you for your generosity and kindness, especially for giving me trust and building my confidence. Our fruitful discussions always tickle the creativity and imagination to bring out the best possible research outcomes. Apart from being a brilliant mentor, I am fortunate to have you as an incredible friend.

I am grateful to the **committee members**, for providing your exceptional insights and for examining my thesis.

Many thanks to the post-docs who taught me invaluable skills: **Kavitha** for passing the throne of graphene activities and just radiating peaceful vibes, **Ewelina** for playing those biomolecular *Legos* up to N^{th} experiment and life conversations, and **Dani R.** for helping my initial sail in doing PhD.

I am indebted to our collaborators from *NanoGUNE*, *VTT*, *CSIC*, *ICMAB*, and *KSU*. It is a privilege to have those numerous extensive discussions that expanded my scientific horizons, especially **Rainer**, **Tarja**, **Tanya**, and **Marta**.

I acknowledge **Lisa Ruby** for patiently proofreading and for promptly reverting my thesis revisions.

Kudos to the *Surface* team with our weekly meetings – **Dani M.** for being such a super reliable friend, **Javi** for your infectious diligence, **Christina**, and **Iliyan**. I also appreciate my short participation in the LIM team – **Roland** for your attentive guidance, **Luc** for your occasional helps, **Robin**, **Matej** and **Alican**.

Thanks to the OPTO family: **Rinu** for the first person to really welcome me and all our laughs, **Mariela** for the shared strength and being a soldier of your inspiring stories, **Vahagn** for actively sharing your knowledge and for always cheering me up in NFL, **Rubi** as my pal for facing together same stages of PhD and bureaucracy

matters in Spain, **Alex** for being kind, our hikes and exploring Barcelona, **Rafael** for all the dinners and great conversations, **Juan R.** for all the fun, **Sofia** for being a cheerful friend, **Miriam** for the support with your graphene expertise, **Sandra**, **Rose**, **Alvaro**, **David**, **Cedric**, **Daniel**, **Ignacio**, **Seba**, **Goretti**, **Josellin**, **Alfredo**, **Marco**.

I am thankful to the warm community of ICFO – HR (**Anne** for welcoming me to your wonderful home, **Manuela**, **Ingrid** and **Mery**), Academic Affairs (**Rob** and **Laia**), Front desk, Maintenance (**Carlos** and **Nuria** for your substantial help with my gas sensing setup), Logistics (**Adrian**, *Kuya*!), IT, Travel, Purchasing, Electronics and Mechanical (**Xavi** for your design suggestions with my setups) workshops. I also have the great opportunity to work in cutting-edge laboratories – NFL (**Javi**, **Luis**, **Johann**, and **Paula** for all the trainings and wonderful support), PPL and Chemistry Lab (**Vittoria** for being my lab savior multiple times), Biology Lab, and NCL. I also appreciate all the talks in corridor/lab that makes working at ICFO extra light – Saúde o Tagay, **Marcelo**! **Sid** ikaw naman ang magtayo ng bandera natin, **Varun**, **Pandian**, **Gaurav**, **Catarina**, and a bunch of people I have missed to mention.

To my core support at ICFO: thanks for the gift of wonderful friendship and shared journey of ups and downs. **Andrew** and **Hitesh**, who would have thought that our common Spanish language class would bring us laughing along the streets of Athens and coasts of Malta. **Dani** and **Jennifer**, thanks for the unforgettable experiences from inventing our own competitive sports to getting lost in places when you entrust me with maps.

Sir **Nath** and Ma'am **Luningning**, who I consider my lifetime mentors, thank you for igniting my passion for science.

Sa tumayong pamilya ko sa Europa: **Aeriel**, **Niña**, **Anjali**, **Java**, **Andy**, **Mads**, bumuo tayo ng mataimtim na mga alaala bunga ng milya-milyang paglalakbay rito. Kayo ang nagsilbing lakas at inspirasyon ko upang tumindig at magpatuloy.

Sa mga matalik kong kaibigan na mula sa kabilang dako ng mundo, salamat sa walang humpay na suporta at pagmamahal: **Phoebe**, **Badet**, **Lariza**, **Chuck**, **Aaron**, **Meryl**, **Micah**, **Aira**, **Pearl**, **Che**, **Jerald**. Kayo ang aking kayamanan!

Sa aking pamilya, maraming salamat sa tiwala mula nu'ng hinatid niyo ako sa airport para sa walang kasiguraduhang lakbay na ito. Mahabang panahon na ang lumipas at patuloy ko'ng nararamdaman ang inyong gabay at pagmamahal: **Mama**, **Nanay**, Ate **Joy**, Kuya **John**, Kuya **Jojit**, Kuya **Michael**, Ate **Hannah**, Ate **Tessa**, **Ashley**, **Ayesha**, **Ajie**, **Sofia**, **Nijel**, **Jacob**. Ikinararangal ko kayo bilang aking pamilya. Walang katumbas ang pagkakaisa natin sa hirap man o ginhawa. Mahal ko kayo!

This dissertation received financial support from the European Union's Horizon 2020 research and innovation program under the Marie Sklodowska-Curie Grant Agreement No. 665884, the Spanish Ministry of Economy and Competitiveness through the "Severo Ochoa" Programme for Centres of Excellence in R&D (SEV-2015-0522), and the H2020 Programme under Grant Agreement No. 881603 (Graphene Flagship).

List of Publications

Journal articles included in this dissertation

1. **Bareza, N.J.**, Gopalan, K.K., Alani, R., Paulillo, B., & Pruneri, V. (2020). "*Mid-infrared gas sensing using graphene plasmons tuned by reversible chemical doping*," ACS Photonics, 2020: 7(4), 879-884.
2. **Bareza, N.J.**, Paulillo, B., Slipchenko, T., Autore, M., Dolado, I., Liu, S., Edgar, J.H., Vélez, S., Moreno, L.M., Hillenbrand, R., Pruneri, V. "*Phonon-enhanced mid-infrared CO_2 gas sensing using boron nitride nanoresonators*," ACS Photonics, 2022: 9(1), 34-42.
3. **Bareza, N.J.**, Wajs, E., Paulillo, B., Tullila, A., Jaatinen, H., Milani, R., Dore, C., Mihi, A., Nevanen, T.K., Pruneri, V, VTT, ICMAB. "*Quantitative mid-infrared plasmonic biosensing based on scalable graphene nanostructures*" [Manuscript for journal submission].

Other journal articles not included in this dissertation

1. Paulillo, B., **Bareza, N.J.**, & Valerio Pruneri. "*Controlling mid-infrared plasmons in graphene nanostructures through post-fabrication chemical doping*," Journal of Physics: Photonics 3.3 (2021): 034001.
2. Gopalan, K.K., Paulillo, B., Mackenzie, D.MA, Rodrigo, D., **Bareza, N.J.**, Whelan, P.R., Shivayogimath, A., & Pruneri, V. "*Scalable and tunable periodic graphene nanohole arrays for mid-infrared plasmonics*," Nano letters 18, no. 9 (2018): 5913-5918.

Conference presentations & proceedings

1. **Bareza, N.J.**, Paulillo, B., Gopalan, K.K., Alani, R., Pruneri, V. "*Mid-infrared gas sensor based on hybrid graphene nanostructures and ultrathin gas-adsorbing polymer*." In 2021 Conference on Lasers and Electro-Optics Europe & European Quantum Electronics Conference (CLEO/Europe-EQEC), pp. 1-1. IEEE, 2021. [Oral + Proceeding]
2. **Bareza, N.J.**, Paulillo, B., Gopalan, K.K., Alani, R., Pruneri, V. "*Graphene gas sensor with mid-infrared plasmons tuned by*

reversible chemical doping." In Optical Sensors 2021, vol. 11772, p. 117720W. International Society for Optics and Photonics, 2021. [Oral + Proceeding]

3. **Bareza, N.J.**, Paulillo, B., Gopalan, K.K., Alani, R., Pruneri, V. "*Mid-infrared plasmonic gas sensing using graphene and polymer adsorber*." Graphene & Beyond: From Atoms to Applications, 2021. [Poster]
4. **Bareza, N.J.**, Gopalan, K.K., Paulillo, B., Mackenzie, D.MA, Rodrigo, D., Whelan, P.R., Shivayogimath, A., Pruneri, V. "*Tunable graphene plasmonics for sensing applications*." Graphene Study; Obergurgl, Austria, 2019 [Poster]

Contents

List of Figures

List of Tables

Chapter 1

Introduction

1.1 Overview

In 1800, the scientific community became intrigued by the *invisible light* that was accidentally discovered by William Herschel. He had been experimenting on the heat distribution of a spectrum of sunlight when passed through a prism, and found that an invisible region below ("infra") the red light recorded the hottest. Later, Maxwell unlocked the fundamental nature of electromagnetic radiation, whose spectrum spans the visible region, as well as the infrared and other invisible ranges. Over the last century, this has extended to solid theoretical frameworks such as quantum mechanics, which have provided us with a better understanding of the behavior of light and its interaction with matter. In particular, harnessing this infrared light has led to a range of fascinating technological developments such as non-invasive medical analysis[1–3], astronomical observations[4,5], thermal infrared imaging for surveillance and military use[6,7], and environmental monitoring[8,9].

The mid-infrared (mid-IR) wavelengths, ranging between 2-20 μm, probe the vibrational modes of molecules upon light absorption. Hence, mid-IR spectroscopy displays unique spectral fingerprints of analytes, which reveal the molecular constituents and their structural information.[10] Fig. 1.1 illustrates the fingerprint locations of some relevant molecular species. Consequently, mid-IR spectroscopy becomes a powerful tool for

molecular sensing (e.g., gas, chemical and biomarker), providing specificity in a non-destructive and label-free fashion.[11–14] However, despite the remarkable technological potential, sensors and photonics systems based on mid-IR are underdeveloped compared to other frequency ranges. First, direct mid-IR sensing suffers from poor sensitivity due to a high mismatch between the micron-scale IR wavelength and the angstrom-spatial size of the molecular analytes. Second, the mid-IR systems require: (i) suitable optical materials (e.g., a large bandwidth, tunability and high sensitivity), and (ii) novel techniques and designs in developing integrated sensors and nanophotonics.

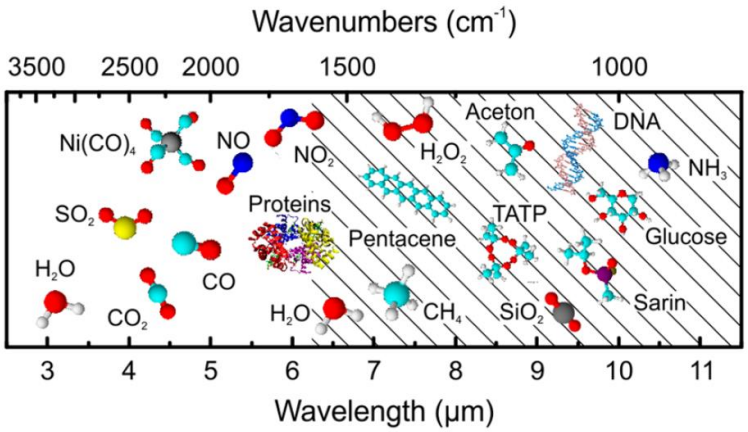

Figure 1.1: Vibrational fingerprints of representative molecular species, adapted from [10].

The mid-IR spectroscopy has been widely used in chemical analysis, where traditional techniques acquire the absorption spectra via direct IR transmission through cuvette cells containing the samples (e.g., either liquid samples or ground powders from solid samples).[15] Another useful development has been configuring the mid-IR spectroscopy with an attenuated total reflection (ATR) scheme.[16] The ATR employs high refractive index prism such that evanescent waves decaying from the top surface are used to sense either solid or liquid analytes. For gas samples, considerable absorption IR signals can be achieved by large optical

pathlength of interaction. The conventional system used is a non-dispersive IR (NDIR) spectroscopic device, which allows identification and quantification of gases. However, in order to be able to enhance the light-gas interaction, typical NDIR sensor designs tend to be bulky.[17] Enhanced optical signals were achieved by alternative techniques such as cavity ring-down spectroscopy (CRDS)[18], quartz-enhanced photoacoustic spectroscopy (QEPAS)[19], and cavity-enhanced absorption spectroscopy (CEAS)[8]. These techniques are effective in critical industrial or military applications and for biomedical diagnostics. However, they are not suitable for large deployment and consumer applications due to the high cost of their components (e.g., MIR quantum cascade laser sources).

The surface enhanced infrared absorption (SEIRA) technique resolves the issue of a weak IR absorption signal from molecular vibrations. Fig. 1.2a depicts the SEIRA principle, where the IR optical field is compressed onto a metal nanoantenna, which enhances the light-matter interaction when the molecules are embedded within the hotspots.[10,20] Correspondingly, SEIRA spectroscopy increases the IR absorption signals (the enhanced dip intensity of the molecule band in Fig.1.2b), improving the sensitivity, meaning that it can detect even a minute number of molecules (e.g., proteins for biological and medical applications[21–23]). For example, Ataka et. al. demonstrated a 10-100x SEIRA signal enhancement with protein films on nanostructured metals.[24] Moreover, SEIRA schemes have enabled the development of IR-based sensors to move toward miniaturized setups. Traditional SEIRA materials are based on nano-patterned metallic thin films that allow the excitation of electron cloud oscillations, a phenomenon known as localized surface plasmon resonance (LSPR).[23,25–28] Although metal-based SEIRA developments achieve better optical sensitivities (e.g., perfect absorber design with metal-insulator-metal (MIM) structures[28,29]), they still encounter major limitations, such as bandwidth selectivity (e.g., fixed with fabricated geometry), relatively poor IR field confinement, and lossy plasmon modes.

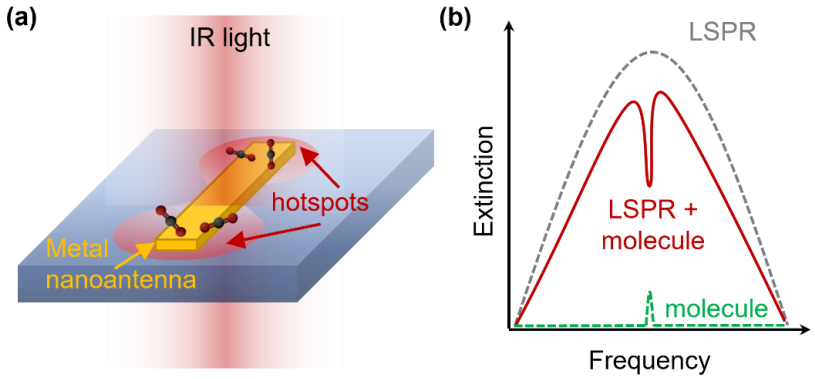

Figure 1.2: Principle of SEIRA sensing. (a) Schematic illustration of the plasmon hotspots produced by a metal nanoantenna upon IR radiation. (b) The vibrational band intensity of embedded molecules within the hotspots (green peak) is enhanced due to its coupling with the plasmons (red dip in LSPR curve).

Van der Waals (vdW) crystals are two-dimensional (2D) materials harnessed in recent years that have opened up the interesting field of 2D physics and engineering of devices.[30–34] They possess the exotic properties of polaritons – achieved by the coupling of light and dipolar elements of matter – complemented by superior optical performances, and could be an effective replacement for the traditional metal-based SEIRA materials.[35,36] Fig. 1.3. summarizes the nanoscale light trapping of representative grouped 2D-vdW materials, including plasmon polaritons (e.g., 2D semimetal: graphene[37–40]), phonon polaritons (e.g., 2D insulator: hexagonal boron nitride *hBN*[41–43]), and exciton polaritons (e.g., 2D semiconductor: Molybdenum disulfide MoS_2[44,45]). The introduction of nanostructured 2D-vdW materials in SEIRA spectroscopy leads an exciting time in modern 2D optics and advanced sensing applications.

2D-vdW heterostructures can be synthesized in a simple manner, through vertical stacking governed by out-of-plane vdW forces.[30,31] Several 2D-vdW crystal combinations offer a plethora of other unique 2D physics phenomena, and a myriad of planar optoelectronic and photonic device applications. Moreover, the simplicity of vertical stacking in 2D-vdW heterostructures bypasses the issues experienced by their bulky

counterparts, such as lattice matching and compatibility processes. In particular, vdW crystals and heterostructures could augment the benefits of mid-IR sensors and nanophotonics systems with regard to their technological maturity.[46–48]

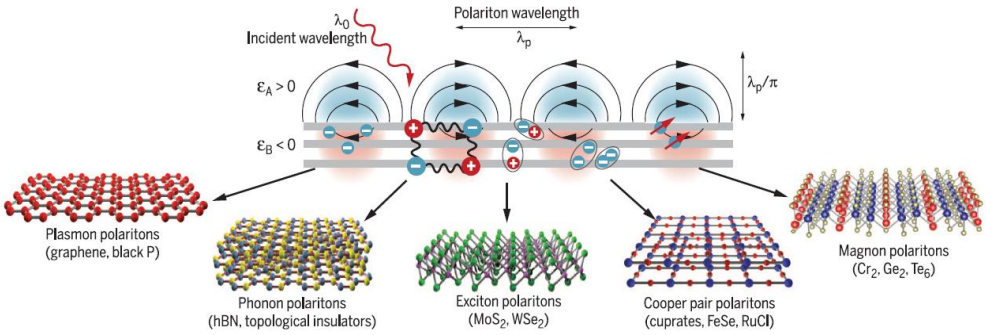

Figure 1.3: The polaritons (hybrid excitations of light and matter) of grouped vdW materials, adapted from [35].

1.2 Purpose of the Study

The aim of this dissertation is to demonstrate novel mid-IR sensing applications (e.g., gas detection and bioassays) based on graphene and other 2D materials, i.e. graphene and related materials (GRM), combined with relevant functional layers. The activities have been within the *Graphene Flagship* collaboration (specifically, work packages WP6 Sensors and WP8 Photonics & Optoelectronics), funded by the European Commission, with the aim of exploiting GRM for use in technological applications. Our motivation is to showcase the potentials of GRM as to bridge the gap in suitable sensing materials in mid-IR systems, specifically validating IR sensing platforms relevant for industrial processes and biomarker detection.

Current literature on 2D-vdW materials reports extensive studies on graphene[40,49–51] (the pioneering 2D-vdW crystal with tunable

optoelectronic properties) and hBN[41,52] (sustaining ultralow-loss polaritons). Both graphene and hBN have almost reached the zenith in fundamental research, and are now ascending toward realization of novel applications and commercialization. To this aim, this thesis evaluates the performances of graphene and hBN nanostructures for mid-IR sensing. The fabricated sensor chips are combined with relevant functional layers, such as adsorbers for gas trapping and antibodies for bio-sensing.

The specific objectives of this thesis includes:

- a novel platform for mid-IR gas sensing based on tunable LSPR of graphene nanostructures functionalized with gas-adsorbing polymer layer;
- a proof-of-concept phonon-enhanced mid-IR gas sensing system using hBN nanostructures functionalized with gas-adsorbing polymer layer;
- a quantitative and scalable mid-IR biosensing platform using functionalized graphene nanostructures.

While proof-of-concept mid-IR biosensing experiments have been successfully demonstrated with graphene LSPR[53,54], mid-IR gas sensing using GRM nanostructures is still an unexploited area. Conventional SEIRA-based gas sensors are made up of plasmonic metamaterials such as metallic nanoparticles[55,56], metal-insulator-metal (MIM)[57], and carbon nanotubes[58], which suffer from fixed bandwidth selectivity and lossy plasmon modes (typical LSPR quality factors Q ~10)[26]. This can be circumvented by employing either the tunable LSPR and extreme confined plasmon modes (decay length ℓ_d~10-15 nm)[54,59] of graphene nanostructures, or the long-lived phonon polaritons (PhP) of hBN nanostructures (e.g., typical Q~10^2 of natural[43] and monoisotopic[41] hBN nanoresonators).

A conceptualized mid-IR gas sensing scheme using the LSPR of graphene nanoribbons is shown in Fig. 1.4. Since graphene displays unique optical tunability over a large spectral bandwidth via graphene doping [60–63], the sensor chip is configured with an electrostatically back-gate bias V_{BG}

across the conventional SiO_2-Si substrate. The linear dispersion of the graphene is illustrated in the shape of a Dirac cone with illustrated graphene Fermi level (E_F) in the valence band. The E_F is tuned by a supplied V_{BG}, which consequently modulates the LSPR modes.

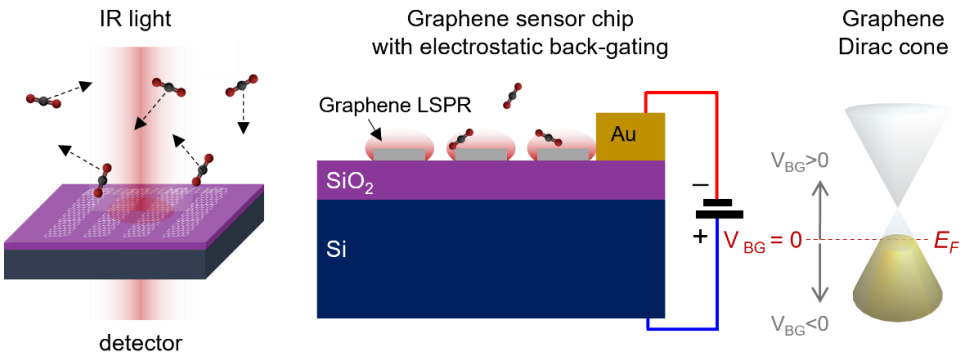

Figure 1.4: Conceptualized mid-infrared gas sensing scheme with nanostructured graphene. The sensor chip is configured with an electrostatic back-gating of graphene on a conventional SiO_2-Si substrate. The graphene dispersion in the shape of a Dirac cone is depicted with an arbitrary Fermi level E_F, which is tuned toward the upper cone for $+V_{BG}$ or toward the lower cone for $-V_{BG}$.

In a recent report, Hu et. al. successfully identified particular gases (e.g., SO_2, NO_2) using graphene LSPR modes.[64] However, they detected the gas concentration at a high limit of detection (LOD > 800 ppm) due to reliance of the system on gas physisorption at graphene surfaces. The vastly dispersed nature of gas molecules hampers surface-based detection with poor contact of the gas molecules inside the plasmonic field. In our work, we propose a new gas sensing scheme that works by functionalizing the graphene nanoribbons with a gas-chemisorbing thin layer. In particular, thin films of polyethylenimine (PEI) polymer were demonstrated for selective CO_2 capture and could be regenerated through thermal desorption.[65]

In this thesis, we also aim to exploit the long lifetime of hBN PhP modes for mid-IR gas sensing, and Fig. 1.5 illustrates the sensing scheme with hBN nanoresonators. Similarly to the work on graphene described above, we propose PEI-functionalization of the hBN nanoresonators in order to capture the gas molecules via chemisorption. This enhances the interaction of IR light-gas molecules, where the PhP field of the hBN nanoresonators overlaps with the gas trapping layer, as illustrated on the right of Fig. 1.5.

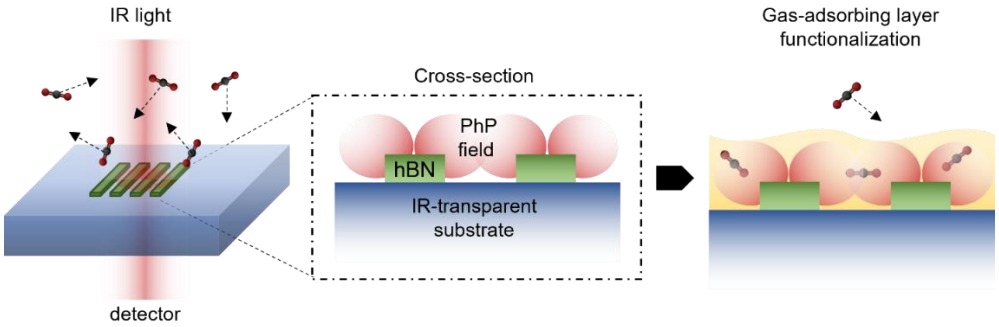

Figure 1.5: Conceptualized mid-infrared gas sensing scheme with the PhP field of hBN nanoresonators. The gas detection is enhanced with functionalization of the gas-adsorbing layer.

Graphene with relevant bio-functionalization prevails as a promising biosensor, owing to its unique optical and electronic properties.[66,67] Graphene LSPR modes have been successfully proven to detect protein bilayers (incubated recombinant protein A/G and binding the goat anti-mouse immunoglobulin G antibodies) in a SEIRA setup.[54] While this work reports a qualitative proof-of-concept experiment, our aim is to demonstrate the mid-IR biosensing of graphene for quantitative bioassays.

The honeycomb lattice structure of graphene constitutes an aromatic surface, allowing a non-covalent functionalization via $\pi - \pi$ stacking that can translate to a SEIRA biosensor platform.[68] Fig. 1.6 shows a conceptualized sensor chip using nanostructured graphene, where the

functionalized pyrene layer (attached to the graphene via $\pi - \pi$ stacking) acts as a versatile anchoring bridge for use in various bio-recognition applications (i.e., antibody-biomarker).[68,69]

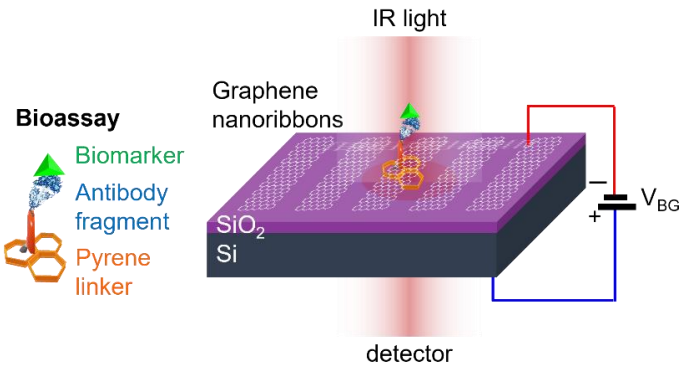

Figure 1.6: Conceptualized mid-infrared biosensing chip based on bio-functionalized nanostructured graphene. The sensor chip is configured with an electrostatic back-gating of graphene on a conventional SiO_2-Si substrate.

1.3 Dissertation Organization

This dissertation manuscript is organized as follows:

Chapter 1 provides an overview of the challenges in mid-IR molecular sensing, followed by the research aim of this dissertation in utilizing GRM polaritons for sensing applications. The review of related literature is presented in Chapter 2, which explains the relevant underlying physics along with the specific materials used in the sensing studies. The chapter specifically focuses on the fundamentals and properties of graphene and hBN crystals, as the principal 2D materials used in the experiments within this dissertation. Moreover, the basic principles of optical gas- and bio-sensing are also tackled, including the state-of-the-art techniques for relevant functional layers for gas trapping and bio-recognition.

The subsequent chapters are divided into the main mid-IR sensing works, corresponding to the specific objectives mentioned in the previous section:

- Chapter 3 investigates mid-IR gas sensing using the tunable plasmons of graphene nanoribbons functionalized with an ultrathin CO_2-adsorbing PEI layer. The graphene LSPR is influenced by the reversible PEI-induced doping of the graphene, resulting in an enhanced LSPR modulation against CO_2 gas concentration.
- Chapter 4 presents a proof-of-concept mid-IR gas sensing scheme using the ultralow-loss PhP modes of hBN nanoribbons functionalized with a thin CO_2-adsorbing PEI layer. Modulation of the hBN PhP modes against the CO_2 gas concentration is reported with a large signal-to-noise ratio.
- Chapter 5 demonstrates a quantitative bioassay using the LSPR of graphene nanoribbons. Here, the graphene is functionalized with pyrene, followed by an antibody-biomarker conjugate of vitamin B12.

An overall summary of the dissertation and the general outlook for GRM-based mid-IR sensors are concluded in Chapter 6.

Chapter 2

State-of-the-Art and Related Literature

2.1 Fundamentals of 2DM

Since the first successful isolation of single-layer graphene in 2004, we have only scratched the tip of the iceberg of the rich world of 2D Physics, where emerging varieties of 2D materials and their heterostructures possess unique and peculiar properties, different from those of their bulk counterparts.[49–51] 2D-vdW materials are described with strong in-plane covalent bonds and weak out-of-plane vdW forces. In just a few decades, the synthesis of 2D-vdW materials has leapt from primitive scotch tape cleaving methods to the current vapor phase synthesis techniques capable of producing scalable and stable 2D materials under ambient conditions.[70,71] 2D materials, with their high surface-to-bulk ratio, possess peculiar basal electrical and optical properties. In particular, nanostructured vdW crystals are capable of squeezing light into deep subwavelength volumes, rendering 2D materials promising for optical sensing applications. Recently, 2D materials have emerged as superior SEIRA materials for label-free molecular sensing applications such as protein and polymer films.[42,54,72–75] From among the various vdW crystals, the following subsection focuses on the fundamentals and mid-IR properties of graphene and hBN, which are the principal 2D materials under study in the predefined specific objectives of this dissertation.

2.1.1 Graphene and Plasmon Polaritons

Graphene, a pioneering and versatile 2D-vdW material, has attracted interest in a vast number of applications encompassing sensors, electronics, energy, telecommunications, and healthcare. This is due to its exceptional properties, such as ultimate tensile strength, large thermal conductivity, high current density, tunable and ambipolar electrical nature, and broadband light absorption. Fig. 2.1a shows a single atomic layer of the covalently bonded carbon atoms in a hexagonal honeycomb lattice. The electronic band structure in Fig. 2.1b depicts the highly symmetric conduction and valence bands meeting at a Dirac point (also referred to as the charge neutrality point, CNP). This zero-bandgap classifies graphene as a semimetal with an ambipolar nature (two charge carriers of either electrons or holes). In the low energy regime ($E < 1.2\ eV$), the graphene dispersion is linear, where the electronic charges in the graphene are reminiscent of massless particles with a relativistic behavior.[50,76] The linear dispersion relation is described by

$$E = \hbar v_F k, \tag{2.1}$$

where $\hbar$ is the reduced Planck's constant and v_F is the relativistic Fermi velocity in the graphene (~$0.003c$, c refers to the speed of light in vacuum).[77,78]

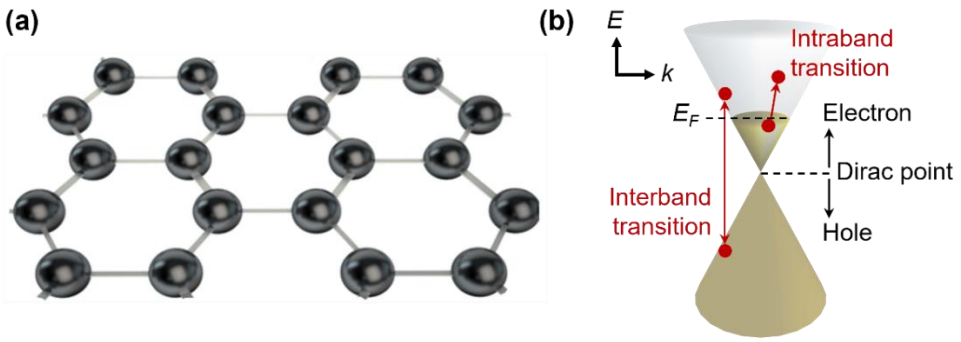

Figure 2.1: Graphene lattice and electronic band structure. (a) Schematic of the monolayer carbon atoms arranged in the hexagonal honeycomb lattice. (b) The energy-momentum ($E - k$) dispersion of graphene (n-doped at an arbitrary Fermi level E_F) in the shape of a Dirac cone, illustrating the energy transitions.

The zero-bandgap and linear dispersion of graphene near the Dirac point has an interesting impact on its optoelectronic applications. The Fermi level E_F of graphene can be tuned towards either the valence band (lower cone) or the conduction band (upper cone), for which the practical methods include electrostatic gating[60,63] and chemical doping[61,79]. Notably, this tunability feature is a long-awaited property unavailable in metallic-based plasmonic systems, enabling broadband applications such as graphene-based IR spectroscopic sensing. The modification of E_F directly changes the optical properties of the graphene, whose physical quantity is governed by the optical conductivity σ. σ consists of two distinct contributions, being the intraband σ_{intra} and the interband σ_{inter} transitions. As depicted in Fig. 2.1b, the interband transition takes place from the valence band to the conduction band when the energy of the electromagnetic radiation E_{ph} is larger than the Fermi Energy ($E_{ph} > 2E_F$). The interband transition is inhibited by Pauli blocking for $E_{ph} < 2E_F$. Meanwhile, the intraband transition occurs within the same conduction (or valence) band, which is the dominant absorption, especially when $E_{ph} \ll 2E_F$. This is governed by the Drude-like conductivity of graphene as derived by the Kubo formula:

$$\sigma_{intra} = \frac{e^2}{\pi\hbar^2(\gamma - i\omega)}\left[E_F + 2k_BTln\left(1 + e^{-E_F/k_BT}\right)\right], \tag{2.2}$$

where k_B and T are the Boltzmann constant and the temperature, respectively.[80,81]

The interband transitions for graphene in the mid-IR frequencies are usually blocked under typical doping levels (i.e., $E_{ph} = \hbar\omega_{\mathrm{mid-IR}} < 2E_F$). Therefore, the optical conductivity of graphene predominantly involves intraband transitions, and carriers behave as in a Drude-like conductor, allowing the existence of plasmon polaritons (couplings between electromagnetic radiation and electron/hole cloud oscillations). Nowadays, graphene is emerging as a powerful material for molecular sensors based on SEIRA, as its mid-IR plasmons exhibit tunability and extreme light confinement.[54]

Nano-structuring is the widely-used technique for the excitation of the mid-IR plasmons in graphene, in order to compensate for the mismatch of wavevectors between the graphene plasmons and the free-space radiation.[59,82,83] Fig. 2.2a shows a diagram of electrically connected graphene nanoribbons (GNR), where far-field IR transmission measurement displays the localized surface plasmon resonance (LSPR). The GNR array is configured with an electrostatic back-gate voltage V_{BG} on a conventional SiO_2/Si substrate, which permits the tuning of the graphene LSPR. This tunable graphene plasmonic platform is adapted for the sensing demonstrations in this dissertation, hence, will be the focus of discussion including the dispersion of graphene plasmons on SiO_2.

For undoped graphene, the Fermi level is at the Dirac point. E_F can be modified in simple fabrication processes, for example, when nanopatterning the graphene. The doping states shown in Fig. 2.2b can either be n-doped (E_F is in the conduction band with electron charge carriers) or p-doped (E_F is in the valence band with hole charge carriers). E_F can be tuned by supplying a particular V_{BG}, whose shift direction is dictated by its polarity (e.g., towards the lower cone for negative voltages). The experimental in-situ tuning of the LSPR is displayed from the calculated extinction spectra for the p-doped case ($1 - T/T_0$, where T and T_0 are taken from GNR and bare substrate, respectively). The higher magnitude of the negative V_{BG} further enhances the p-doping; hence the LSPR increases in intensity and blueshifts. Moreover, the CNP can be located for a spectrally flat response corresponding to a specific voltage V_{CNP}, indicating the absence of carrier charges to produce any LSPR. This relationship is described by the following:

$$|E_F| = \hbar v_F \sqrt{\pi \frac{C_{ox}}{q_e} |V_{CNP} - V_{BG}|}, \tag{2.3}$$

where $\hbar$ is the reduced Planck constant, v_F is the Fermi velocity, q_e is the fundamental electric charge, and C_{ox} is the capacitance of the 285 nm-thick oxide ($C_{ox} = \frac{\epsilon_0 \epsilon_{ox}}{t_{ox}}, \epsilon_{ox} = 3.9$ SiO_2 permittivity).[84]

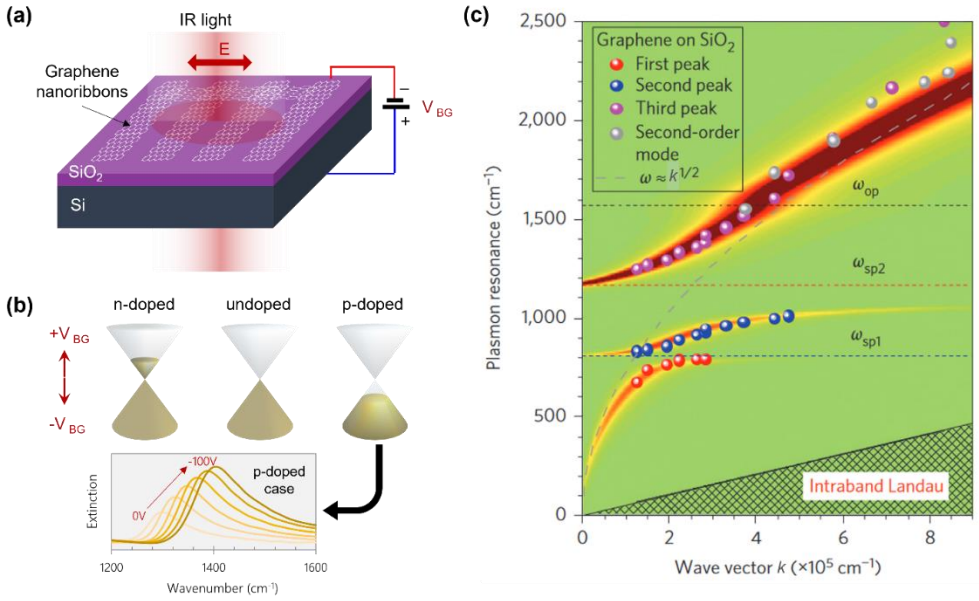

Figure 2.2: The dispersion relation of graphene nanoribbons (GNR) on SiO_2/Si. (a) Schematic of a GNR on a SiO_2/Si substrate in a perpendicularly polarized IR transmission for optical reading. A back-gate voltage V_{BG} is used for the electrostatic tuning of the graphene LSPR. (b) Illustration of different graphene doping cases, where the Fermi level can be tuned by the supplied V_{BG} and the shift directions are assigned by the polarities. The representative extinction spectra of the LSPR tuning are shown for the p-doped case. (c) The calculated (2D pseudo-colored map) and measured (markers) loss function (defined by the IR extinction) of GNR on SiO_2 as a function of wavevector and frequency, adapted from [85]. The plot indicates the three plasmon-phonon hybrid modes (colored curves), surface polar phonons of the SiO_2 (dashed lines at ω_{sp1} and ω_{sp2}), and graphene intrinsic phonons (dashed line at ω_{op}).

The platform of GNR on a SiO_2 substrate results in a modified graphene plasmon dispersion, as depicted in Fig. 2.2c.[85] In this case, the graphene plasmons interact with two surface optical phonons of SiO_2 at frequencies ω_{sp1}~$806\ cm^{-1}$ and ω_{sp2}~$1168\ cm^{-1}$, whose coupling produces three branches of hybridized plasmon-phonon modes with two anti-crossings. The mode above ω_{sp2} corresponds to the LSPR peak which has an altered plasmon dispersion compared to the pristine state of the graphene (dashed gray curve). The intensities of the three modes infer the energy exchange, such that for an increasing wavevector the spectral weight

transfers from a low-frequency hybrid branch to a high-frequency plasmon branch. Meanwhile, the linewidth along the frequency axis shows the damping nature. Below the frequency of the intrinsic optical phonon of the graphene (ω_{op}~$1580\ cm^{-1}$), the LSPR has a higher plasmon lifespan as it resonates near ω_{sp2}. Near and beyond ω_{op}, the peak broadening is indicative of larger damping due to the decay contribution coming from the emission of the graphene optical phonon. The GNR on SiO_2 offers a novel platform for the excitation of mid-IR graphene plasmons with tunable LSPR via a supplied V_{BG}.

2.1.2 hBN and Phonon Polaritons

Polar dielectric hBN displays peculiar properties, such as high thermal stability, chemical inertness, and mechanical robustness, making it a suitable material for operation in harsh environments. Furthermore, the rigid, electrically insulating, and high-quality crystal hBN nanosheets enable it's use as a contending template or passivation layer for graphene electronics.[86,87] The crystal lattice of hBN is illustrated in Fig. 2.3, showing a strong in-plane covalent network of boron and nitrogen bonds at interlocking hexagonal rings. The stack of atomic layers is held together by the relatively weak vdW bond.

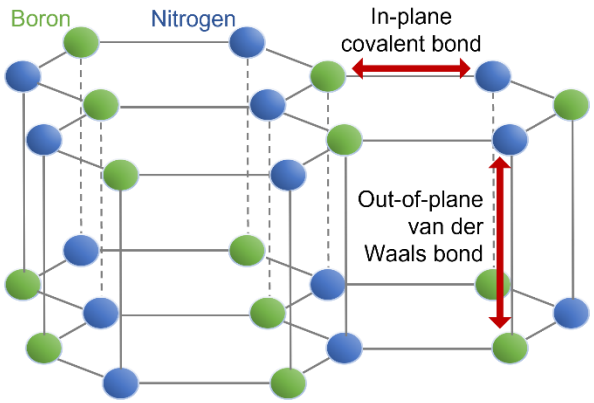

Figure 2.3: Schematic of the crystal lattice of hBN.

The hBN crystal structure results in a uniaxial anisotropy of dielectric permittivity in the in-plane ($\epsilon_{\parallel}$) and out-of-plane ($\epsilon_{\perp}$) directions. The relative permittivity as a function of frequency ω can be generally expressed (j as either $\perp, \parallel$) in a single-Lorentzian form by the following:

$$\varepsilon_j = \varepsilon_{\infty,j}\left(1 + \frac{\omega_{\mathrm{LO},j}^2 - \omega_{\mathrm{TO},j}^2}{\omega_{\mathrm{TO},j}^2 - \omega^2 - i\omega\gamma_j}\right), \tag{2.4}$$

where ε_∞ is the high-frequency dielectric constant, γ_j is the damping factor, and ω_{LO} and ω_{TO} represent the longitudinal (LO) and the transverse (TO) optical phonon frequencies, respectively. The hBN is considered to be a natural hyperbolic material in the frequency regions where $Re(\epsilon_{\parallel}) \cdot Re(\epsilon_{\perp}) < 0$.[88–90] This condition of opposite permittivity signs between the orthogonal directions occurs in two frequency regions designated as lower (LR, Type I) and upper (UR, Type II) Reststrahlen bands. The $\epsilon_{\parallel}$ is isotropic and negative (positive) in the UR (LR), while the $\epsilon_{\perp}$ is positive (negative). The electromagnetic radiation couples to the crystal lattice vibration in the LR and the UR bands, generating long-life and sub-diffractional PhP modes. Fig 2.4a illustrates the PhP dispersion of a 105 nm-thick hBN slab, where branches of curves consist of the fundamental (l=0) and the higher PhP modes.[90] Moreover, the PhP modes in the UR and the LR are a result of the in-plane and the out-of-plane vibrations, respectively. For instance, nanostructuring a thin layer of hBN supports PhP modes that propagate with in-plane hyperbolic dispersion.[91]

The varying thickness of few-layered hBN crystals tunes the PhP dispersion, where the polariton wavelength λ_p scales linearly with the crystal thickness.[89] Also, the thinner hBN crystal results in higher confinement ($\lambda_{\mathrm{IR}}/\lambda_p$) of an incident IR light, which can be optimized for target applications (e.g., considering analyte sizes in sensing). Because of the long lifetime of the PhP in naturally abundant hBN, the isotopic enrichment of the hBN substantially increases its lifespan, with a threefold improvement.[41] Furthermore, the ultralow-loss nature of hBN crystals enable the natural[43] and monoisotopic[41] hBN nanoresonators to exhibit

high-Q mid-IR resonances, which were recently employed to demonstrate molecular sensing at the strong coupling limit.[42,75]

In this dissertation, the hBN nanoresonators on a CaF_2 substrate are adapted for sensing experiments using PhP modes, as depicted in Fig. 2.4b. Autore et. al. confirmed experimentally that the PhP resonances of hBN nanoresonators blueshift with reducing ribbon widths.[42] Fig. 2.4c shows the case for monoisotopic hBN nanoresonators where the relative transmission spectra (T/T_0) exhibit sharp resonances in the UR band for various geometry.

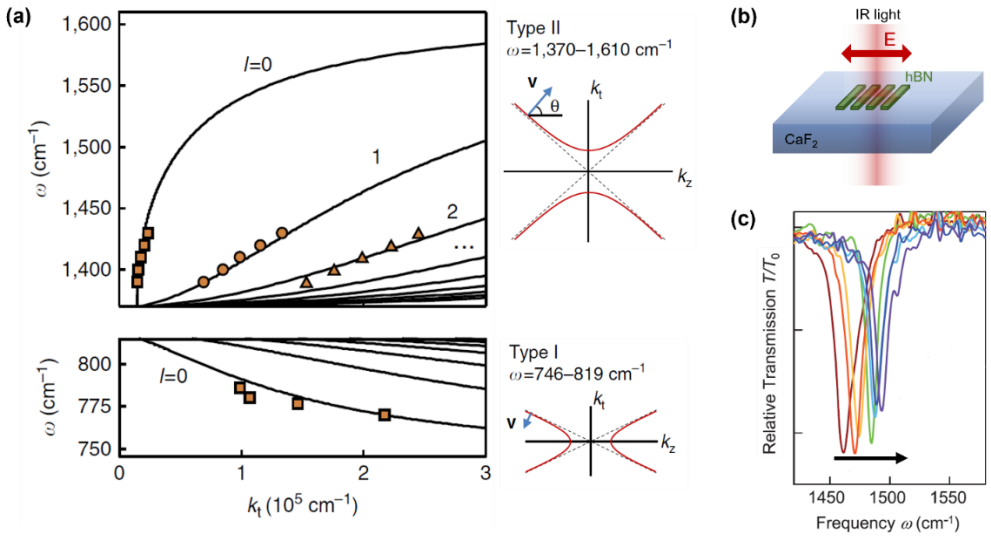

Figure 2.4: Hyperbolic dispersion of PhP modes in hBN. (a) Adapted from [90]: The calculated (curves) and measured (markers) PhP dispersion of 105 nm-thick hBN in the UR (Type II) and the LR (Type I). The side panel displays the isofrequency curves of the hyperbolic dispersion for the two bands with blue arrow indicating the polariton group velocity. (b) Schematic of hBN nanoresonators on a CaF_2 substrate in a perpendicularly polarized IR transmission for optical reading. (c) Relative transmission spectra of monoisotopic hBN nanoresonators for reducing ribbon widths indicated by the black arrow, adapted from [42].

2.2 Principles of IR Gas Sensing and CO_2 Functional Layer

2.2.1 IR Gas Sensing

Gas sensing technology has made a great impact across a wide range of applications, such as air quality monitoring, hazard assessment, pipeline leakage detection, and breath diagnostics.[92–95] The gas sensors market is currently dominated by electrochemical technology that traditionally uses metal oxide semiconductors in transducing the target gas, where the chemical reaction is converted into an electrical readout.[96] However, this system still suffers as a result of high power consumption and a short device lifespan. Mid-IR spectroscopy is a powerful optical technique that directly probes the vibrational fingerprints of molecules in a non-destructive fashion (recall Fig. 1.1), offering high sensitivity, a fast response, and large device lifetime.[97,98] Selected benchmarking of IR-based optical gas sensing is summarized in Table 2.1.

Table 2.1: Benchmark study of IR-based optical gas sensor.

	GRM SEIRA	*Other technologies*		
	Bilayer graphene LSPR gas sensor[64]	**Submerged silicone diffusion cell[99]**	**Sensirion-SCD30 (Commercial)[100]** $63	**Gasmet-DX4040 (Commercial)[101]** $65,000
Instrument	FTIR	NDIR	NDIR	FTIR
Target gas	SO_2	N_2O	CO_2	multi-gas
Limit of detection	800 ppm	1 ppm	400 ppm	sub-ppm

Traditional spectroscopic gas sensing is based on a non-dispersive infrared (NDIR) sensor, as illustrated in Fig. 2.5a.[17] It consists of a broadband source passing through a gas sampling chamber with active (absorbing region) and reference (non-attenuating region) filters on the detectors. The highly dispersive nature of gas molecules requires a high-volume gas chamber to achieve a significant absorption signal, making

an NDIR sensor a bulky instrument. The IR absorption is based on the Beer-Lambert law:

$$I = I_0 \exp\left(-\gamma_{\text{enh}} \alpha L\right), \tag{2.5}$$

where I is the intensity of the light that traverses the gas sample, I_0 is the intensity of the incident light, γ_{enh} is the enhancement factor, α is the effective absorption coefficient of the gas, and L is the optical interaction path-length.[102]

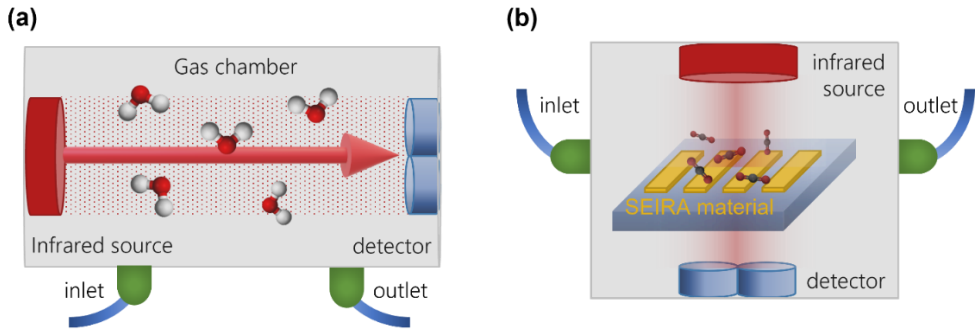

Figure 2.5: IR-based gas sensing. Schematic diagram of (a) NDIR gas sensor and (b) SEIRA-based gas sensor.

As discussed in the previous chapter, one way to overcome the weak IR-molecule interaction is to employ a SEIRA scheme (Fig. 2.5b), which enables a miniaturized setup of on-chip based molecular sensors. The near-field coupling that occurs in SEIRA materials allows the γ_{enh} in Equation 2.5 to be greater than unity. Gas molecules are highly dispersive in nature, leading to an inherently poor physisorption on 2D structures. Consequently, gas detection in a SEIRA scheme has so far been elusive. Although Hu et. al. did successfully demonstrate SEIRA-based gas sensing using graphene plasmons, they reported a high limit of detection of 800 ppm with SO_2 gas for bilayer graphene.[64] One strategy to leverage the signal enhancement is to functionalize the SEIRA material with a gas trapping material. The traditional examples of which include zeolites and activated carbons. Specifically in our proposed scheme, we have considered a thin layer of polyethylenimine (PEI) polymer, which

selectively chemisorbs CO_2 gas. In this dissertation, we present proof-of-concept CO_2 sensing with graphene and hBN, functionalized with a PEI layer. The following subsections tackle the nature of PEI polymer including its interaction with CO_2 gas and its chemical doping effect on graphene.

2.2.2 Polyethylenimine (PEI): CO_2 Gas Trapping Layer

PEI is a cationic polymer containing amine groups, which finds many applications in organic electronics and biomedical applications, and is also largely devoted to the capture of CO_2 at room temperature.[103–106] Recently, thin films of PEI polymer have been demonstrated as functional adsorber for mid-IR CO_2 sensing on resonant nanostructures such as metal metasurfaces and all-dielectric photonic slabs.[29,107]

The interaction between CO_2 gas and amine-containing PEI occurs via a zwitterion mechanism, whereby the hard-acidic CO_2 molecules bind covalently with the basic amine groups of the PEI polymers even under atmospheric thermal conditions.[108,109] The amines are derivatives of ammonia with primary (RNH_2), secondary (R_2NH), and tertiary (R_3N) groups, where R represents species from the alkyl group. PEI is synthesized in either linear form that contains all the secondary amines, or a branched form composed of all the amine groups.

The CO_2 gas adsorption dynamics in the PEI medium has been thoroughly studied in literature, and consists of a rapid interface adsorption followed by a slower diffusion into the bulk medium.[110,111] The CO_2 molecules react with the primary and secondary amines producing carbamate compounds, whose reversible chemical reactions are as follows:

$$CO_2 + 2RNH_2 \rightleftharpoons RNHCOO^- + RNH_3^+, \tag{2.6}$$

$$CO_2 + 2R_2NH \rightleftharpoons R_2NCOO^- + R_2NH_2^+. \tag{2.7}$$

The reversibility in regenerating the amines and CO_2 can be obtained through thermal desorption with a ≥ 85 ℃ heat treatment.[65] These carbamates are stable compared to CO_2 combined with the tertiary amine group, which produces bicarbonates (HCO_3^-) under humid conditions[112]:

$$CO_2 + R_3N + H_2O \rightleftharpoons R_3NH^+ + HCO_3^-. \quad (2.8)$$

The interactions between the CO_2 and the amine groups in the PEI transform the ionic constituents in the medium, which modifies the permittivity of the PEI.[109] The products of the chemical reactions between the CO_2 and PEI amine groups have natural mid-IR frequency vibrations as summarized in Table 2.2.

Table 2.2: Frequency assignments of product species from PEI-CO_2 interaction.[113–117]

Frequency (cm^{-1})	Assignment
1101	C=O symmetric stretch in R_2NCOO^-
1304	Conformational change in HCO_3^-
1380	Asymmetric stretch in carbonate
1475, 1488	NCOO skeletal vibration
1550, 1565	C=O asymmetric stretch in R_2NCOO^-
1636, 1650	N-H deformation in NH_3^+
3055	N-H stretch in NH_3^+
3360	Asymmetric NH_2 stretch
3420, 3439	N-H stretch in $RN\text{-}HCOO^-$

The dielectric medium of the PEI can be modeled by the electronic oscillators corresponding to the resonant frequencies of the PEI vibrations. The relative permittivity of the PEI follows the multi-Lorentz model, written as:

$$\varepsilon_{PEI} = \varepsilon_\infty + \sum_{j=1}^{5} \frac{S_j}{1-\left(\frac{k}{k_{0j}}\right)^2 - i\gamma_j\left(\frac{k}{k_{0j}}\right)}, \quad (2.9)$$

where ε_∞ is the non-dispersive dielectric background, S_j is the amplitude, γ_j is the damping factor, and k_{0j} is the central wavenumber.

2.2.3 PEI-Induced Graphene Doping

The key element in achieving a high sensitivity of graphene sensing via molecular adsorption involves a charge transfer process. Polar gas molecules (e.g., NO_2 and NH_3) offer an excellent graphene-based gas sensing performance by directly affecting the local carrier concentration of the graphene.[118] However, in order to induce changes in graphene conductivity upon exposure to nonpolar gas molecules (e.g., CO_2 and H_2), functionalization is required.[119,120] To this end, this subsection discusses the critical role of PEI functionalization and CO_2 gas adsorption, which induce the chemical doping of the graphene.

The PEI polymer is regarded as a homogenous n-type dopant and stable non-covalent functional layer of the graphene.[121] Fig. 2.6a illustrates an amine unit of PEI on graphene, wherein amine protonation is compensated by electron donation to the graphene (i.e., n-type doping).[122] Upon CO_2 gas adsorption, an equilibrium takes place on the chemical reactions with the amines in the PEI (refer to Eqn. 2.6 and 2.7 in the previous subsection), reducing the electron doping of the graphene as depicted in Fig. 2.6b. The charge transfer occurring in polymer-functionalized graphene creates an enhanced detection for nonpolar gas molecules, such as CO_2 gas in the case of PEI.

The n-type doping effect of the PEI polymer arising from the charge transfer process was experimentally demonstrated by Jo et. al., where their electrical measurements retrieved the 2D conductance profile σ_{2D} as a function of the V_{BG} (see Fig. 2.2a for the gating) from a graphene field effect transistor (GFET) device.[123] In their work, the CNP shifts toward negative voltages after PEI coating, indicating that the Fermi level is in the conduction band. This confirms the n-type doping effect of the amine-rich PEI polymer. Another prevalent feature with a PEI-functionalized GFET device is the conductance asymmetry. The n-dopant nature of the PEI polymer creates a potential barrier, suppressing the hole carriers, as seen by the decreased hole conductivity ($V_{BG} < V_{CNP}$).[124] This infers that the LSPR excitation with PEI-functionalized graphene is solely

facilitated by the electron carrier oscillation, as experimentally demonstrated in [61].

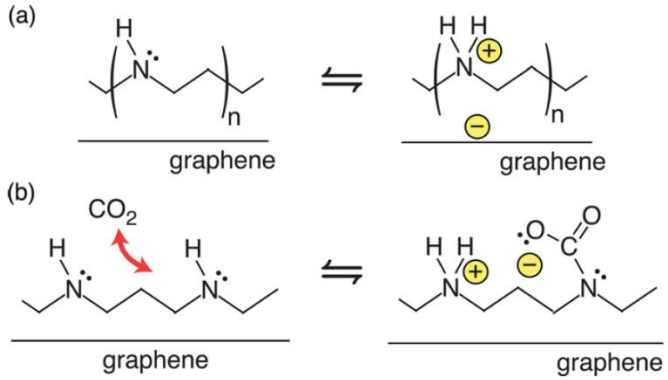

Figure 2.6: PEI-induced doping mechanism, adapted from [122]. (a) The PEI coating results in the protonation of an amine group and equilibrates with an increased electron density (n-type doping) within the graphene. (b) The adsorption of the CO_2 facilitates a reduction in the PEI-induced graphene doping.

2.3 Principles of IR Biosensing and Graphene Bio-Functionalization

2.3.1 IR Biosensing

Optical biosensing provides a cost-effective and real time biomolecular detection, and has achieved an exponential technological growth in recent decades in widespread applications such as in clinical analysis, food quality control, and drug discovery.[125,126] A benchmark study of existing optical biosensor technologies in the commercial market and research phase is presented in Table 2.3. Traditional refractometric sensing with visible/near-IR light is based on a Kretschmann configuration, which excites the SPR along a thin metallic film upon internal reflection through a prism, as illustrated in Fig. 2.7a.[127] The plasmonic field extending in the outer environment provides a platform

for surface-based and in-situ analysis of biomolecular interactions in an aqueous medium. The light absorption signal depends on the refractive index change induced by bio-analytes, and is the basis of refractometric sensing with earlier developments using the near-IR or visible region. Biacore by *Cytiva* (transitioned from *GE Healthcare*) has the largest SPR biosensor market share, offering various functionalized plasmonic gold chips for analyzing several biomolecular interactions.

Table 2.3: Benchmark study of SPR and LSPR biosensors in the commercial market and research phase.

	Biacore T200 SPR biosensor (commercial)[128]	**LamdaGen LSPR biosensor (commercial)[129]**	**Au LSPR SEIRA biosensor (research)[130]**	**Graphene LSPR SEIRA biosensor (research)[54]**
Sensor element	Au coated prism	Au nanostructures	Au nanostructures	Graphene nanostructures
Sensing scheme	Refractometric VIS/NIR		IR absorption spectroscopy	
Sensitivity	~fM	30 pg/mL	100 pg/mL	n.a.
Specificity	Wide-range of enzyme-linked immunosorbent assays (ELISA)		Vibrational fingerprints with biorecognition elements	
Advantages	Well established technology and functionalization protocols		Intrinsic chemical specificity (molecular vibrations)	Intrinsic chemical specificity; dynamic optical tuning; extreme field confinement
Applications	kinetic analysis	In vitro diagnostics		

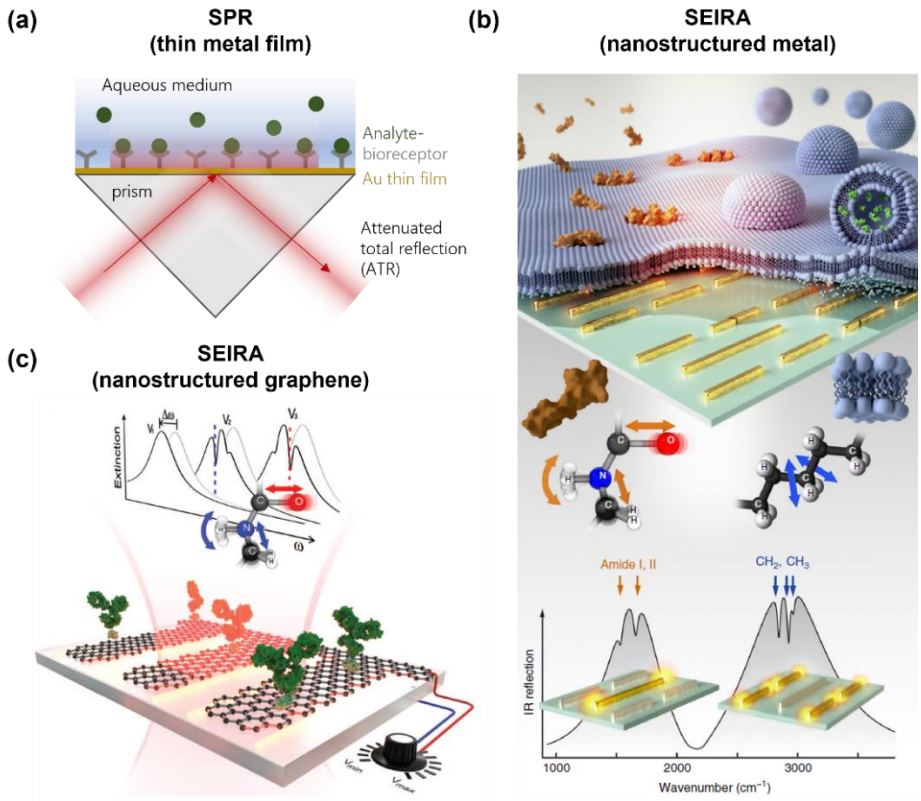

Figure 2.7: Optical biosensing techniques. (a) SPR-based biosensor in a Kretschmann configuration, where plasmons propagating along a thin Au film interact with biomolecules in an aqueous medium upon attenuated total reflection of light in a prism. (b) SEIRA-based biosensor using multi-resonant metal nanoantennas, where vibrational signals are coupled in a gold LSPR enabling the biochemical-specific detection of proteins (amide bands) and lipids (methylene bands), adapted from [131]. (c) SEIRA-based biosensor using graphene nanoribbons, where the graphene LSPR is tunable via electrostatic back-gating, adapted from [54].

Meanwhile, the mid-IR regime probes the molecular vibrational modes and provides intrinsic chemical specificity of analytes. The SEIRA technique enables an enhanced IR absorption signal of biomolecules embedded on plasmonic metamaterials, as depicted in Fig 2.7b.[131] Here, multi-resonances in the mid-IR are obtained by various geometries of gold nanoantennas, allowing the detection of protein (coupled amide bands) and lipids (coupled methylene bands) at different frequency

ranges. As noted earlier, the main limitations of metal-based LSPR structures are the bandwidth selectivity and the relatively poor field confinement in the IR. Graphene, however, with its dynamic optical tunability and extreme IR field confinement, circumvents these issues. Electrostatic gating in graphene can be used to modulate the LSPR modes over a large spectral bandwidth (see Fig. 2.2). Rodrigo et. al. demonstrated a SEIRA biosensor with a dry-spotted protein (specifically, recombinant protein A/G and binding goat anti-mouse immunoglobulin G antibodies) on a GNR array, as shown in Fig. 2.7c.[54] Here, the graphene LSPR is dynamically tuned to the frequency locations of the protein vibrational modes (amide bands). While this work is a fundamental and qualitative demonstration, the goal of this dissertation is to validate a quantitative dry-spotted bioassay with a relevant functionalization technique, using an IR readout in the transmission mode and the standard tunable LSPR of a GNR array platform. The following subsection focuses on the topic of graphene as a suitable material for a biosensor platform, and includes the functional groups for biorecognition.

2.3.2 Graphene-Based Biosensor and Functionalization

Graphene has emerged as a breakthrough template material for biosensing owing to its high surface area, arguably good biocompatibility, and extraordinary electronic properties arising from the $\pi-$electron clouds of sp^2 hybridized carbon bonds.[132,133] Graphene enables bio-functionalization by either covalent bonds or non-covalent interactions, serving as a versatile template for various bioreceptor and analyte combinations, refer to Fig. 2.8.[66] Covalent functionalization requires a chemically reactive species in order to yield good stability in the functional layer. However, it is unfavorable due to the disruption of the π-conjugation on the graphene surface, which lessens the carrier mobility and conductivity.[134] On the other hand, non-covalent functionalization relies on molecular adsorption to the graphene lattice, which includes $\pi-\pi$ stacking, hydrogen bonding, and electrostatic

interaction.[135] The $\pi - \pi$ stacking occurs when aromatic biomolecules (i.e., ring structure of nucleobases) interact with the hexagonal rings of the graphene lattice. This version has proven to be the most beneficial as it exhibits self-assembly and preserves the intrinsic properties of the graphene.

Different biomolecules, such as DNA, proteins, viruses, and enzymes, can be immobilized onto the surface of graphene. The bioreceptors attached primarily to the graphene surface may be organic or inorganic materials, with examples from Fig. 2.8 including antibodies, enzymes, and ssDNA capture elements. The bioreceptor selectively binds with the target analytes above the layer that translates to measurable signals. Information such as recognition events or analyte concentrations can be transduced in several ways, popular among which are optical and electrochemical detections.

The protocol implemented in this dissertation involves non-covalently functionalized graphene with a pyrene linker (via π-π stacking). Next, the antibody-analyte conjugate pair of vitamin B12 is considered to demonstrate the quantitative dried bioassay using tunable mid-IR graphene LSPR.

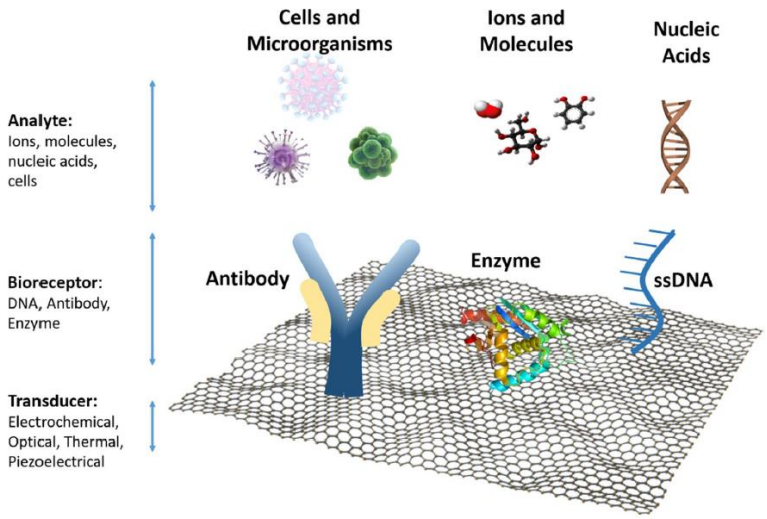

Figure 2.8: Conceptual view of a biosensor with various bioreceptor-analyte combinations on graphene platform, adapted from [66].

Chapter 3

Gas Sensing with Tunable Graphene Plasmons

Bareza, N. J., Gopalan, K. K., Alani, R., Paulillo, B., & Pruneri, V. (2020). "Mid-Infrared Gas Sensing Using Graphene Plasmons Tuned by Reversible Chemical Doping," ACS Photonics, 2020: 7(4), 879-884.

Graphene is considered a powerful material for mid-IR spectroscopic applications since its mid-IR plasmons display outstanding properties, such as unique optical tunability via graphene doping and extreme light compression.[37,38,60,79] Nanostructured graphene has recently prevailed as a SEIRA material for label-free molecular sensing applications such as protein and polymer films.[54,72–74] This chapter demonstrates the mid-IR CO_2 gas sensing of graphene nanoribbons (GNR) functionalized with an ultrathin CO_2-selective PEI layer. The optical tunability over large spectral bandwidth is enabled by electrostatically back-gating the connected graphene nanostructures on a SiO_2-Si substrate. By recording the far-field transmission spectra of the PEI-coated GNRs, we demonstrate two coexisting transduction mechanisms with CO_2 sensing: (i) the change in strength of the vibrational bands of the PEI layer (SEIRA effect) and (ii) the tuning of the LSPR modes via graphene chemical doping assisted by PEI. We report the latter as a novel CO_2 sensing scheme where chemical doping of the graphene is induced by the n-dopant amines of the PEI.[124] The proposed hybrid gas sensor can be extended to other functional polymers that specifically adsorb different groups of gases. For instance,

the same PEI polymer can be evaluated with other specific and relevant gases (e.g., volatile organic compounds[136]). Also, the chemical-based doping of the graphene shows a promising route towards gate-free sensing applications.[61]

3.1 Plasmonic-Based Gas Sensing Scheme with Graphene Nanoribbons

This section describes the construction of IR-based gas sensing setup and the fabrication of graphene-based plasmonic sensor chip.

Fig. 3.1 illustrates the gas sensing scheme, where a customized gas cell was coupled to a Fourier transform infrared (FTIR) microscope system. The fabricated sensor was placed on a heating stage inside the gas cell in order to regenerate the CO_2 adsorption capacity of the PEI. The gas cell was equipped with IR-transparent windows and the stage has a circular opening to allow transmission measurements with an FTIR microscope. The plasmonic sensor chip is configured with an electrostatic back-gating setup to enable the LSPR tuning. The incoming IR light was polarized perpendicular to the long axis of the graphene ribbons for the LSPR excitation, and far field transmission spectra were collected by a liquid nitrogen-cooled mercury-cadmium-tellurium (MCT) detector. Subsequent measurements were taken with 100 averaged scans, with a resolution of 16 cm^{-1} per region on GNR+PEI (T) and bare substrate (T_0) to acquire the extinction spectra $\left(1-\frac{T}{T_0}\right)$.

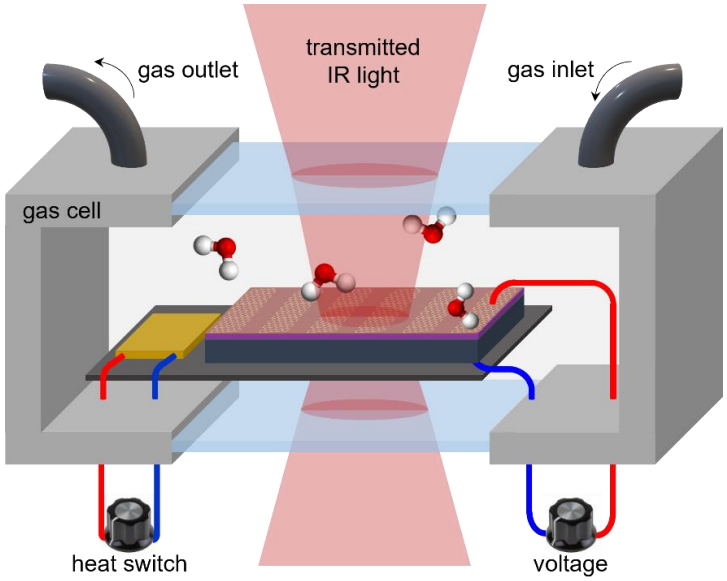

Figure 3.1: Schematic diagram of the gas sensing setup. The sensor chip mounted on a heating stage and configured with a supply of back-gate voltage V_{BG} is sealed in a gas cell, equipped with valves for gas flow and IR-transparent windows for transmission measurements with an FTIR microscope.

Fig. 3.2 outlines the sensor fabrication process. First, the standard graphene wet transfer was performed using a monolayer of graphene grown via chemical vapor deposition on copper foil and covered with a PMMA layer (from *Graphenea Inc.*). The copper foil was chemically etched in 0.1 M ammonium persulfate in water solution for 4 hrs to ensure the complete removal of any copper residues. Then, the graphene beneath the PMMA coating was rinsed twice by suspending it in milli-Q water for 5 mins. Next, the suspended graphene was wet-transferred onto an SiO_2-Si substrate and laminated over the pre-patterned top gold contacts. The sample was left overnight in a vacuum chamber to dry any excess trapped water. The PMMA was removed by subsequently rinsing the sample in acetone and IPA.

The GNR array was then fabricated via electron beam lithography. The sample was spin-coated with a 40 nm resist (ZEP520A by Zeon), then baked at 170^{o}C for 2 mins. A GNR array pattern was written on the resist on top of the graphene using a 50 keV electron beam (CRESTEC), then

exposed ZEP regions were developed. Next, the exposed graphene was removed using oxygen/argon (1:1) plasma etching at 10 W for 1 min. The SEM characterization shows a fabricated ribbon geometry of 50 nm width and 90 nm period. Additionally, the patterned ribbons are entirely connected (refer to SEM micrograph in Fig. 3.2) to set a uniform potential at whole graphene array when electrostatically back-gated, whose voltage V_{BG} is supplied across a 285 nm native silicon dioxide layer.

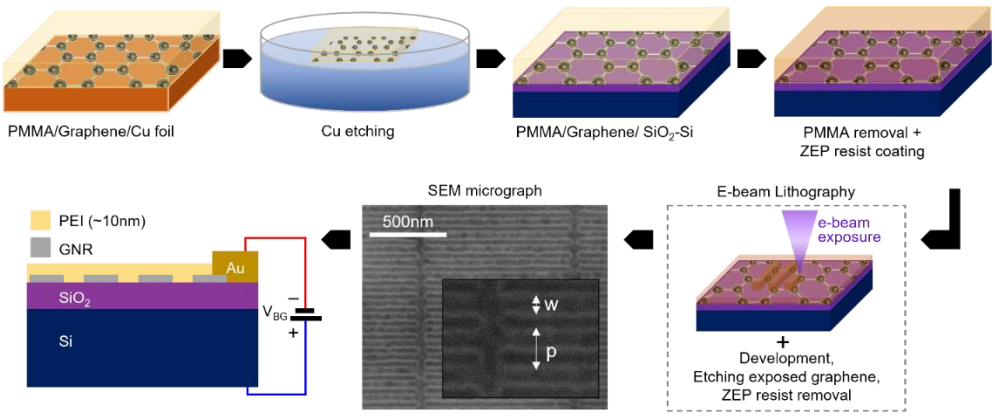

Figure 3.2: Schematic flowchart for the fabrication of the proposed graphene-based plasmonic gas sensor. The monolayer graphene was wet-transferred on an SiO_2-Si substrate and then, electron beam lithography was performed to fabricate the GNR array. An SEM micrograph shows the ribbon geometry of width w=50nm and period p=90nm. Lastly, an ultrathin PEI layer was deposited on top of the GNRs. The cross-section schematic illustrates the sensor layers configured with an electrostatic back-gating of graphene.

Lastly, a layer of ~10 nm PEI was deposited on top of the GNR. The thickness was chosen to match the lateral decay length of the graphene plasmons, typically 10-15 nm from the graphene surface.[54,59] Further details about the PEI including its doping effect on the graphene are explained in Section 3.2.

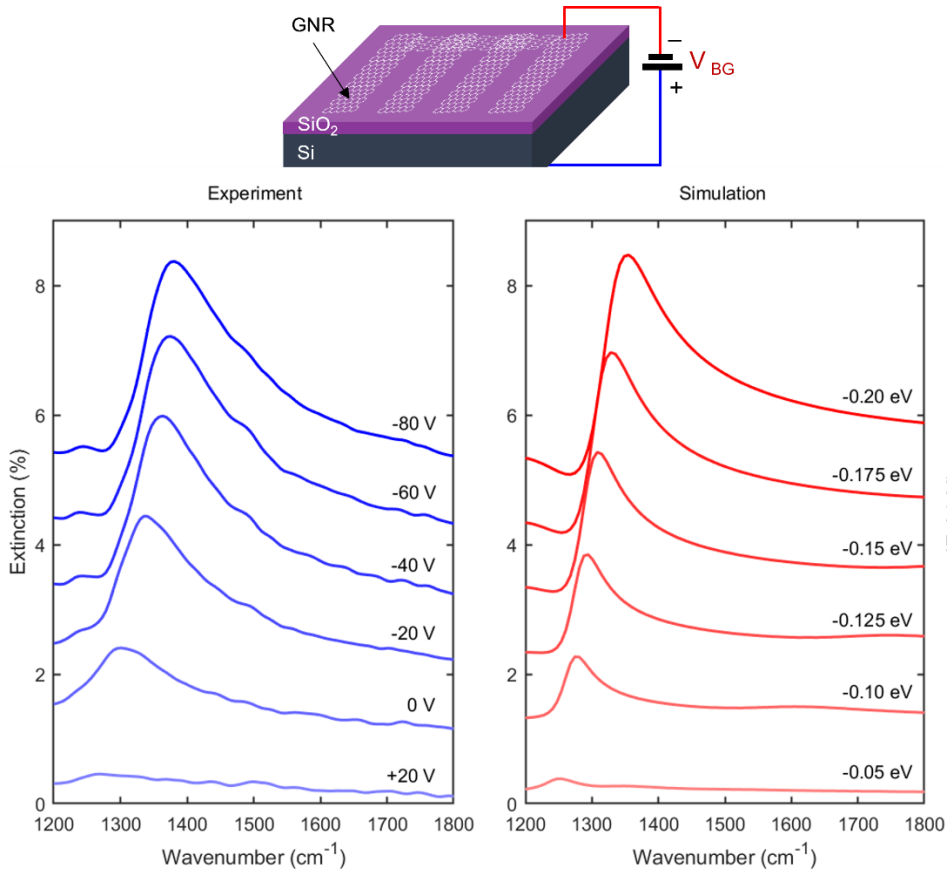

Figure 3.3: As-prepared GNR surface characterization. [Top] Schematic of the sensor chip without PEI functionalization. [Bottom] Experimental and simulated LSPR response of the GNR surface for varying V_{BG} and Fermi energy E_F, respectively.

Before PEI functionalization, the fabricated GNR surface was characterized by subsequent spectral measurements for different V_{BG} values. Fig. 3.3 shows a schematic of the sensor with the GNR array completely exposed to ambient atmosphere. The measured extinction spectra exhibit modulation of the LSPR modes within a spectral bandwidth of 1200-1500 cm^{-1}. From the optical response upon V_{BG} sweeping, we evaluate the charge neutrality point (CNP) around $V_{CNP} = +20V$, and the LSPR mode appearing at zero bias reveals that the fabricated GNR is slightly p-doped (Fermi level in the valence band, as expected for fabricated graphene samples alike[54,59,137]). The resonance

further grows in amplitude and blueshifts toward higher negative V_{BG}. This LSPR enhancement is a direct consequence of increased p-doping of the graphene for a higher negative bias.

To identify the intrinsic doping of as-prepared GNR, electromagnetic simulations were performed using finite-element methods in the frequency domain (COMSOL software). The geometrical parameters were taken from the experimental values of the fabricated GNR. The graphene damping was fixed at $\gamma = 6.7\text{x}10^{13}s^{-1}$, which approximately matched the experimental LSPR linewidth. This damping value is inserted into the complex Drude-like conductivity model of graphene in Equation 2.2.[81] Then, the Fermi energy E_F was swept for a certain range in the valence band to reproduce the experimental response. The intrinsic doping of the as-prepared GNR is estimated to be around $E_F = 0.15\ eV$.

3.2 Ultrathin PEI Functionalization and Doping Effect on GNR

As noted in the previous section, the thickness of the PEI layer must optimally match the LSPR decay length of the fabricated GNR. Since the graphene LSPR extremely confines the near field with decay length around 10-15 nm from the graphene surface[54,59], the PEI formulation is required to achieve the equivalent thickness of an ultrathin layer. The solutions were prepared by diluting branched PEI (M_w~2500 from Sigma Aldrich) in ethanol. After magnetic stirring, the solutions were spin-coated on Si samples at 5000 rpm and then, the remaining ethanol solvent in the film was evaporated by heating the chips at 100°C for 2 mins. Fig. 3.4 displays the characterizations of the deposited PEI membranes from two different solutions. PEI thicknesses of 30 nm and 9 nm were evaluated from ellipsometric fitting (Fig. 4.4a) with 0.76 wt% and 0.22 wt% concentrations of PEI diluted in ethanol, respectively. These PEI layers formed continuous films with RMS roughness around 0.3 nm as depicted in representative AFM images in Fig 3.4b/c.

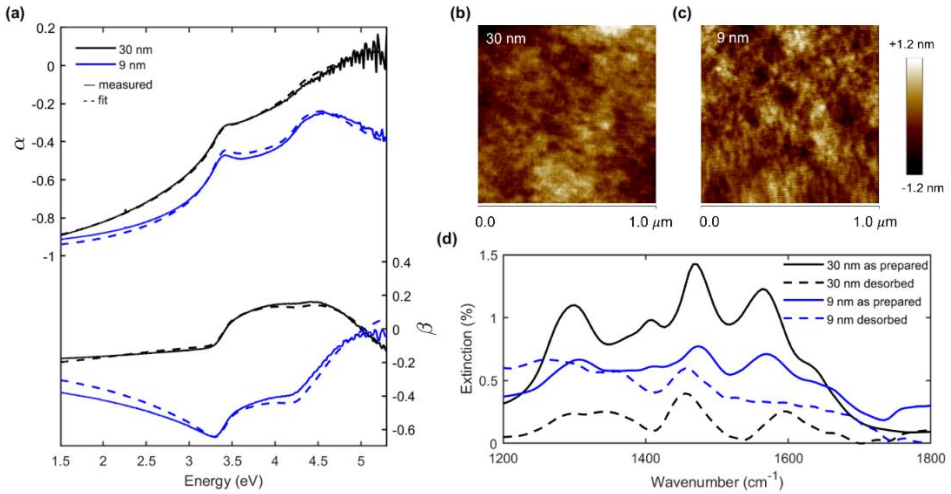

Figure 3.4: Ultrathin PEI characterization. (a) Ellipsometry fitting parameters (α,β) of spin-coated PEI layers of 30 nm and 9 nm on Si substrates from two solutions with molecular weights of 0.76 wt% and 0.22 wt% in ethanol, respectively. Surface morphologies of the (b) 30 nm and (c) 9 nm PEI membranes are imaged with atomic force microscopy, both having approximate RMS roughness R_q~0.3 nm. (d) Extinction spectra showing the thermal desorption at 100°C of PEI on CaF_2 substrates of the 9 nm PEI film compared with the 30 nm PEI film.

An ultrathin polymer film has several advantages compared to its bulk counterpart. First, it avoids the absorption loss contribution of IR light penetrating in thicker polymers. In addition, it allows a shorter path diffusion length for gas species, thus yielding faster response during gas adsorption and thermal desorption processes. This may resolve the non-zero reference issue of bulk polymer film caused by incomplete desorption with stuck gas species. Fig 3.4d displays the spectral changes of the two PEI films when thermally desorbed at 100°C for 2 mins in ambient air. Three prominent peaks at 1304, 1475, and 1565 cm^{-1}, corresponding to HCO_3^- vibration, NCOO skeletal vibration, and C=O stretch, respectively, are more pronounced with the 30 nm film as expected with a higher interaction length. A flatter spectral response is observed with the 9 nm PEI film when heated, indicating an easier CO_2 desorption from the film. In this work, the 9 nm ultrathin PEI layer was

selected to functionalize the GNR surface as its thickness optimally matches the LSPR decay length of the graphene.

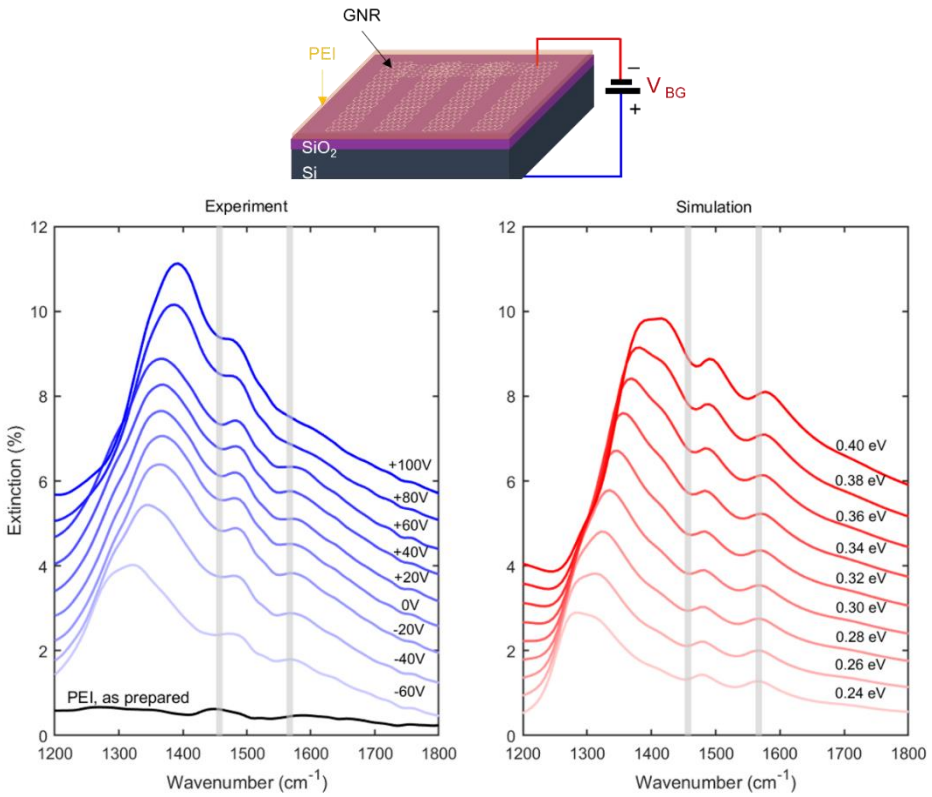

Figure 3.5: PEI-functionalized GNR surface characterization. [Top] Schematic of the sensor chip with PEI coating. [Bottom] Experimental and simulated LSPR responses of the GNR+PEI surface for varying V_{BG} and Fermi energy E_F, respectively. The spectrum of the PEI without GNR is displayed as a black curve. The grey lines indicate two prominent vibrational bands of the PEI.

The same GNR surface from Fig. 3.3 was functionalized with a 9 nm PEI layer, and a schematic of the sensor and the spectral characterization are shown in Fig. 3.5. The extinction plot of the PEI film without GNR (black curve) depicts two vibrational resonant peaks (highlighted grey) at around 1475 cm^{-1} and 1565 cm^{-1}, which appear as local dips in the LSPR

modes due to coupling. In addition, the LSPR grows in amplitude and blue-shifts with an increasing positive V_{BG}. Note that this enhancement with a PEI coating occurs in the opposite direction to the V_{BG} sweep with GNR only (the LSPR mode enhances toward a higher negative V_{BG} in Fig. 3.3). This is due to an induced n-doping of the graphene by the amine-rich PEI polymer, as discussed in Section 2.2.3. The LSPR mode is visible even at V_{BG} =-60 V indicating that the initial slightly p-doped state (hole charge carriers) of the graphene has converted to a substantial n-doped level (electron charge carriers).

The reversal of the graphene doping type is examined by evaluating the shift in Fermi level upon PEI coating. The graphene Dirac cone in Fig. 3.6a represents the shift in Fermi levels for the as-prepared GNR (p-doped) in the valence band towards the conduction band after coating with the PEI layer (n-doped). The experimental LSPR modes at $V_{BG} = 0$ in Fig. 3.6b depicts the LSPR enhancement after PEI-coating on GNR. By comparing experimental and simulated spectra, we can estimate the CNP of graphene with a PEI layer. The extinction spectra against varying E_F values were simulated using the same geometrical parameters as the fabricated graphene nanostructures used in the experiment. The PEI permittivity was obtained by analytically fitting the experimental transmission data of 9 nm PEI on a CaF_2 substrate (Fig. 3.7a). The Lorentz model in Equation 2.9 was used with 5 coupled oscillators corresponding to PEI vibrational bands within the 1200-1800 cm^{-1} range. The PEI complex permittivity obtained from the fitting (Fig. 3.7b) was used to produce the simulated LSPR plots in Fig. 3.5. The experimental LSPR mode at $V_{BG} = 0$ is comparable to the simulated spectrum at $E_F = +0.32\ eV$, which roughly correspond to locate the CNP of GNR+PEI around $V_{CNP} = -80\ V$. We calculated the $E_F - V_{BG}$ Dirac curves in Fig 3.6c using Equation 2.3. This visualizes the shift in CNP with slightly p-doped as-prepared GNR ($V_{CNP} = +20\ V$) and n-doped PEI-coated GNR ($V_{CNP} = -80\ V$).

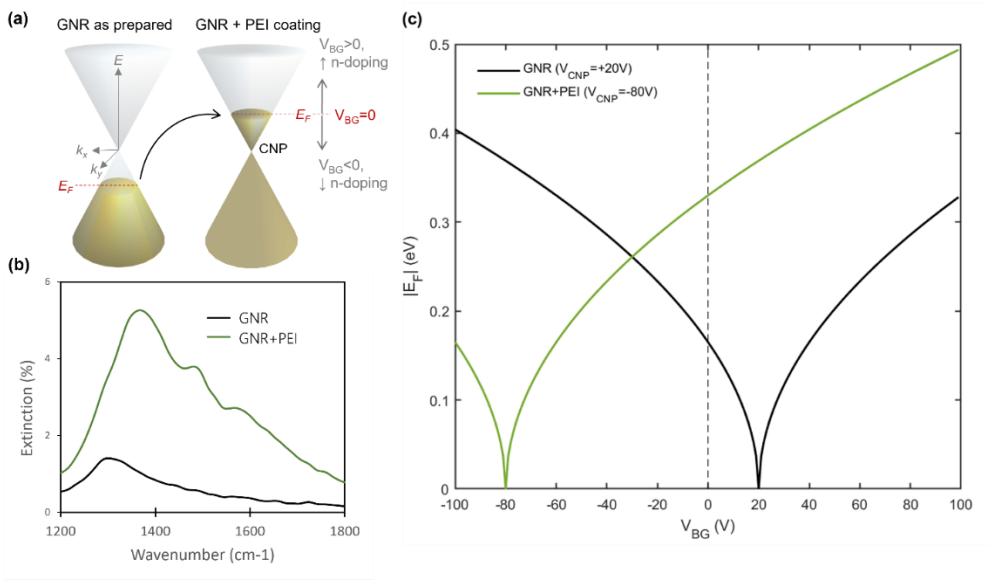

Figure 3.6: Graphene chemical doping induced by PEI. (a) Schematic of Fermi levels in a Dirac cone for as-prepared GNR (p-doped) and after PEI coating (n-doped). (b) Extinction spectra at $V_{BG} = 0V$ of as-prepared GNR and after PEI coating. (c) Fermi Energy E_F versus V_{BG} of as-prepared GNR and PEI-coated GNR.

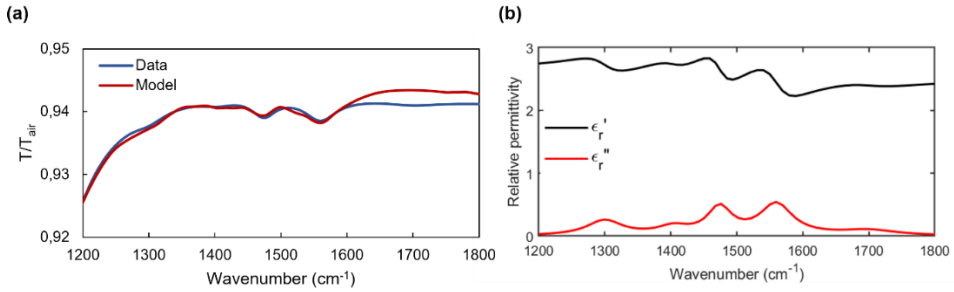

Figure 3.7: 9 nm PEI permittivity. (a) Experimental and fitted transmission spectra of 9 nm PEI on a CaF_2 substrate. (b) Extracted relative permittivity $\epsilon = \epsilon_r' - i\epsilon_r''$ from the fitted transmission data.

3.3 Graphene Plasmonic Response with CO_2

The optical response of the proposed sensor against different CO_2 levels is illustrated in Fig. 3.8a. The V_{BG} is fixed at $+100\,V$ to allow for a large

extinction and maximum overlap of LSPR with the PEI vibrational bands. The range of CO_2 is varied, from an ambient atmospheric level (~390 ppm) to higher levels, which is monitored by a commercial CO_2 sensor. For comparison, the spectra on PEI without GNR are recorded in Fig. 3.8b at the same CO_2 exposure levels and displayed using the same extinction scale. In the case with only PEI, an increase in absorption intensity of the PEI bands is observed in response to increasing CO_2 concentrations. This is in contrast to the case with GNR+PEI, where an appreciable change in the LSPR mode, comprising of two coexisting transduction mechanisms, resulted from varying CO_2 levels. First, the local dips appearing in the LSPR indicated by grey lines are the enhanced PEI vibrational bands – the so-called SEIRA effect. Second, the LSPR is greatly tuned with varying CO_2 levels via PEI-induced chemical doping of the graphene, which we highlight as the novel sensing mechanism in our study. Note that these modulations were not seen in the control experiment (Fig. 3.9), which was conducted by exposing the GNR surface directly with different CO_2 concentrations. No detectable change is observed in the LSPR modes in the considered range. Thus, PEI as a functional layer enhances the gas detection with surface-based sensing in our works by both selectively adsorbing and concentrating the gas inside the near field plasmon polariton of graphene nanostructures.

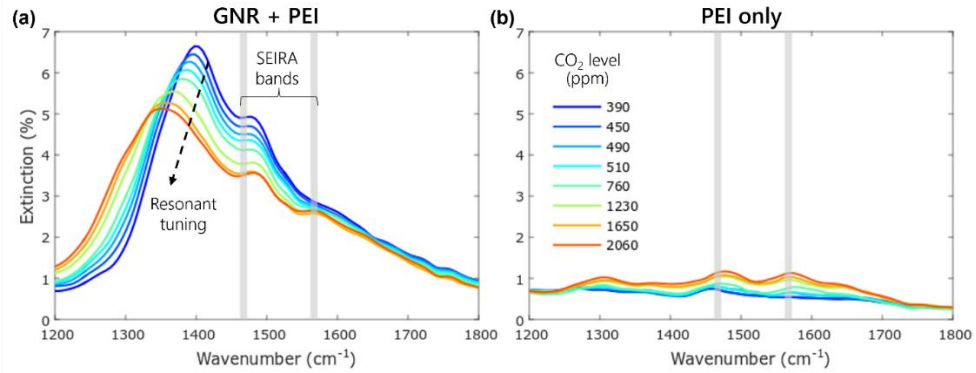

Figure 3.8: CO_2 sensing experiment for GNR+PEI. Extinction spectra of (a) GNR+PEI and (b) PEI only exposed to varying CO_2 ppm levels. The grey bands indicate the spectral locations of 2 prominent PEI vibrational bands.

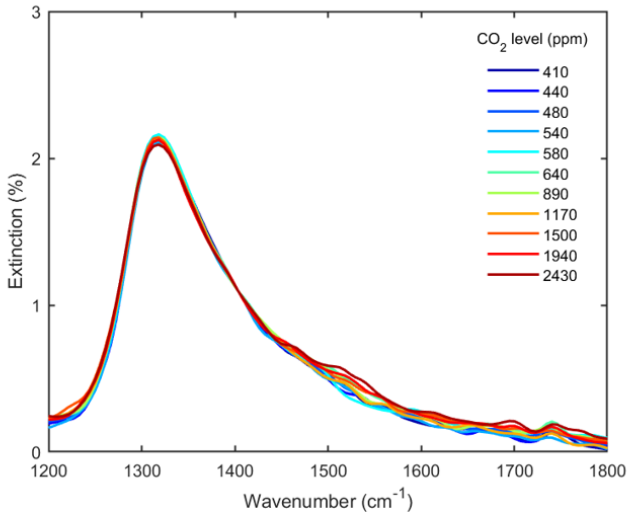

Figure 3.9: CO_2 sensing control experiment. Extinction spectra of GNR (45 nm width and 80 nm period) without PEI functionalization, exposed to different CO_2 ppm levels.

To illustrate the SEIRA effect, Fig. 3.10 shows the representative measured spectra of GNR+PEI and PEI only at 2060 ppm. Here, the graphene LSPR (grey curve) and PEI vibrational resonances (red curves) are decoupled. The inverted spectrum of the PEI shows Lorentzian peaks that appear as local dips within the LSPR of the GNR+PEI. This reveals the enhancement in pronounced Lorentzian resonant intensities. The cumulative spectrum of the GNR+PEI is expected to be less than its extracted pure LSPR counterpart because of the dissipative absorption of the PEI environment. Note that, quantification of the gas concentration through the intensity of the SEIRA vibrational bands requires a decoupling process of multi-Lorentzian peaks, which can be unpractical.

On the other hand, monitoring the LSPR modulation in response to CO_2 concentration offers more straightforward and simpler transduction than analyzing the SEIRA bands. The LSPR continuously redshifts and reduces in intensity for increasing CO_2 levels. This tuning is related to the reduction in graphene chemical doping as more amines (n-dopant) interact with adsorbed CO_2 in the PEI layer. A linear relationship is derived by plotting the LSPR peak position k_{LSPR} versus the logarithmic scale of

CO_2 concentration $\log(C_{gas})$, as shown in Fig. 3.11. The slope of linear fitting calculates the relative shift, yielding $\frac{\Delta k_{LSPR}}{\Delta \log(C_{gas})} = -63\ \frac{cm^{-1}}{ppm}$. This applies to the zone of linear response from an atmospheric CO_2 level (390 ppm) up to 2000 ppm (approaching the upper limit, as seen in Fig 3.12).

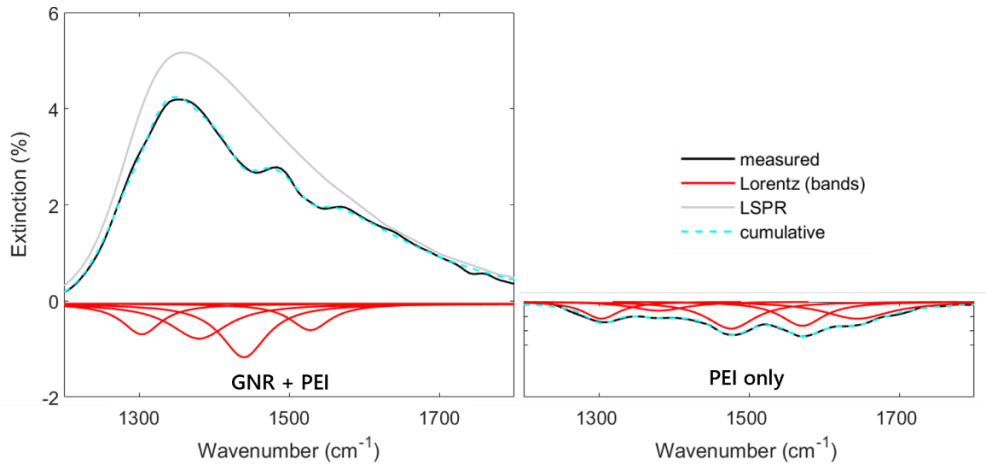

Figure 3.10: Decoupled SEIRA bands. The spectra of GNR+PEI and PEI only at 2060 ppm of CO_2 are displayed with extracted graphene LSPR and PEI Lorentzian vibrational resonances. The latter has an inverted spectrum for comparison on the same scale as the PEI bands.

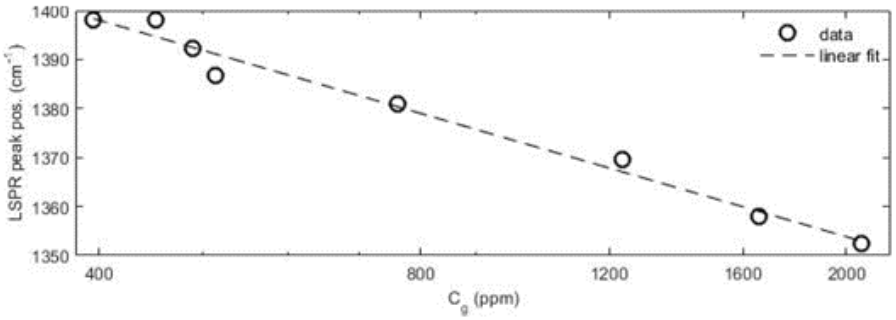

Figure 3.11: Derived linear relationship of the gas sensing response. LSPR peak position (cm^{-1}) as a function of CO_2 concentration (logarithmic scale in ppm).

Repeatability of the sensor's response to CO_2 ppm variations is examined for three cycles of measurements (Fig. 3.12). For each cycle, spectra are recorded while the sensor is exposed to increasing CO_2 ppm levels, and then the device is heated to thermally desorb the CO_2 gas from the PEI while continuously purging a flow of N_2 gas. The representative spectra for all cycles in the insets in Fig. 3.12 exhibit a consistent behavior as described previously: the LSPR peak reduces in intensity and redshifts upon exposure to higher CO_2 levels. The CO_2 concentration is extended to even higher ppm levels on days 2 and 20, where saturation is observed beyond 2000 ppm, indicated by a red dashed box. This region signifies that the gas sensing approached the upper limit, probably related to the limited CO_2 that can be adsorbed in an ultrathin PEI layer.

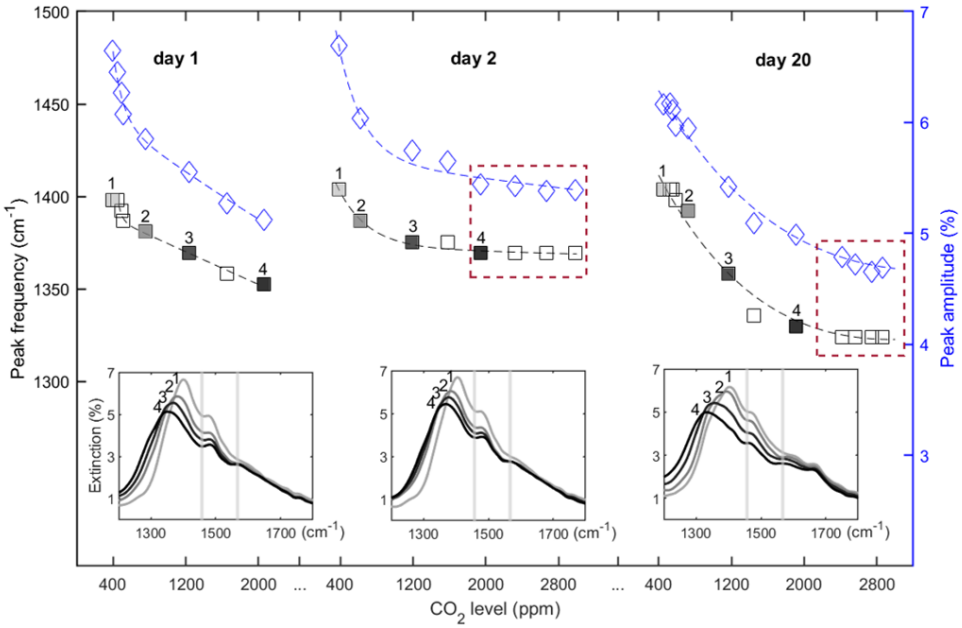

Figure 3.12: Repeatability experiments. Three measurement cycles recorded on different days displaying the extracted peak frequency and amplitude versus CO_2 gas concentration. The insets below represent extinction spectra for each cycle corresponding to indexed data points. The red dashed boxes show the saturation region.

As noted previously, the observed dynamic range of CO_2 concentrations forming a linear relationship in this system is between an ambient atmospheric level and 2000 ppm (refer Fig. 3.11). 1000 ppm is classified as a harmful level in indoor air quality monitoring, meaning that our system is already relevant for applications.[138] The deviations in the measurements can be reduced with better sealing of the gas cell to avoid leak exposure from the altering atmospheric conditions. Also, an extra PEI band appeared at 1684 cm^{-1} on day 20, which is associated with slow urea formation over time.[139] Thus, stabilizing the PEI coating from degradation (e.g., adding cross-linkers to the PEI solution[140]) could further improve the proposed sensor.

3.4 Conclusion

We have proposed a novel gas sensing platform based on mid-IR LSPR of graphene nanoribbons functionalized with an ultrathin gas adsorbing polymer. The CO_2-selective PEI polymer employed in this work enhances the detection by trapping the gas within the extremely confined near field of the graphene plasmons. Moreover, the PEI contains amines, which chemically n-dopes the graphene and eventually enhances the LSPR of the graphene nanoribbons. Two coexisting transduction mechanisms occur by the proposed sensor upon variations in CO_2 levels. First, the SEIRA effect is observed through enhancements in the intensities of the PEI vibrational bands coupled in the LSPR. Second, we elucidate a novel sensing transduction, where LSPR is modulated via graphene chemical doping and whose tuning is related to the doping level set by the adsorbed CO_2 in the PEI layer. The latter provides an efficient sensing mechanism and simpler transduction by just monitoring changes in the graphene LSPR (e.g., spectral shift or resonant intensity). Further study of graphene chemical doping assisted by a polymer could pave the way to gate-free graphene-based 2D sensors.

Chapter 4

Gas Sensing with hBN Phonon Polaritons

Bareza, N. Jr., Paulillo, B., Slipchenko, T., Autore, M., Dolado, I., Liu, S., Edgar, J. H., Vélez, S., Moreno, L.M., Hillenbrand, R., Pruneri, V. "Phonon-Enhanced Mid-Infrared CO_2 Gas Sensing Using Boron Nitride Nanoresonators," ACS Photonics, 2022: 9(1), 34-42.

Polar van der Waals dielectrics offer an exciting paradigm in the field of nanophotonics as their mid-IR PhP support extreme light confinement and long lifetimes.[35,41,43,141–143] PhP modes occur from the coupling between IR light and crystal lattice vibrations in the material. For instance, nanostructured hBN hosts high quality-factor Q resonances which have attracted attention in SEIRA spectroscopy. Sharp resonances ($Q \sim 10^2$) of natural[43] and monoisotopic[41] hBN nanoresonators were shown to perform molecular sensing at the strong coupling limit.[42,75] This chapter demonstrates phonon-enhanced mid-IR CO_2 sensing using nanoribbons made of monoisotopic hBN, which are functionalized with CO_2-adsorbing thin film of PEI polymer. By collecting the far-field transmission spectra of the PEI-functionalized hBN nanoribbons, we show PhP resonance modulation, dependent on the CO_2 concentration. We also demonstrate a reversible optical response by thermally desorbing CO_2 molecules from the PEI. The proposed hybrid material sensing platform displays a high signal-to-noise ratio (SNR), despite measuring small ribbon arrays of 30x30 μm^2, which finds potential applications as miniaturized systems of indoor air quality (IAQ) monitoring and smart ventilation.[9,144]

4.1 Phonon-Enhanced Gas Sensing Scheme with hBN Nanoribbons

This section details the construction of IR-based gas sensing setup and the fabrication of proposed phonon-enhanced hybrid-material sensor chip. The sensor chip consists of hBN nanoribbons and functionalized with a thin film membrane of CO_2-adsorbing PEI polymer.

The gas sensing scheme is similar to that shown in Fig. 3.1. of the previous chapter, where a customized gas cell was coupled to a FTIR microscope system. Fig. 4.1 shows the gas sensing scheme, where fabricated sensor was placed on a heating stage inside the gas cell. The incoming IR light was polarized perpendicular to the long axis of hBN ribbons for PhP excitation. Far field transmission spectra were collected with 100 averaged scans, with a resolution of 4 cm^{-1}. The extinction was calculated as $1 - \frac{T}{T_0}$, where T and T_0 represent the transmission spectra with and without hBN+PEI, respectively.

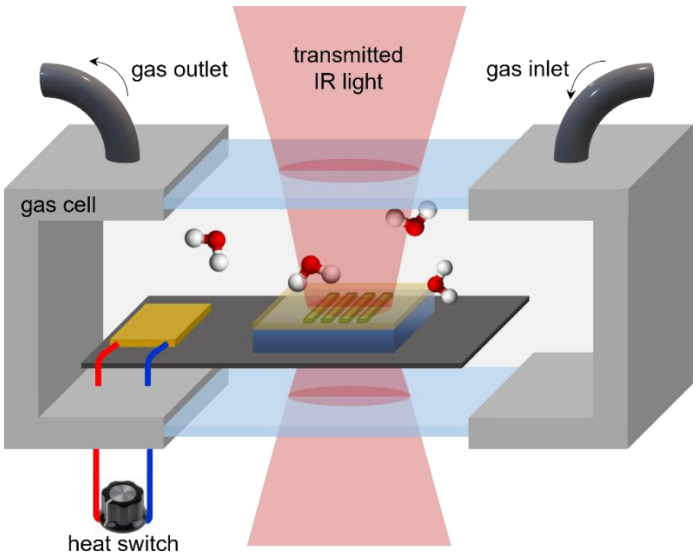

Figure 4.1: Schematic diagram of the gas sensing setup. The sensor chip mounted on a heating stage is placed inside a gas cell, equipped with valves for gas flow and IR-transparent windows for transmission measurement with an FTIR microscope.

Fig. 4.2a shows a sketch of the conceptualized sensor layers. First, ^{10}B enriched hBN crystal was grown using the metal flux method (details in reference [145]) by the collaborators from *Kansas State University*. Then, the collaborators from *The Basque Nanoscience Cooperative Research Center (CIC NanoGUNE)* fabricated the hBN nanoribbons. A large homogenous monoisotopic hBN flake was mechanically exfoliated, then dry-transferred onto an IR-transparent CaF_2 substrate. Next, high-resolution electron beam lithography (EBL) was performed to fabricate several 30x30 μm^2 array elements of different ribbon widths with a fixed period of 400 nm. Lastly, the nanostructured hBN was functionalized with a thin film of PEI polymer. The cross-section schematic of the sensor in Fig. 4.2a illustrates the chemisorption of the CO_2 molecules interacting with amine groups in the PEI layer. The PEI film can be regenerated by heating the sensor chip >85 ℃ to thermally desorb the CO_2 gas.[65,110,111]

A representative array of the EBL patterned hBN nanoribbons before PEI coating was characterized with SEM and AFM depicting a ribbon geometry of 400 nm period and 30 nm thickness (Fig. 4.2b/c). Surface defects and inhomogeneities are observed in the SEM micrograph, which could contribute to increased polaritonic scattering, consequently broadening the PhP resonances.

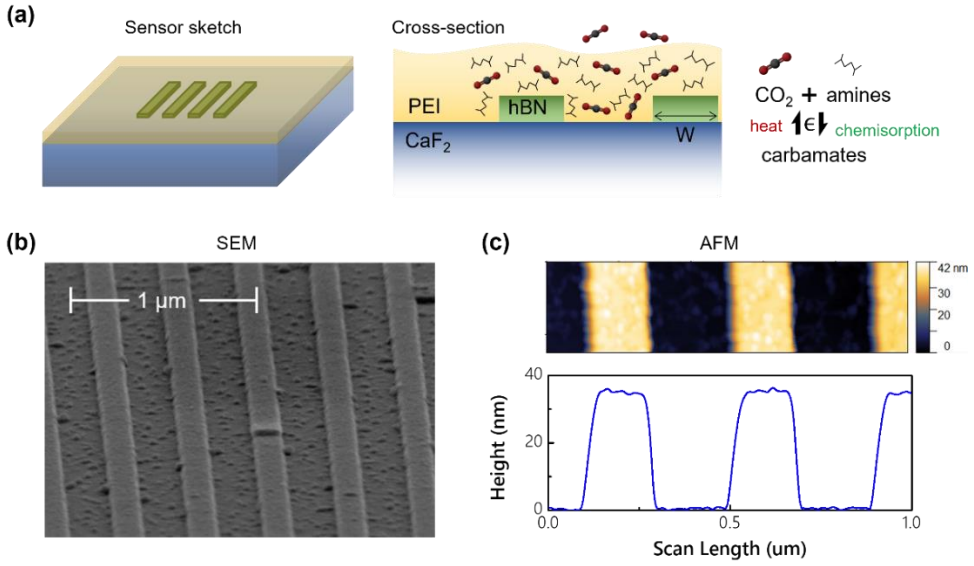

Figure 4.2: hBN-based gas sensor chip and structural characterization. **(a)** Schematic of the proposed sensor chip comprised of fabricated hBN nanoribbons on a CaF2 substrate and functionalized with a PEI coating. The basic reaction is illustrated by reversible chemisorption and thermal desorption of CO_2 gas in the amine-rich PEI layer. **(b)** SEM and **(c)** AFM characterizations of EBL patterned hBN nanoribbons.

The extinction spectra of the EBL patterned hBN nanoribbons were first investigated prior to PEI functionalization. Fig. 4.3 compares the transversal volume confined PhP modes produced from two ribbon geometries, with high extinction (~30%) and sharp (achieving Q~80) PhP resonances occurring above the transverse optical (TO) phonon position. Wider ribbons shifted the PhP resonance towards a lower wavenumber as expected from geometrical tuning. For comparison, the extinction spectrum of PEI directly deposited on a substrate (solid grey curve) displays weak band intensities. The rescaled plot (dashed grey curve) enables us to show the overlap of a prominent vibrational fingerprint (~1470 cm^{-1}) with the PhP resonances.

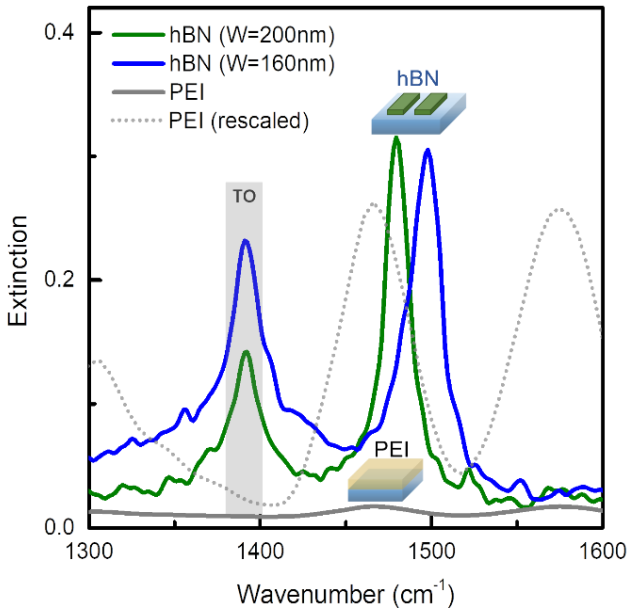

Figure 4.3: Fabricated hBN surface characterization. Experimental extinction spectra of hBN nanoribbons of two different ribbon widths with the same 400 nm period. The PhP modes occurred above the TO phonons (grey highlight). For comparison, the extinction spectrum of PEI (75 nm thick) deposited directly on CaF_2 substrate is also displayed (solid grey curve) including its rescaled plot (dashed grey curve).

4.2 Effect of PEI Functionalization on hBN Nanoribbons

Functionalizing the 2D nanostructures with gas-adsorbing thin layer generally enhances the interaction between gas molecules and surface bound polariton fields. Hence, depositing a thin PEI film on top of hBN nanoribbons would enhance the near field interaction by concentrating the adsorbed CO_2 molecules within the PhP field volume penetrating in the PEI layer.

The thickness of the PEI film should optimally match the field decay length of the highly confined PhP modes of the hBN nanoribbons. We formulated a PEI solution that could yield a film thickness to cover the

majority of the field decay length (e.g., in reference [[75]], an 85% field is confined 30 nm from the top surface of the hBN nanoribbons). The hBN thickness (determined experimentally to be 30 nm, as shown in the AFM in Fig. 4.2c) should be considered when estimating the overall PEI thickness. A 1.58 wt% solution of branched PEI (M_w~2500 from Sigma Aldrich) diluted in ethanol was prepared, and after magnetic stirring, the solution was spin-coated on a silicon substrate at 5000 rpm. Then, the sample was baked at 100 ℃ for 2 mins to further evaporate the ethanol solvent. From ellipsometry fitting (Fig. 4.4a), the thickness of the PEI film was determined to be 75 nm, which is able to entirely cover the hBN nanoribbons (around 30 nm thick based on AFM in Fig. 3.2c). In estimate, the remaining thickness on top of hBN is ~45 nm that matches the PhP field decay length.[75] Such PEI solution was deposited on top of hBN nanoribbons. The resulting surface morphology in AFM image depicts a planarized film with small undulation of around 2 nm peak-to-peak amplitude (Fig. 4.4b).

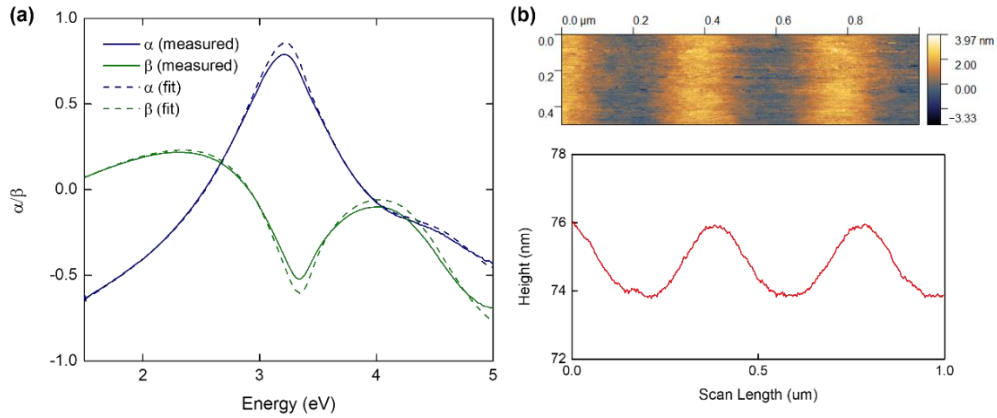

Figure 4.4: Thin PEI characterization. (a) Ellipsometry fitting parameters (α, β) of a spin-coated 75 nm PEI layer on Si from a 1.58 wt% solution prepared in ethanol. (b) AFM measurement of PEI coated hBN nanoribbons.

The optical response was investigated for different hBN nanoribbon geometries upon addition of the thin PEI film. The measured PhP resonances redshift and broaden upon PEI coating in two representative

arrays of different ribbon widths, as observed in Fig. 4.5a. This is consistent with other ribbon widths, where similar trends can be seen. This is shown in Fig. 4.5c, which plots the extracted experimental Q's and peak positions of PhP resonances before (blue) and after (red) PEI coating. This clearly demonstrates decreased Q's and redshifted peak positions of the PhP resonances after PEI coating. This damping effect could be explained by the coupling of the PhP resonance with much broader vibrational resonance of PEI molecules.

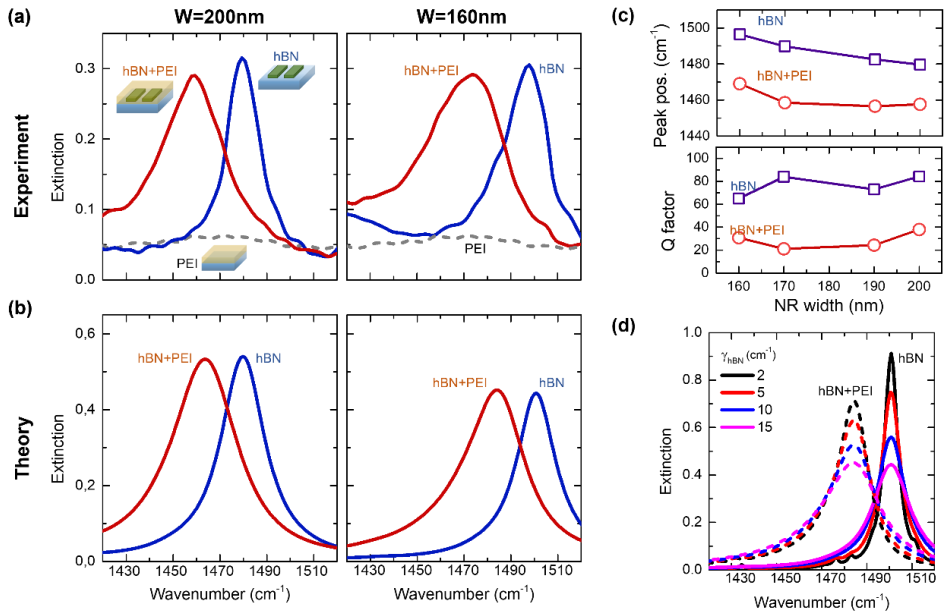

Figure 4.5: PEI-functionalized hBN nanoribbon surface. (a) Experimental and (b) simulated extinction spectra of hBN nanoribbons before (blue curves) and after (red curves) 75 nm PEI coating for two ribbon widths with the same 400 nm period. The experimental spectrum for bare PEI on CaF_2 is also displayed for comparison (dashed grey curves). (c) Resonant peak positions and Q's extracted from experiments for various fabricated ribbon widths before (blue curves) and after (red curves) PEI coating. (d) Simulated PhP resonances for hBN nanoribbons of width 160 nm for different hBN damping values before (solid curves) and after (dashed curves) PEI coating.

Full wave electromagnetic simulations were performed using finite-element methods (COMSOL software) by the collaborators from *Spanish National Research Council* (*CSIC-Universidad de Zaragoza)*. The permittivity of 75 nm PEI was taken by fitting the Lorentz model with three coupled oscillators with the experimental transmittance spectra of the PEI layer deposited on CaF_2 (Fig. 4.6). Here, subsequent measurements were collected for different CO_2 level concentrations. The fitted spectrum at 390 ppm (exposure at ambient atmospheric CO_2 level) corresponds to the as-prepared PEI layer. The dielectric function of the hBN, obtained in single-Lorentzian form (Equation 2.4), was analytically fitted with the experimental transmission spectrum of a non-patterned hBN flake on CaF_2. To closely examine the losses of the PhP modes in the presence of PEI, the hBN damping factor γ_{hBN} was varied in the permittivity model for a representative ribbon array (width = 160 nm), as shown in Fig. 4.5d. For relatively low γ_{hBN} values, a significant drop in the extinction and a broadening of the PhP modes were observed. Our experiments can be reproduced using γ_{hBN}= 15 cm^{-1}, where the addition of PEI results in a PhP mode with similar extinction but with substantial broadening. This γ_{hBN}= 15 cm^{-1} value was applied to numerical simulations in Fig 4.5b, with the trend agreeing with the experimental results. However, the simulated extinction peak intensities were higher compared with those in the experiments, which can be attributed to scattering due to non-uniformity and defects of the fabricated hBN nanoribbons.

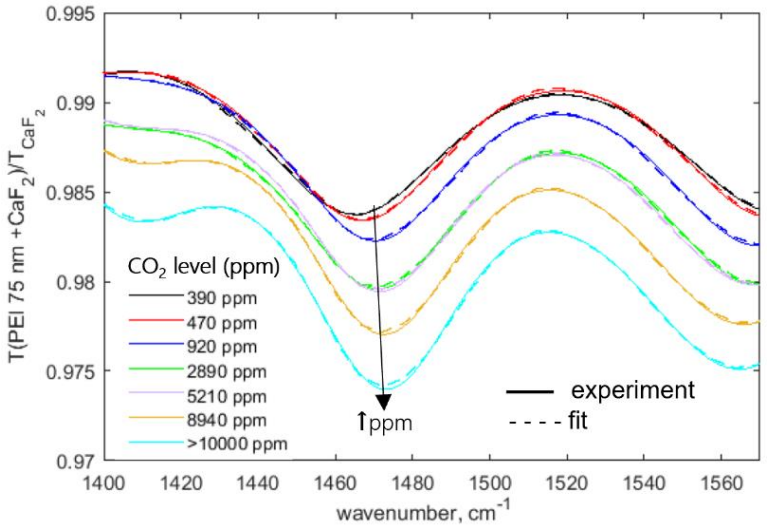

Figure 4.6: 75 nm PEI permittivity. Experimental (solid) and numerically fitted (dashed) spectra of 75 nm PEI on CaF_2 exposed at different CO_2 ppm levels.

4.3 hBN PhP Response with CO_2

The optical response sensitivity of the proposed sensor to CO_2 gas exposure is presented in Fig. 4.7. The experimental PhP mode of PEI-coated hBN nanoribbons with 160 nm width nearly overlaps the PEI vibrational fingerprint at 1470 cm^{-1}, thus this geometry is monitored in the experiment. The range of CO_2 injected in gas cell (Fig. 4.1) is varied from an ambient atmospheric level (~390 ppm) to higher levels, beyond the classified harmful scale (>1000 ppm) in IAQ monitoring.[138]

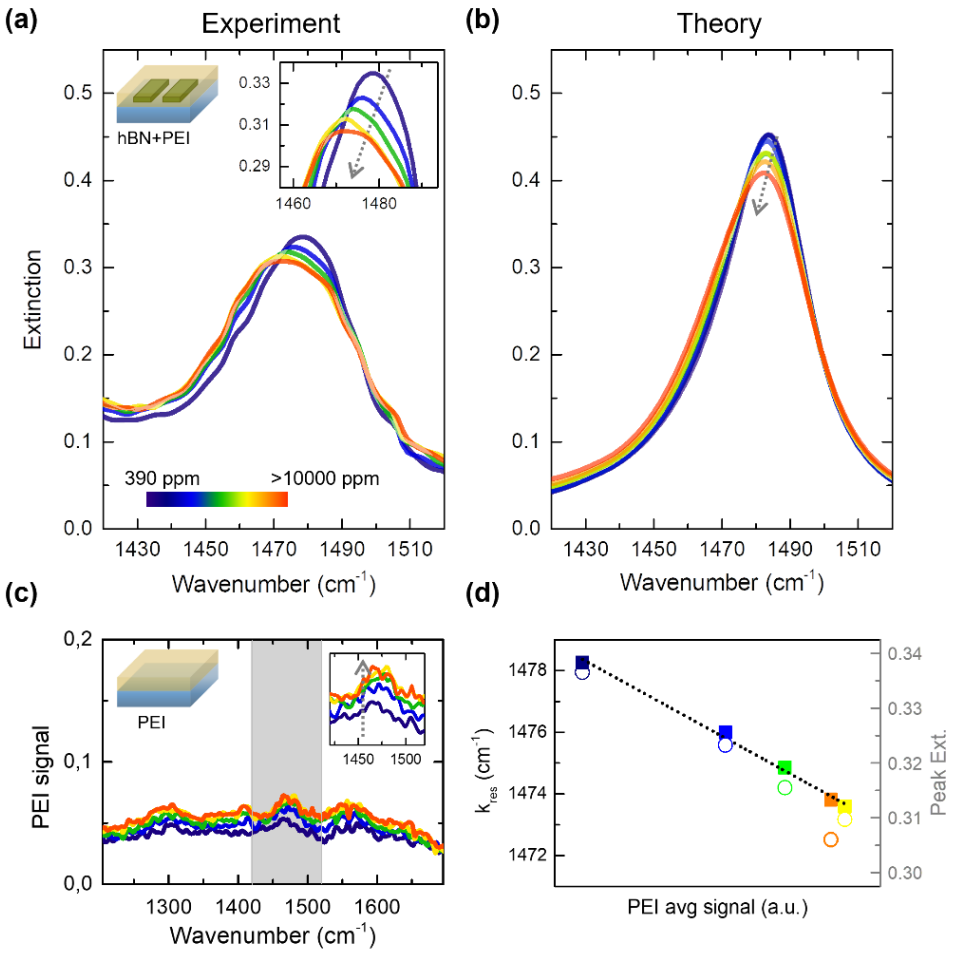

Figure 4.7: CO_2 sensing experiment of hBN+PEI. (a) Experimental and (b) simulated extinction spectra of hBN (width=160 nm)+PEI with varying CO_2 ppm levels (grey dashed arrow indicates the response toward increasing levels). (c) Extinction spectra of bare PEI on CaF_2 in response to the same CO_2 level variations in (a). Inset displays the zoom-in of the PEI vibrational band (grey shaded region). (d) Extracted experimental resonant peak position k_{res} (left axis, solid markers) and peak extinction (right axis, open markers) as a function of the average PEI signal in (c).

The experimental PhP resonance (Fig. 4.7a) redshifts, broadens, and weakens at increasing CO_2 ppm levels. The PEI vibrational band intensities strengthen as the PEI layer adsorbs the CO_2 gas at a particular increased concentration level. The PhP mode probes the variation of dielectric

function in the PEI layer in its vicinity, which results in a modulation of the PhP resonance for varying CO_2 levels. The simulated spectra produced in Fig. 4.7b were acquired by using the PEI permittivity model as a function of CO_2 nominal levels, corresponding to fitted model in Fig. 4.6. The theory shows good agreement with the experimental trends, except with overall lower extinction peaks in the experiments, which is related to fabrication defects. Note that these modulations were not seen in the control experiment by directing CO_2 gas to the surfaces of hBN nanoribbons without a PEI coating (Fig. 4.8). The small amplitude variation in the control experiment could be due to unstable measurements from a small aperture (25x25 μm^2) focused on the area of the hBN sensing array element. No trend of PhP mode as a function of gas concentration is observed due to almost negligible adsorption of gas molecules at hBN nanostructures. This proves that solely relying on gas physisorption on 2D materials is ineffective due to the highly dispersive state of gas molecules.

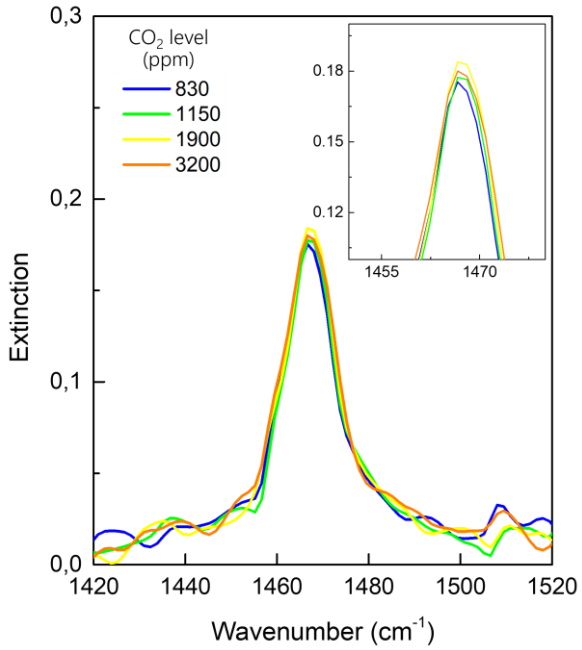

Figure 4.8: CO_2 sensing control experiment. Extinction spectra of hBN nanoribbons (width w=190 nm, period p=400 nm, flake=20 nm) without PEI functionalization exposed with different CO_2 ppm levels.

For comparison, the spectral responses of PEI on CaF_2 were recorded at the same CO_2 exposure levels and the same 30x30 μm^2 aperture size used when measuring the hBN array element. This resulted in a poor SNR due to the small footprint size of the measurements, as shown in Fig. 4.7c. However, the PhP resonant modulations were able to transduce the CO_2 levels with a cleaner SNR, a clear advantage of utilizing the low-loss and highly confined hBN PhP modes. The hBN+PEI surface provides a large SNR enhancement with respect to PEI alone. The spectral noise floor was estimated as N ~ 0.3%, yielding S/N ≥100 for the hBN+PEI surface and S/N ≤10 for the bare PEI, i.e., an SNR improvement of more than 10x. Further improvements can be expected by expanding the footprint size of the hBN array element and reducing the fabrication defects (e.g., with a comprehensive study of the formulating recipe for more uniform hBN etching).

The overall PhP modulation in the explored concentration range is quantified by plotting the extracted peak positions and extinctions as a function of averaged PEI signals. We have an estimated spectral shift of 4 cm^{-1} and an extinction drop of 10% relative to the peak value in the explored range, as presented in Fig. 4.7d. The overall spectral shift is somewhat small and is already equivalent to the FTIR resolution used in the experiments. In contrast, the changes in extinction occur at one order of magnitude higher than the noise level (estimated as N ≈ 0.3%), and as mentioned earlier, the SNR can be further improved with a larger sensing area. Hence, monitoring the intensity changes in the PhP mode is expected to be more operable for smaller changes in CO_2 concentration.

Next, we examine the repeatability of the optical response. The sensor response is monitored in cycles on different days with subsequent CO_2 adsorption and thermal desorption. As discussed previously and shown in Fig. 4.2a, adsorbed CO_2 reacts with amine groups of PEI to form carbamate. The PEI is regenerated by heating it at 95 ℃ for 2 mins with a continuous N_2 gas flow, causing the carbamate to dissociate and the amine-sorbents to be recovered, while releasing the CO_2 gas. Fig. 4.9a illustrates the repeatable response over several days, showing that the

change in PhP resonance for higher CO_2 ppm is consistent with that previously described. Moreover, thermal desorption returns the PhP mode to its as-prepared state (exposure to ambient atmospheric CO_2).

Finally, Fig. 4.9b demonstrates the reusability of the sensor. After 8 months, the PEI layer is removed using O_2 plasma etching, and the PhP resonance still retains its frequency position at higher wavenumber for bare hBN nanoribbons. A new 75 nm PEI coating on top produces the same trend of redshifted, broadened and weakened PhP resonance.

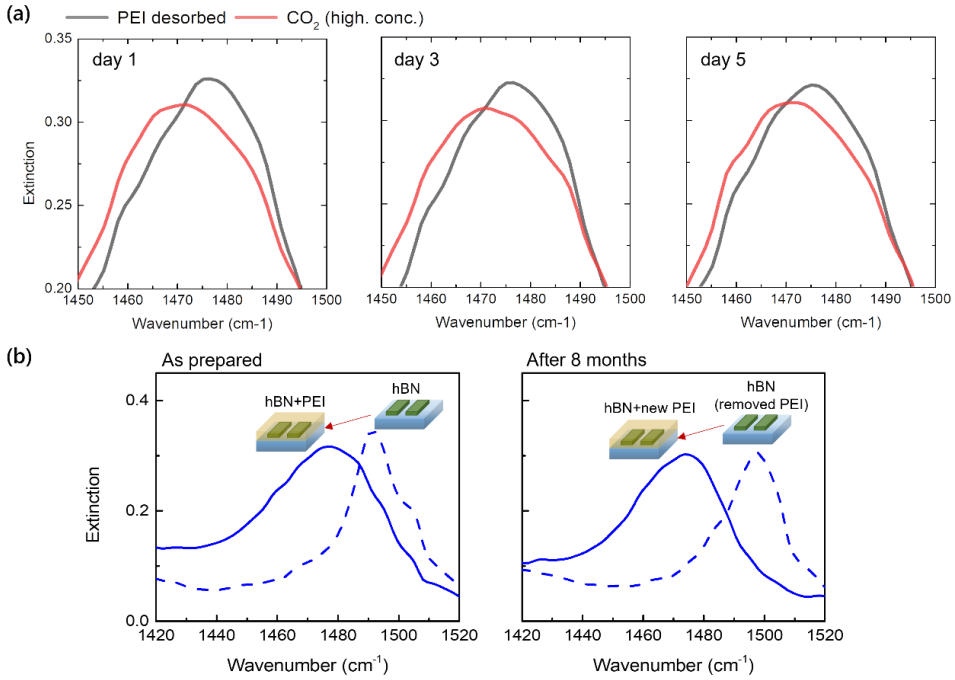

Figure 4.9: Repeatability and reusability experiments. (a) Extinction spectra of hBN+PEI on different days upon PEI thermal desorption (grey curves) and exposed at higher CO_2 level (red curves). (b) Extinction spectra of hBN nanoribbons with and without a PEI layer for first time use (left), and following removal of the old PEI layer and coating with a new PEI layer after 8 months (right).

4.4 Conclusion

We have demonstrated mid-IR gas sensing based on monoisotopic hBN nanoribbons functionalized with thin CO_2-specific PEI polymer. The top thin PEI layer improves the sensitivity by bringing the CO_2 adsorbed molecules within the highly confined PhP field. In this system, the PhP resonance redshifts, broadens, and weakens with increasing CO_2 concentrations. This resonant modulation is influenced by the changes in the local refractive index of the PEI dependent on CO_2 ppm concentration. In addition, the sharp and high extinction PhP resonance allows us to detect these local changes with a high SNR, even for a small sensing area of only 30x30 μm^2. Our results show that a miniaturized SEIRA gas sensor platform could be developed with PhP-enhanced nanostructured hBN.

Chapter 5

Quantitative Bioassay with Graphene Plasmons

The content of this chapter is currently under consideration for submission of a journal paper:

Bareza, N. Jr., Wajs, E., Paulillo, B., Tullila, A., Jaatinen, H., Milani, R., Dore, C., Mihi, A., Nevanen, T.K., Pruneri, V. "Quantitative mid-infrared plasmonic biosensing based on scalable graphene nanostructures," [Manuscript for journal submission].

Graphene has attracted a lot of attention for use in biosensing applications due to its versatile functionalization methods with different biomolecular building blocks (e.g., enzymes, proteins, and DNA), and also because of its flexible transducing principles (e.g., conductivity changes in field effect transistor, absorption enhancement as fluorescent quencher, and plasmonic resonant tuning).[66,133,135] For instance, graphene nanostructures that generate highly confined mid-IR plasmons show promising potential for tunable and surface-enhanced plasmonic sensing applications.[39,54,59,72] Rodrigo et. al. demonstrated qualitative label-free detection of proteins by way of the coupled amide frequency bands in the LSPR of graphene nanoribbons (GNR).[54]

Our objective is to report a quantitative bioassay using a graphene-based mid-IR plasmonic system with a relevant bio-functionalization. A bioassay comprising small biomolecular components is considered, which in principle should be within the extension of the plasmonic field decay length of graphene nanostructures (typically $\ell_d = 10 - 15\ nm$)[54,59] In our system, we functionalize the fabricated GNR with a pyrene linker (Py) via

$\pi - \pi$ stacking. This subsequently binds with an anti-vB12 antibody fragment (Fab), an antigen-binding component that attaches to pyrene via an amide bond. The Py+Fab acts as a bioreceptor for the recognition of a vitamin B12 (vB12) analyte. By displaying the extinction spectra from IR transmission measurements, we observe the LSPR modulation: (i) for each additional biomolecular layer (Py, Fab, and vB12), and (ii) for different vB12 concentrations. We also test the system with large-scale nanoimprinted graphene nanoholes (GNH), and we find consistent result-trends in the LSPR responses. Our quantitative bioassay using mid-IR graphene plasmons could be further extended by either using different sets of immunosensors (small receptor-biomarkers) or by employing other hybridized graphene metasurfaces that possess more robust and higher extinction LSPR modes.[146–148]

5.1 Plasmonic-Based Biosensing with Graphene Nanoribbons

This section details the IR biosensing setup and the fabricated graphene-based plasmonic sensor chip with considered bioassay. Fig. 5.1 illustrates the schematic diagram of the biosensing scheme, where optical measurements were done using FTIR microscope system. The sensor chip consists of GNR on SiO_2/Si substrate (fabrication described in Fig. 3.2) with configured electrostatic back-gate voltage V_{BG} for active tuning of the graphene LSPR. The sensor chip, divided into several sensor array elements, is mounted on a moving stage that enables to scan different sensor surface when performing transmission measurements. A single unit of bioassay on GNR is sketched, which composed of Py, Fab, and vB12. The Fab used is a recombinant protein, engineered and provided by the collaborators from *Technical Research Centre of Finland* (*VTT*).

In the optical measurements, the IR light was polarized perpendicular to the long axis of the graphene ribbons for the LSPR excitation, and far field

transmission spectra were collected by a liquid nitrogen-cooled mercury-cadmium-tellurium (MCT) detector. In order to acquire the extinction spectra $\left(1-\frac{T}{T_0}\right)$, subsequent measurements were taken, with 100 averaged scans with a resolution of 16 cm^{-1} per region on GNR+bioassay (T) and a bare substrate (T_0).

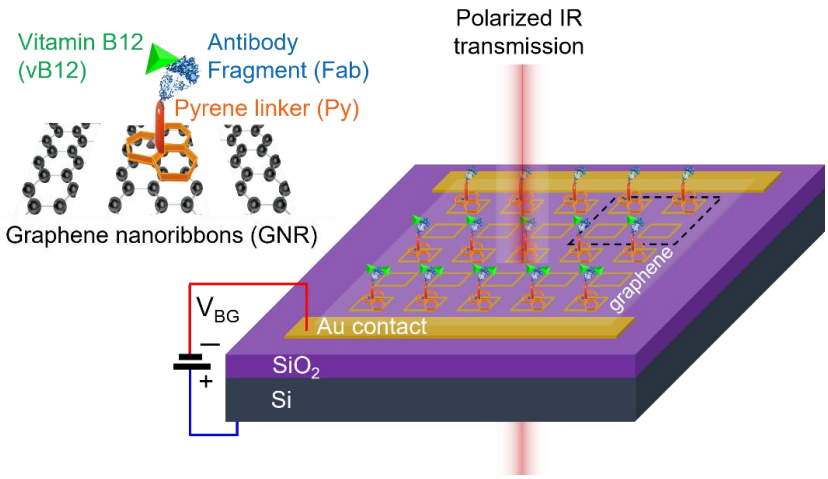

Figure 5.1: Schematic diagram of the biosensing setup. A sensor array of GNR on an SiO_2/Si substrate is configured with a supply of back-gate voltage V_{BG}. The sensor chip is mounted on a moving stage in order to scan the sensor elements when measuring the IR transmission using an FTIR microscope. A single-unit of bioassay is illustrated, comprising a pyrene linker, an antibody fragment (receptor) and vitamin B12 (analyte).

The immobilization of the bioassay is illustrated in Fig. 5.2a. The sensor chip was first immersed in a freshly prepared solution of 1-Pyrenebutyric acid N-hydroxysuccinimide ester (5 mM in 100% methanol) for 2 hours at room temperature. This forms a self-assembly monolayer (SAM) of pyrene derivative on the graphene surface. Then, the sample was washed with methanol to remove any excess and unbound molecules. After this, the Fab solution (0.5 $mg \cdot mL^{-1}$ in PBS 7.4) was dispensed in a few μL-drops using a high-precision SCIENION sciFLEXARRAYER S3 spotter. After

30 mins of incubation at room temperature in the humidity chamber, the device was washed with Milli-Q water and then dried. After that, 100 mM ethanolamine solution at pH 8.5 was spotted and incubated for 10 mins to block the remaining active ester sites and subsequently washed with Milli-Q water and dried. Next, different concentrations of vB12 (0 to 1 $mg \cdot mL^{-1}$) were spotted on different sensor elements and incubated for 5 mins at room temperature in the humidity chamber. Lastly, the device was washed with Milli-Q water and dried for optical measurements.

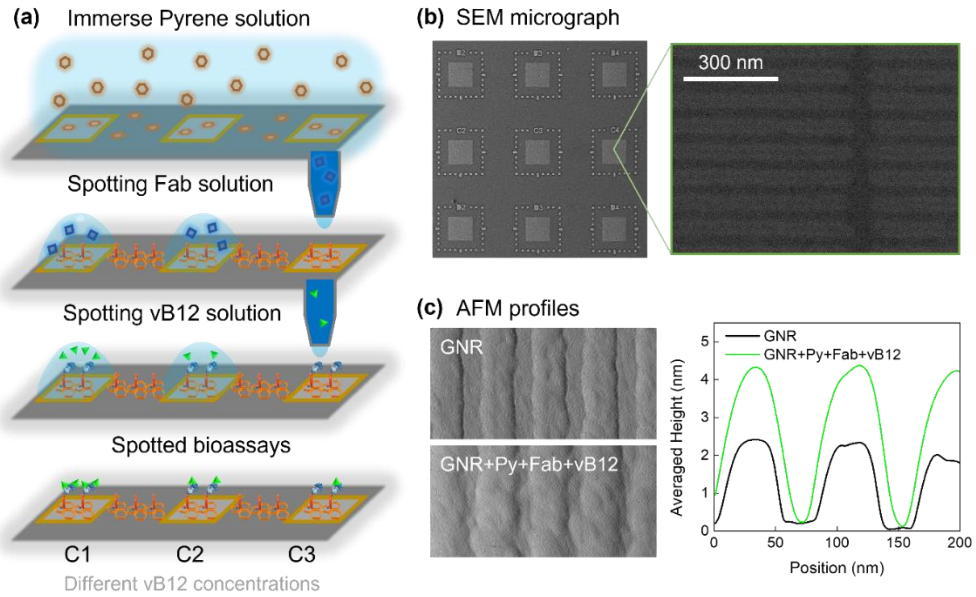

Figure 5.2: Schematic flowchart of the bioassay formation and sensor surface characterizations. **(a)** The sensor chip was immersed in a solution to immobilize the pyrene linker. After washing in methanol and Milli-Q water, subsequent spotting, incubation, and washing stages of Fab and then vB12 solutions were performed for each sensor element. Different concentrations of vB12 were assigned in the sensor array. **(b)** SEM micrograph images show a snippet of the sensor array, where light grey squares contain the GNR of width w=30nm and period p=80nm. **(c)** AFM characterization of the GNR surface before and after the bioassay formation.

The SEM micrograph in Fig. 5.2b shows that the sensor surface is divided into several elements of fabricated GNR (light grey squares with areal size of 240x240 μm^2) to accommodate different bioassay components on a single chip. The zoom-in image illustrates that the fabricated ribbons are electrically connected to have uniform bias upon gating. The AFM measurements in Fig. 5.2c confirm the presence of spotted biomaterials on top of GNR. The AFM image after the full bioassay immobilization (Py+Fab+vB12) shows irregular structures on top of the GNR indicating the presence of accumulated biomaterials. This is clearly demonstrated with a higher extracted average AFM height profile after adding the bioassay (green line) compared to GNR only (black line).

5.2 Bioassay: Characterization of Biomolecular Layers

The optical characterizations of the biomolecular layers that are successively added on non-patterned graphene and GNR (displayed in same y-scale to compare IR absorption) are presented by the experimental extinction spectra in Fig. 5.3. Noticeable changes in the spectral absorption are more obvious with the GNR surface biased at $V_{BG} = -100V$ (Fig. 5.3b) than with the non-patterned graphene (Fig. 5.3a). This is due to the absorption enhancement induced by the graphene LSPR.

The spectra for the non-patterned case have vibrational signal features, that are scarcely distinguishable from the noise. Nevertheless, the zoom-in plot in the inset (Fig. 5.3a) depicts the amide bands of Fab (1550 cm^{-1} and 1660 cm^{-1}) in blue highlights, as well as one apparent increased peak in green highlight at 1670 cm^{-1} that corresponds to the stretching of the propionamide side chain of the vB12.[149] Fig. 5.4 presents a closer investigation of the vibrational modes of the vB12 within the 1200-1700 cm^{-1} wavenumber region including its interaction with the Fab, for different concentrations. To yield higher vibrational signals, dried vB12 solutions are examined (Fig. 5.4a), wherein the precipitated vB12

biomolecules form single bound layers on top of the Fab. This results in more pronounced vibrational signals due to the large interaction length of the vB12 with the transmitted IR light, where intensities are directly related to concentration levels. Table 5.1 summarizes the frequency assignments of the vibrational modes, which include the most intense peak at 1670 cm^{-1} and other weaker band signatures. In our sensing experiments, the spotted solutions of vB12 were washed after 5 mins of incubation in a humidity chamber, enabling the specific binding of the vB12 analyte with the Fab receptor (Fig. 5.4b). As expected, this showed weaker signals due to a smaller interaction of the IR light with fewer vB12 biomolecules. Nevertheless, the vibrational signals are also present with intensities directly related to the vB12 concentrations.

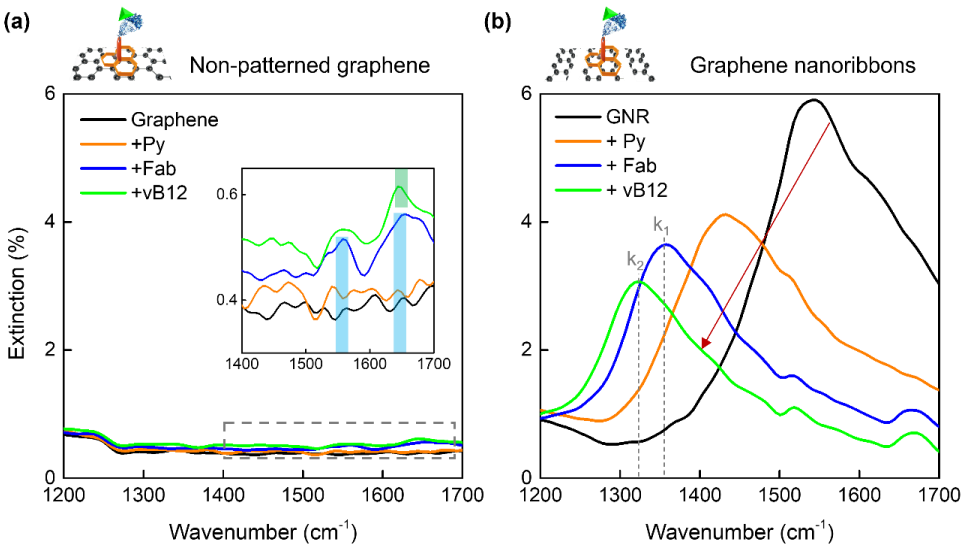

Figure 5.3: Optical characterization of biomolecular layers. Extinction spectra are displayed for the successive addition of biomolecular layers for (a) non-patterned graphene and (b) graphene nanoribbons. The inset in (a) shows a zoom-in of the vibrational bands (blue and green shaded regions for Fab and vB12, respectively). The red arrow in (b) indicates the shift in plasmonic response on addition of the biomolecular layers.

Table 5.1: Frequency assignments of vB12 biomolecules.[149,150]

Frequency (cm^{-1})	Assignment
1670	δ(C=O)
1570	δ(C=C)
1500	δ(C=C)
1475	δ(N—O)
1450	ϑ(C—H)
1400	δ(C—C)
1215	δ(C—O)

The optical responses shown in Fig. 5.3b exhibit prominent LSPR modulations for each subsequent addition of a biomolecular layer on the GNR, specifically reducing the amplitude and red-shifting the LSPR peaks. On addition of the Fab and vB12 layers, the LSPR peak positions are detuned from the highlighted vibrational band locations in Fig 5.3a. For instance, a small broad peak attributed to the amide band I ($\sim 1660\ cm^{-1}$) is situated on the pedestal of the LSPR of GNR+Py+Fab (blue curve). This implies that the plasmonic field is coupling weakly with the biomolecular vibrational resonances, and that the LSPR modulation is induced by the dielectric environment change (i.e., change of bulk refractive index) in the presence of the biomolecules.

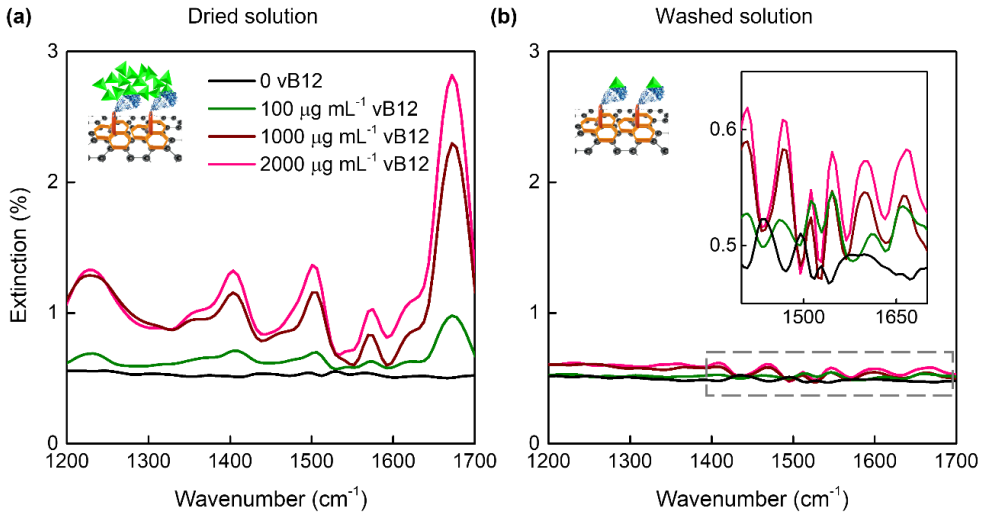

Figure 5.4: Vitamin B12 band characterization. Extinction spectra are shown for different concentrations of (a) dried and (b) washed solutions of vB12 on non-patterned graphene. Inset in (b) displays a zoom-in of vB12 vibrational bands.

In order to elucidate the influence of the biomolecular layers on the conductivity of the graphene, electrical characterizations (R vs. V_{BG}) were performed with a fabricated graphene field effect transistor (gFET)-like device with an active area of 500x500 μm^2, as shown in Fig. 5.5. Prior to the measurements, the gFET sample was treated by, firstly, spin-coating and then removal of the e-beam resist (ZEP) to mimic the initial p-doping of as-prepared GNR via e-beam lithography. The Dirac curve of the gFET has a charge neutrality point (CNP) of around $V_{BG} \sim +40V$, indicating that the Fermi level is in the valence band (p-doped) with hole carriers. The addition of pyrene caused the CNP to move towards a higher p-doping level ($V_{BG} \sim +60V$), probably due to the additional hole doping induced by the NHS ester contained in the pyrene molecules.[151] However, on addition of the Fab and vB12, the Dirac curves showed only small CNP shifts, maintaining the graphene at similar p-doped levels in all cases.

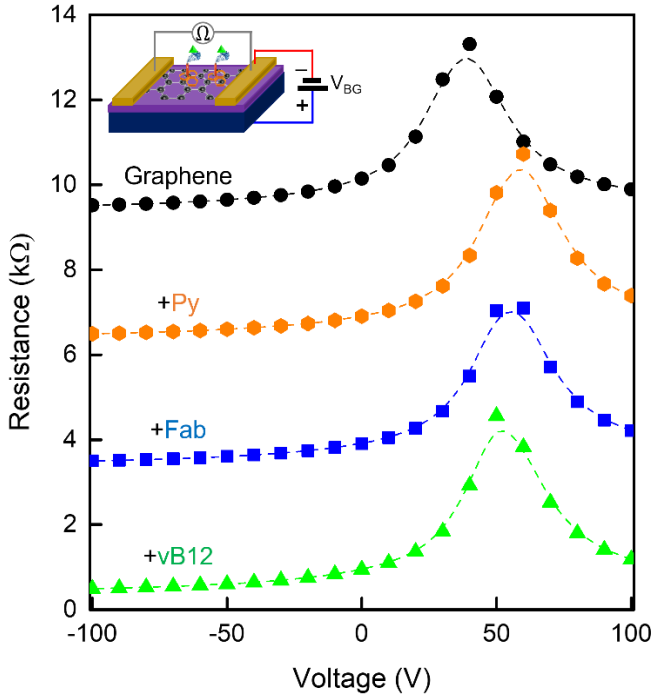

Figure 5.5: Electrical characterization of a bioassay for graphene with a V_{BG} sweep. The inset shows a schematic of the sensor chip, which measures the electrical resistance R across $0.5x0.5\,mm^2$ graphene for a V_{BG} sweep from $+100V$ to $-100V$. The R vs. V_{BG} plots are displayed for graphene only and also for subsequent added layers of Py, Fab and vB12.

Fig. 5.6 illustrates the enhancement of the LSPR modes upon dynamical tuning via electrostatic gating for the cases with GNR only and after the addition of Py, Fab and vB12 biomolecular layers. In all cases, the LSPR modes continuously blue-shift and increase in amplitude by applying back-gate voltages from $0V$ to $-100V$ (i.e., higher p-doping). However, the overall spectral locations of LSPR peaks have red-shift on addition of each biomolecular layer. In the experiments, we kept the system at $V_{BG} = -100V$ (recall Fig. 5.3b) in order to have enhanced LSPR when analyzing the responses for different vB12 concentrations.

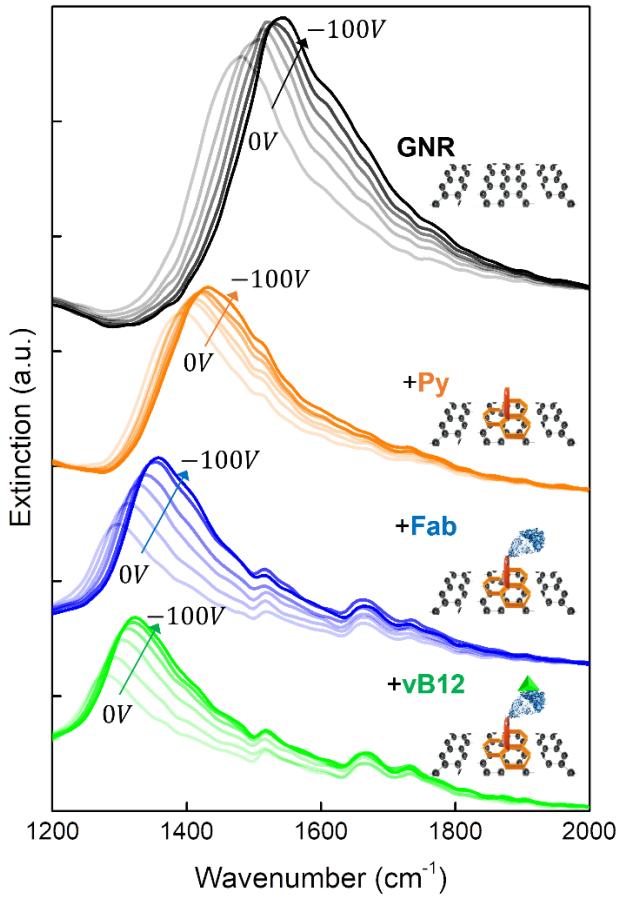

Figure 5.6: Optical characterization of a bioassay for GNR with a V_{BG} sweep. Extinction spectra for bias voltages V_{BG} from $0V$ to $-100V$ (sweep direction indicated by arrows) are presented for GNR alone and for subsequent added layers of Py, Fab and vB12. A vertical offset was applied to show the stack of grouped LSPR responses for each addition of biomolecular layer.

5.3 Quantification of Vitamin B12

This section tackles the quantification of vB12 concentrations from graphene LSPR modulation. Different concentrations of vB12 solutions are spotted on each of the GNR+Py+Fab sensor elements (recall Fig. 1a). After incubation, washing and drying steps of the chip, the optical measurements are taken per sensor element. We examined that the LSPR

further redshifts and reduces in amplitude with increasing vB12 concentration. We acquired the calibration curve for vB12 detection by calculating the spectral shifts. Hence, we extracted the spectral positions of LSPR peaks before (k_1) and after (k_2) adding vB12, as illustrated from the dashed lines in Fig. 5.3b.

The calibration plots of vB12 concentration vs. $\Delta(k_1 - k_2)$ are displayed in Fig. 5.7. In Fig. 5.7a, the current values of the standard curve showed a sigmoidal relationship with the concentration of vB12 with saturation above 5 $\mu g \cdot mL^{-1}$. However, the linear fitting in Fig. 5.7b shows an excellent linearity (R^2 = 0.99, p<0.001). Here, the sensitivity of the system is calculated from the slope of the standard curve, which equals 4.4 $mL \cdot cm^{-1} \cdot mg^{-1}$. The limit of detection (LOD) was found to be 43 nM, calculated as 3 times the standard deviation of the y-intercept of the regression line divided by the slope.

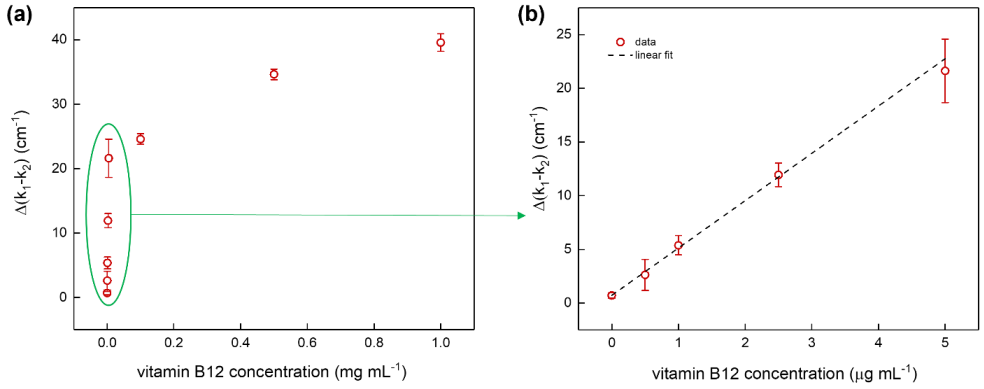

Figure 5.7: Calibration plots for vB12 detection. (a) Standard curve for wavenumber shift $\Delta(k_1 - k_2)$ vs. vB12 concentration (from 0 to 1 $mg\,mL^{-1}$), where k_1 and k_2 indicate the spectral positions of the LSPR peaks before and after the addition of vB12 analytes, respectively. (b) Linear fit for the lower concentration range from 0 to 5 $\mu g\,mL^{-1}$.

A negative control experiment was performed to test the specific binding of vB12 molecules with Fab receptors. In this experiment, we compared

two bioassays, one with complete components (GNR+Py+Fab+vB12, solid line) and the other one without the Fab layer (GNR+Py+vB12, dashed line). As shown in Fig. 5.8, a significant shift is observed with the presence of Fab, indicating the specific binding of vB12 to Fab. On the other hand, almost no spectral shift is observed in the control experiment (without the Fab), signifying the absence of the non-specific binding of vB12 to the surface of the GNR.

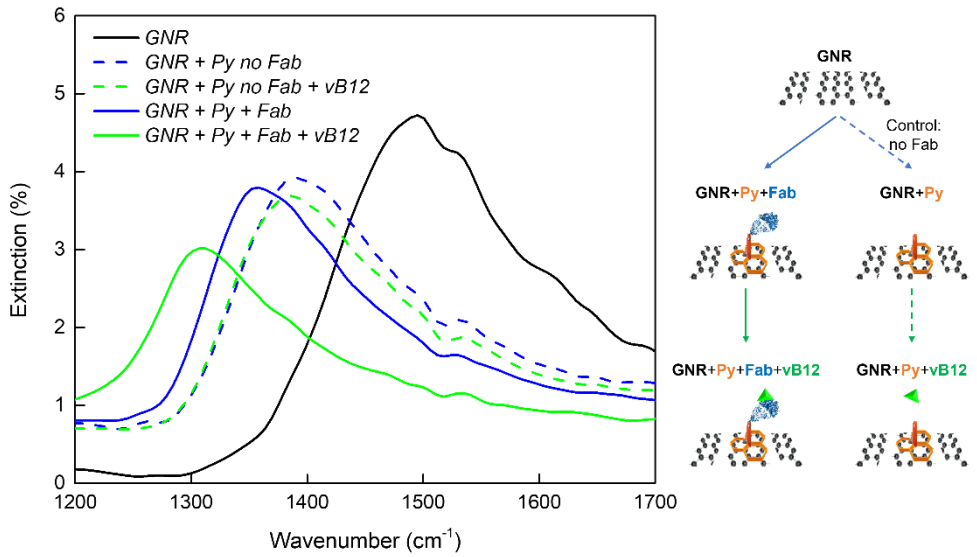

Figure 5.8: Control experiment for the non-specific binding of vB12 to the surface of the GNR sensor. Extinction spectra are displayed for vB12 binding to the surface with Fab (solid curves) and without Fab (dashed curves). The right panel shows an illustration of sequential bioassay formation between the actual sensing experiment and control experiment.

5.4 Biosensing with Large-Scale Graphene Nanoholes

In order to move toward large sample sizes and the effective screening analysis of mid-IR sensing applications with nanostructured graphene surfaces, an important factor to consider is the employment of cost-

effective and high throughput processes as an alternative to e-beam lithography (EBL). For instance, nanoimprint lithography (NIL)[59] and block copolymer self-assembly strategy[152] have shown great potential for future implementations, and are constantly being improved in terms of high uniformity and minimal fabrication defects of scalable graphene nanostructures. This section presents a demonstration of the same biosensing experiment with a large-scale NIL-fabricated GNH sample, fabricated and provided by the collaborators from *The Institute of Materials Science of Barcelona* (*ICMAB)*.

Fig. 5.9 illustrates a schematic of the GNH-based biosensor setup. The SEM micrograph shows the fabricated GNH structures, which exhibit an LSPR that is polarization-insensitive to IR transmission.[59] Therefore, in this experiment, we used unpolarized IR light and a $1x1\ mm^2$ aperture size (100x larger that that used for the EBL-fabricated GNR in Fig. 5.1), which allows a response from a wide area of the GNH surface to be collected. The sensor chip consisting of large-scale GNH on an SiO_2/Si substrate is also configured with electrostatic back-gate voltage V_{BG} for optical tuning.

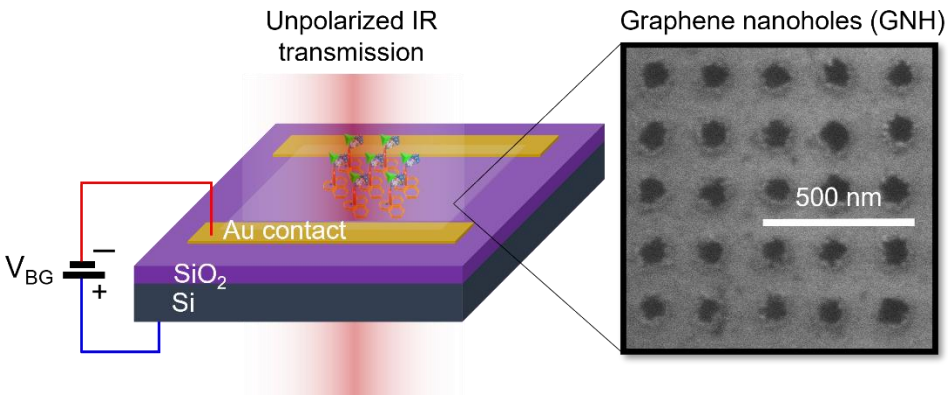

Figure 5.9: Schematic diagram of a sensor based on large-scale patterned graphene nanoholes (GNH) via nanoimprint lithography on an SiO_2/Si substrate, which is configured with a supply of back-gate voltage V_{BG}. The SEM micrograph shows the GNH of diameter d=75nm and period p=200nm.

Fig. 5.10a depicts the LSPR response of an NIL-fabricated GNH sample with dynamical tuning via electrostatic gating. The LSPR modes are enhanced by applying the V_{BG} toward higher negative voltages (i.e., higher p doping), specifically blue-shifting and increasing the intensity of the LSPR peaks. The overall response of the GNH with an immobilized bioassay in Fig. 5.9b shows a red-shift and decreased amplitude of the LSPR peaks, which is similar to the result-trend of the GNR case in Fig. 5.6.

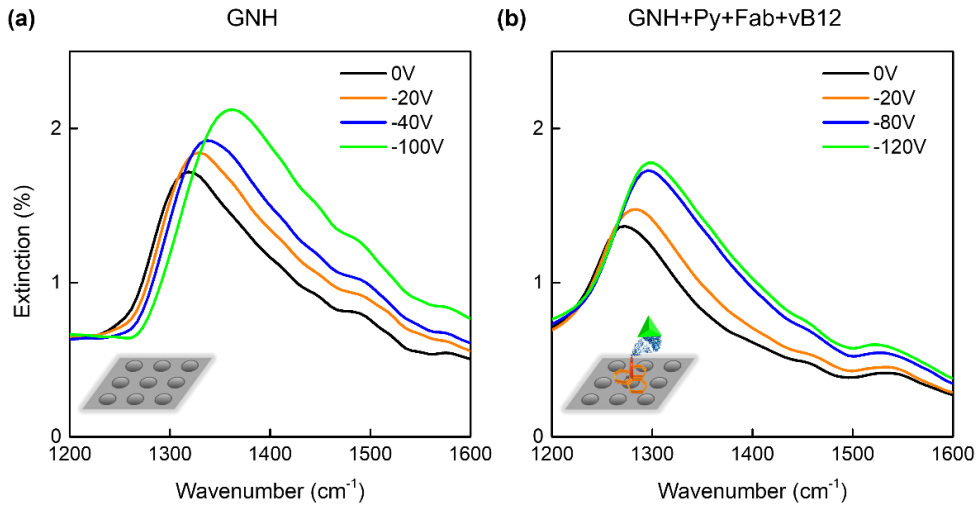

Figure 5.10: GNH surface characterization. Extinction spectra of (a) as-prepared GNH and (b) GNH after bioassay formation are displayed for a V_{BG} sweep from $0V$ to higher negative voltages.

Fig. 5.11 displays the experimental extinction spectra obtained by analyzing the GNH after the addition of each biomolecular layer and at different vB12 concentrations. We have observed results that are consistent with the same experiments carried out using small-scale GNR structures, where the LSPR peak continuously reduces in amplitude and redshifts (Fig. 5.11a). In Fig. 5.11b, we have also observed the same result-trend for increasing vB12 concentrations with the LSPR peaks further

reduced in intensity and red-shifted. This demonstrates the potential use of NIL-fabricated graphene samples for large-scale biosensing applications. However, the plasmonic mode distributions between GNR and GNH are different, where near field are highly concentrated along the edges of the nanostructures.[54,59] These geometrical shapes may slightly affect the macroscopic sensor responses. Hence, a comparative study between GNR and GNH would be required, with more comprehensive experiments backed by numerical simulations, which goes beyond the scope of our proof-of-concept study.

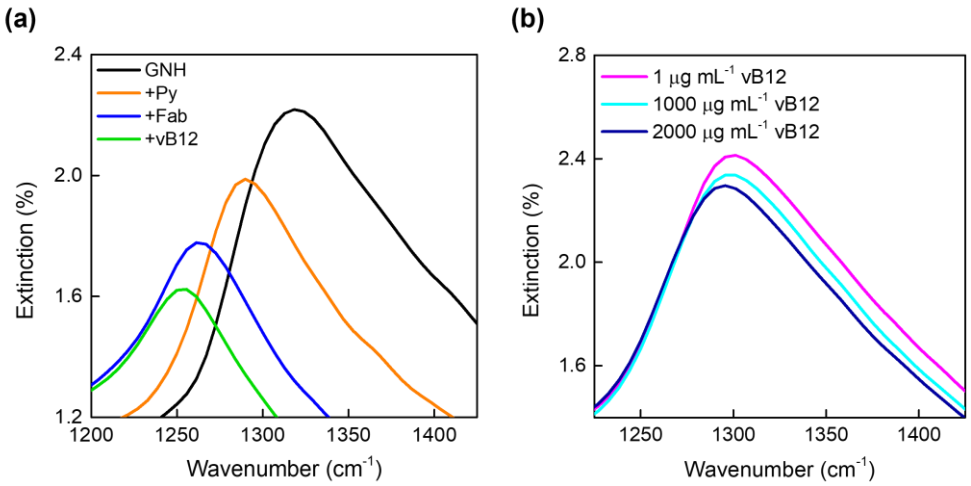

Figure 5.11: Bioassay characterization of large-scale nano-imprinted GNH. (a) Extinction spectra of an ungated chip for successive added biomolecular layers. (b) Extinction spectra for different vB12 concentrations with $V_{BG} = -120V$.

5.5 Conclusion

In this chapter, we have demonstrated a quantitative bioassay for vB12 detection based on mid-IR plasmons of graphene nanostructures. In our system, we functionalized the graphene nanostructures with Py+Fab as a receptor to bind with vB12 target at different concentrations. We found that the LSPR is frequency-shifted and weakened with increasing vB12 concentrations due to changes in the dielectric environment induced by the presence of biomolecules. Using an EBL-fabricated GNR sample, we acquired standard curves based on extracted spectral shifts before and after the addition of the vB12. Remarkably, consistent result-trends were obtained using industrially scalable large-area nanoimprinted graphene nanostructures with the same bioassay. Our results confirm that mid-IR graphene plasmons can be employed for quantitative mid-IR biosensing. The proposed sensor platform could be easily multiplexed for the detection of multiple biomarkers for effective screening and large sample analysis. Additionally, by exploring other hybridized graphene metasurfaces that possess higher LSPR sensitivities, the LOD could be lowered even further for specific applications.[146–148]

Chapter 6

Summary and Outlook

Mid-infrared (mid-IR) spectroscopic sensing, within the 2-20 μm wavelengths as the so-called molecular-fingerprint region, is a powerful technique that finds real applications in chemical analysis, atmospheric surveys, and health diagnostics. In the past decade, spurring scientific research has achieved chip-based developments by employing surface enhanced IR absorption (SEIRA) technologies, but still faces challenges in terms of exploring suitable SEIRA materials and optimizing metasurface designs. The aim of this dissertation is to demonstrate novel mid-IR molecular sensing applications (e.g., relevant for industrial processes and biomarker detections) based on nanostructured two-dimensional van der Waals (2D-vdW) materials, exhibiting highly confined polaritonic modes, and functionalized with relevant layers. Exploiting the 2D-vdW crystals that have been extensively studied in recent years, we investigated the sensing performances of their nanostructures, specifically graphene (pioneering 2D-vdW with tunable electro-optical properties) and hexagonal boron nitride (*hBN*, sustaining ultralow-loss polaritons).

In this thesis, three major mid-IR sensing works have been conceptualized, performed, and evaluated using the nanostructures of graphene and hBN materials.

- First, we demonstrated a novel mid-IR gas sensing platform based on graphene nanoribbons (GNR) functionalized with an ultrathin CO_2-adsorbing polyethylenimine (PEI) layer. The CO_2 level variations were transduced by two coexisting mechanisms: (i) the SEIRA effect (vibrational signal enhancements) and (ii) reversible PEI-induced

graphene doping (localized surface plasmon resonance *LSPR* modulations). We reported the latter as a novel way of efficiently sensing CO_2 levels with a limit of detection of 390 ppm – the ambient atmospheric level – but it was limited because the setup was not hermetically sealed.

- Next, we reported the first phonon-enhanced mid-IR gas sensing system based on monoisotopic hBN nanoresonators functionalized with a thin PEI layer. We detected CO_2 levels by means of the reversible phonon polariton (PhP) resonance tuning caused by dielectric changes in a PEI environment upon the adsorption or thermal desorption of CO_2 gas. Despite a small sensing area of only 30x30 μm^2, we achieved a high signal-to-noise ratio due to high-Q PhP resonances of the hBN nanostructures.
- Finally, we presented a successful quantitative bioassay of vitamin B12 (vB12) detection using mid-IR plasmons of graphene nanostructures with functionalized bioreceptor layers (pyrene linker + anti-vB12 antibody fragment). Varying vB12 concentrations were transduced by the LSPR modulation of EBL-fabricated GNR samples, with the response being influenced by the local bulk refractive index change related to the amount of immobilized vB12 molecules. We acquired a calibration plot based on the spectral shifts of the LSPR upon addition of the vB12, where we extracted an LOD of 43 nM. We also validated the same trend of optical responses with the same bioassay on a large-scale nanoimprinted graphene nanohole array sample.

The main findings in this dissertation confirm that nanostructured 2D-vdW materials such as graphene and hBN could pave the way toward enhanced, molecular-specific, quantitative sensing in the mid-IR. However, further experimental work, backed with numerical simulations, is needed in order for comprehensive performance evaluations to realize their full potentials in molecular sensing applications. On the one hand, the demonstrated proof-of-concept gas sensing (Chapters 3 and 4) could be readily extended to the detection of other relevant gas species with

the same PEI polymer (e.g., NH_3 and volatile organic compounds)[136], or other conductive polymers[153]. On the other hand, the mid-IR biosensor platform could test different sets of small conjugate pairs of immunoassays[135], with the opportunity for multiplexed detection of several biomarkers on a single chip.

Future implementations include scalable sensor platforms and improved sensitivity with the use of optimized surfaces in order to lead 2D-vdW-based mid-IR sensors toward technological maturity. Cost-effective and high throughput processes have already been fabricated with nanostructured graphene using nanoimprint lithography (NIL)[59] and block copolymer self-assembly strategy[152]. As noted previously in Chapter 5, we demonstrated mid-IR biosensing with vB12 detection on an NIL-fabricated GNH surface. While large monolayer graphene grown via chemical vapor deposition (CVD) was used for gas- and biosensing, a monoisotopic hBN flake was also employed for gas sensing having small footprint size for areal measurement. It would be noteworthy to explore and evaluate the mid-IR sensing performance of recently synthesized wafer-scale hBN down to a monolayer via CVD[154] and molecular beam epitaxy (MBE)[155]. In order to improve the sensitivity, as well as reducing fabrication-defects, hybridized 2D-vdW metasurfaces[146–148] or higher crystallinity could be utilized (e.g., seeded growth for monocrystalline graphene[156] or isotopic enrichment[41] for the case of hBN). These possess robust and higher extinction resonances, lowering the LOD of target molecules for specific applications.

Bibliography

(1) Lahiri, B. B.; Bagavathiappan, S.; Jayakumar, T.; Philip, J. Medical Applications of Infrared Thermography: A Review. *Infrared Physics & Technology* 2012, *55* (4), 221–235. https://doi.org/10.1016/j.infrared.2012.03.007.

(2) Hildebrandt, C.; Raschner, C.; Ammer, K. An Overview of Recent Application of Medical Infrared Thermography in Sports Medicine in Austria. *Sensors* 2010, *10* (5), 4700–4715. https://doi.org/10.3390/s100504700.

(3) Seddon, A. B. Mid-Infrared (IR) - A Hot Topic: The Potential for Using Mid-IR Light for Non-Invasive Early Detection of Skin Cancer *in Vivo*. *physica status solidi (b)* 2013, *250* (5), 1020–1027. https://doi.org/10.1002/pssb.201248524.

(4) Ishihara, D.; Onaka, T.; Kataza, H.; Salama, A.; Alfageme, C.; Cassatella, A.; Cox, N.; García-Lario, P.; Stephenson, C.; Cohen, M.; Fujishiro, N.; Fujiwara, H.; Hasegawa, S.; Ita, Y.; Kim, W.; Matsuhara, H.; Murakami, H.; Müller, T. G.; Nakagawa, T.; Ohyama, Y.; Oyabu, S.; Pyo, J.; Sakon, I.; Shibai, H.; Takita, S.; Tanabé, T.; Uemizu, K.; Ueno, M.; Usui, F.; Wada, T.; Watarai, H.; Yamamura, I.; Yamauchi, C. The AKARI/IRC Mid-Infrared All-Sky Survey. *Astronomy and Astrophysics* 2010, *514*, A1. https://doi.org/10.1051/0004-6361/200913811.

(5) Herter, T. L.; Adams, J. D.; de Buizer, J. M.; Gull, G. E.; Schoenwald, J.; Henderson, C. P.; Keller, L. D.; Nikola, T.; Stacey, G.; Vacca, W. D. FIRST SCIENCE OBSERVATIONS WITH SOFIA/FORCAST: THE FORCAST MID-INFRARED CAMERA. *The Astrophysical Journal* 2012, *749* (2), L18. https://doi.org/10.1088/2041-8205/749/2/L18.

(6) Shimoni, M.; Haelterman, R.; Perneel, C. Hypersectral Imaging for Military and Security Applications: Combining Myriad Processing and Sensing Techniques. *IEEE Geoscience and Remote Sensing Magazine* 2019, *7* (2), 101–117. https://doi.org/10.1109/MGRS.2019.2902525.

(7) Andraši, P.; Radišić, T.; Muštra, M.; Ivošević, J. Night-Time Detection of UAVs Using Thermal Infrared Camera. *Transportation Research Procedia* 2017, *28*, 183–190. https://doi.org/10.1016/j.trpro.2017.12.184.

(8) Wang, H.; Chen, J.; Lu, K. Development of a Portable Cavity-Enhanced Absorption Spectrometer for the Measurement of Ambient NO3 and N2O5: Experimental Setup, Lab Characterizations, and Field Applications in a Polluted Urban Environment. *Atmospheric Measurement Techniques* 2017. https://doi.org/10.5194/amt-10-1465-2017.

(9) Kwon, J.; Ahn, G.; Kim, G.; Kim, J. C.; Kim, H. A Study on NDIR-Based CO2 Sensor to Apply Remote Air Quality Monitoring System. In *ICCAS-SICE 2009 - ICROS-SICE International Joint Conference 2009, Proceedings*; 2009.

(10) Neubrech, F.; Huck, C.; Weber, K.; Pucci, A.; Giessen, H. Surface-Enhanced Infrared Spectroscopy Using Resonant Nanoantennas. *Chemical Reviews*. 2017. https://doi.org/10.1021/acs.chemrev.6b00743.

(11) Du, Z.; Zhang, S.; Li, J.; Gao, N.; Tong, K. Mid-Infrared Tunable Laser-Based Broadband Fingerprint Absorption Spectroscopy for Trace Gas Sensing: A Review. *Applied Sciences* 2019, *9* (2), 338. https://doi.org/10.3390/app9020338.

(12) Haas, J.; Mizaikoff, B. Advances in Mid-Infrared Spectroscopy for Chemical Analysis. *Annual Review of Analytical Chemistry* 2016, *9* (1), 45–68. https://doi.org/10.1146/annurev-anchem-071015-041507.

(13) Diem, M.; Romeo, M.; Boydston-White, S.; Miljković, M.; Matthäus, C. A Decade of Vibrational Micro-Spectroscopy of Human Cells and Tissue (1994–2004). *Analyst* 2004, *129* (10), 880–885. https://doi.org/10.1039/B408952A.

(14) Selvaraj, R.; Vasa, N. J.; Nagendra, S. M. S.; Mizaikoff, B. Advances in Mid-Infrared Spectroscopy-Based Sensing Techniques for Exhaled Breath Diagnostics. *Molecules* 2020, *25* (9), 2227. https://doi.org/10.3390/molecules25092227.

(15) Coleman, P. B. *Practical Sampling Techniques for Infrared Analysis*; CRC Press, 1993.

(16) Khoshhesab, Z. M. Reflectance IR Spectroscopy. *Infrared spectroscopy—materials science, engineering and technology* 2012, *11*, 233–244.

(17) Wong, J. Y. NDIR Gas Sensor. US5747808A, 1998.

(18) Brown, S. S.; Stark, H.; Ravishankara, A. R. Cavity Ring-down Spectroscopy for Atmospheric Trace Gas Detection: Application to the Nitrate Radical (NO3). *Applied Physics B: Lasers and Optics* 2002. https://doi.org/10.1007/s00340-002-0980-y.

(19) Patimisco, P.; Scamarcio, G.; Tittel, F. K.; Spagnolo, V. Quartz-Enhanced Photoacoustic Spectroscopy: A Review. *Sensors (Switzerland)* 2014, *14* (4), 6165–6206. https://doi.org/10.3390/s140406165.

(20) Adato, R.; Aksu, S.; Altug, H. Engineering Mid-Infrared Nanoantennas for Surface Enhanced Infrared Absorption Spectroscopy. *Materials Today* 2015, *18* (8), 436–446. https://doi.org/10.1016/j.mattod.2015.03.001.

(21) Cottat, M.; Thioune, N.; Gabudean, A.-M.; Lidgi-Guigui, N.; Focsan, M.; Astilean, S.; Lamy de la Chapelle, M. Localized Surface Plasmon Resonance (LSPR) Biosensor for the Protein Detection. *Plasmonics* 2013, *8* (2), 699–704. https://doi.org/10.1007/s11468-012-9460-3.

(22) Fujiwara, K.; Watarai, H.; Itoh, H.; Nakahama, E.; Ogawa, N. Measurement of Antibody Binding to Protein Immobilized on Gold Nanoparticles by Localized Surface Plasmon Spectroscopy. *Analytical and Bioanalytical Chemistry* 2006, *386* (3), 639–644. https://doi.org/10.1007/s00216-006-0559-2.

(23) Petryayeva, E.; Krull, U. J. Localized Surface Plasmon Resonance: Nanostructures, Bioassays and Biosensing—A Review. *Analytica Chimica Acta* 2011, *706* (1), 8–24. https://doi.org/10.1016/j.aca.2011.08.020.

(24) Ataka, K.; Stripp, S. T.; Heberle, J. Surface-Enhanced Infrared Absorption Spectroscopy (SEIRAS) to Probe Monolayers of Membrane Proteins. *Biochimica et Biophysica Acta (BBA) - Biomembranes* 2013, *1828* (10), 2283–2293. https://doi.org/10.1016/j.bbamem.2013.04.026.

(25) Osawa, M.; Ataka, K.-I.; Yoshii, K.; Nishikawa, Y. Surface-Enhanced Infrared Spectroscopy: The Origin of the Absorption Enhancement and Band Selection Rule in the Infrared Spectra of Molecules Adsorbed on Fine Metal Particles. *Applied Spectroscopy* 1993, *47* (9), 1497–1502.

(26) Lilley, G.; Messner, M.; Unterrainer, K. Improving the Quality Factor of the Localized Surface Plasmon Resonance. *Optical Materials Express* 2015, *5* (10). https://doi.org/10.1364/ome.5.002112.

(27) Brown, L. v.; Yang, X.; Zhao, K.; Zheng, B. Y.; Nordlander, P.; Halas, N. J. Fan-Shaped Gold Nanoantennas above Reflective Substrates for Surface-Enhanced Infrared Absorption (SEIRA). *Nano Letters* 2015, *15* (2), 1272–1280. https://doi.org/10.1021/nl504455s.

(28) Liu, N.; Mesch, M.; Weiss, T.; Hentschel, M.; Giessen, H. Infrared Perfect Absorber and Its Application As Plasmonic Sensor. *Nano Letters* 2010, *10* (7), 2342–2348. https://doi.org/10.1021/nl9041033.

(29) Hasan, D.; Lee, C. Hybrid Metamaterial Absorber Platform for Sensing of CO2 Gas at Mid-IR. *Advanced Science* 2018, *5* (5). https://doi.org/10.1002/advs.201700581.

(30) Geim, A. K.; Grigorieva, I. v. Van Der Waals Heterostructures. *Nature* 2013, *499* (7459), 419–425. https://doi.org/10.1038/nature12385.

(31) Novoselov, K. S.; Mishchenko, A.; Carvalho, A.; Castro Neto, A. H. 2D Materials and van Der Waals Heterostructures. *Science (1979)* 2016, *353* (6298). https://doi.org/10.1126/science.aac9439.

(32) Ajayan, P.; Kim, P.; Banerjee, K. Two-Dimensional van Der Waals Materials. *Physics Today* 2016, *69* (9), 38–44. https://doi.org/10.1063/PT.3.3297.

(33) Liu, Y.; Weiss, N. O.; Duan, X.; Cheng, H.-C.; Huang, Y.; Duan, X. Van Der Waals Heterostructures and Devices. *Nature Reviews Materials* 2016, *1* (9), 16042. https://doi.org/10.1038/natrevmats.2016.42.

(34) Shiue, R.-J.; Efetov, D. K.; Grosso, G.; Peng, C.; Fong, K. C.; Englund, D. Active 2D Materials for On-Chip Nanophotonics and Quantum Optics. *Nanophotonics* 2017, *6* (6), 1329–1342. https://doi.org/10.1515/nanoph-2016-0172.

(35) Basov, D. N.; Fogler, M. M.; García De Abajo, F. J. Polaritons in van Der Waals Materials. *Science*. 2016. https://doi.org/10.1126/science.aag1992.

(36) Ma, W.; Shabbir, B.; Ou, Q.; Dong, Y.; Chen, H.; Li, P.; Zhang, X.; Lu, Y.; Bao, Q. Anisotropic Polaritons in van Der Waals Materials. *InfoMat* 2020, *2* (5), 777–790. https://doi.org/10.1002/inf2.12119.

(37) Grigorenko, A. N.; Polini, M.; Novoselov, K. S. Graphene Plasmonics. *Nature Photonics* 2012, *6* (11). https://doi.org/10.1038/nphoton.2012.262.

(38) García de Abajo, F. J. Graphene Plasmonics: Challenges and Opportunities. *ACS Photonics* 2014, *1* (3). https://doi.org/10.1021/ph400147y.

(39) Koppens, F. H. L.; Chang, D. E.; García de Abajo, F. J. Graphene Plasmonics: A Platform for Strong Light–Matter Interactions. *Nano Letters* 2011, *11* (8), 3370–3377. https://doi.org/10.1021/nl201771h.

(40) Fan, Y.; Shen, N.; Zhang, F.; Zhao, Q.; Wu, H.; Fu, Q.; Wei, Z.; Li, H.; Soukoulis, C. M. Graphene Plasmonics: A Platform for 2D Optics. *Advanced Optical Materials* 2019, *7* (3), 1800537. https://doi.org/10.1002/adom.201800537.

(41) Giles, A. J.; Dai, S.; Vurgaftman, I.; Hoffman, T.; Liu, S.; Lindsay, L.; Ellis, C. T.; Assefa, N.; Chatzakis, I.; Reinecke, T. L.; Tischler, J. G.; Fogler, M. M.; Edgar, J. H.; Basov, D. N.; Caldwell, J. D. Ultralow-Loss Polaritons in Isotopically Pure Boron Nitride. *Nature Materials* 2018, *17* (2). https://doi.org/10.1038/NMAT5047.

(42) Autore, M.; Dolado, I.; Li, P.; Esteban, R.; Alfaro-Mozaz, F. J.; Atxabal, A.; Liu, S.; Edgar, J. H.; Vélez, S.; Casanova, F.; Hueso, L. E.; Aizpurua, J.; Hillenbrand, R. Enhanced Light–Matter Interaction in 10B Monoisotopic Boron Nitride Infrared Nanoresonators. *Advanced Optical Materials* 2021, *9* (5). https://doi.org/10.1002/adom.202001958.

(43) Caldwell, J. D.; Kretinin, A. v.; Chen, Y.; Giannini, V.; Fogler, M. M.; Francescato, Y.; Ellis, C. T.; Tischler, J. G.; Woods, C. R.; Giles, A. J.; Hong, M.; Watanabe, K.; Taniguchi, T.; Maier, S. A.; Novoselov, K. S. Sub-Diffractional Volume-Confined Polaritons in the Natural Hyperbolic Material Hexagonal Boron Nitride. *Nature Communications* 2014, *5*. https://doi.org/10.1038/ncomms6221.

(44) Shi, H.; Yan, R.; Bertolazzi, S.; Brivio, J.; Gao, B.; Kis, A.; Jena, D.; Xing, H. G.; Huang, L. Exciton Dynamics in Suspended Monolayer and Few-Layer MoS_2 2D Crystals. *ACS Nano* 2013, *7* (2), 1072–1080. https://doi.org/10.1021/nn303973r.

(45) Hill, H. M.; Rigosi, A. F.; Roquelet, C.; Chernikov, A.; Berkelbach, T. C.; Reichman, D. R.; Hybertsen, M. S.; Brus, L. E.; Heinz, T. F. Observation of Excitonic Rydberg States in Monolayer MoS_2 and WS_2 by Photoluminescence Excitation Spectroscopy. *Nano Letters* 2015, *15* (5), 2992–2997. https://doi.org/10.1021/nl504868p.

(46) Liu, Y.; Huang, Y.; Duan, X. Van Der Waals Integration before and beyond Two-Dimensional Materials. *Nature* 2019, *567* (7748), 323–333. https://doi.org/10.1038/s41586-019-1013-x.

(47) Liu, C.; Zheng, J.; Chen, Y.; Fryett, T.; Majumdar, A. Van Der Waals Materials Integrated Nanophotonic Devices [Invited]. *Optical Materials Express* 2019, *9* (2), 384. https://doi.org/10.1364/OME.9.000384.

(48) Ling, H.; Li, R.; Davoyan, A. R. All van Der Waals Integrated Nanophotonics with Bulk Transition Metal Dichalcogenides. *ACS Photonics* 2021, *8* (3), 721–730. https://doi.org/10.1021/acsphotonics.0c01964.

(49) Novoselov, K. S.; Geim, A. K.; Morozov, S. v.; Jiang, D.; Zhang, Y.; Dubonos, S. v.; Grigorieva, I. v.; Firsov, A. A. Electric Field Effect in Atomically Thin Carbon Films. *Science (1979)* 2004, *306* (5696), 666–669. https://doi.org/10.1126/science.1102896.

(50) Novoselov, K. S.; Geim, A. K.; Morozov, S. v.; Jiang, D.; Katsnelson, M. I.; Grigorieva, I. v.; Dubonos, S. v.; Firsov, A. A. Two-Dimensional Gas of Massless Dirac Fermions in Graphene. *Nature* 2005, *438* (7065), 197–200. https://doi.org/10.1038/nature04233.

(51) Mas-Ballesté, R.; Gómez-Navarro, C.; Gómez-Herrero, J.; Zamora, F. 2D Materials: To Graphene and Beyond. *Nanoscale* 2011, *3* (1), 20–30. https://doi.org/10.1039/C0NR00323A.

(52) Caldwell, J. D.; Aharonovich, I.; Cassabois, G.; Edgar, J. H.; Gil, B.; Basov, D. N. Photonics with Hexagonal Boron Nitride. *Nature Reviews Materials* 2019, *4* (8), 552–567. https://doi.org/10.1038/s41578-019-0124-1.

(53) Zheng, B.; Yang, X.; Li, J.; Shi, C.-F.; Wang, Z.-L.; Xia, X.-H. Graphene Plasmon-Enhanced IR Biosensing for in Situ Detection of Aqueous-Phase Molecules with an Attenuated Total Reflection Mode. *Analytical Chemistry* 2018, *90* (18), 10786–10794. https://doi.org/10.1021/acs.analchem.8b01715.

(54) Rodrigo, D.; Limaj, O.; Janner, D.; Etezadi, D.; García De Abajo, F. J.; Pruneri, V.; Altug, H. Mid-Infrared Plasmonic Biosensing with Graphene. *Science (1979)* 2015, *349* (6244), 165–168. https://doi.org/10.1126/science.aab2051.

(55) Powell, A. W.; Coles, D. M.; Taylor, R. A.; Watt, A. A. R.; Assender, H. E.; Smith, J. M. Plasmonic Gas Sensing Using Nanocube Patch Antennas. *Advanced Optical Materials* 2016, *4* (4). https://doi.org/10.1002/adom.201500602.

(56) Bingham, J. M.; Anker, J. N.; Kreno, L. E.; van Duyne, R. P. Gas Sensing with High-Resolution Localized Surface Plasmon Resonance Spectroscopy. *J Am Chem Soc* 2010, *132* (49). https://doi.org/10.1021/ja1074272.

(57) Su, D.-S.; Tsai, D. P.; Yen, T.-J.; Tanaka, T. Ultrasensitive and Selective Gas Sensor Based on a Channel Plasmonic Structure with an Enormous Hot Spot Region. *ACS Sensors* 2019, *4* (11). https://doi.org/10.1021/acssensors.9b01225.

(58) Allsop, T.; Arif, R.; Neal, R.; Kalli, K.; Kundrát, V.; Rozhin, A.; Culverhouse, P.; Webb, D. J. Photonic Gas Sensors Exploiting Directly the Optical Properties of Hybrid Carbon Nanotube Localized Surface Plasmon Structures. *Light: Science & Applications* 2016, *5* (2). https://doi.org/10.1038/lsa.2016.36.

(59) Gopalan, K. K.; Paulillo, B.; Mackenzie, D. M. A.; Rodrigo, D.; Bareza, N.; Whelan, P. R.; Shivayogimath, A.; Pruneri, V. Scalable and Tunable Periodic Graphene Nanohole Arrays for Mid-Infrared Plasmonics. *Nano Letters* 2018, *18* (9), 5913–5918. https://doi.org/10.1021/acs.nanolett.8b02613.

(60) Ju, L.; Geng, B.; Horng, J.; Girit, C.; Martin, M.; Hao, Z.; Bechtel, H. A.; Liang, X.; Zettl, A.; Shen, Y. R.; Wang, F. Graphene Plasmonics for Tunable Terahertz Metamaterials. *Nature Nanotechnology* 2011. https://doi.org/10.1038/nnano.2011.146.

(61) Paulillo, B.; Bareza, N. J.; Pruneri, V. Controlling Mid-Infrared Plasmons in Graphene Nanostructures through Post-Fabrication Chemical Doping. *JPhys Photonics* 2021, *3* (3). https://doi.org/10.1088/2515-7647/abf943.

(62) Low, T.; Avouris, P. Graphene Plasmonics for Terahertz to Mid-Infrared Applications. *ACS Nano* 2014, *8* (2), 1086–1101. https://doi.org/10.1021/nn406627u.

(63) Brar, V. W.; Jang, M. S.; Sherrott, M.; Lopez, J. J.; Atwater, H. A. Highly Confined Tunable Mid-Infrared Plasmonics in Graphene Nanoresonators. *Nano Letters* 2013, *13* (6), 2541–2547. https://doi.org/10.1021/nl400601c.

(64) Hu, H.; Yang, X.; Guo, X.; Khaliji, K.; Biswas, S. R.; García de Abajo, F. J.; Low, T.; Sun, Z.; Dai, Q. Gas Identification with Graphene Plasmons. *Nature Communications* 2019, *10* (1), 1–7. https://doi.org/10.1038/s41467-019-09008-0.

(65) Drage, T. C.; Smith, K. M.; Arenillas, A.; Snape, C. E. Developing Strategies for the Regeneration of Polyethylenimine Based CO2 Adsorbents. In *Energy Procedia*; 2009. https://doi.org/10.1016/j.egypro.2009.01.116.

(66) Peña-Bahamonde, J.; Nguyen, H. N.; Fanourakis, S. K.; Rodrigues, D. F. Recent Advances in Graphene-Based Biosensor Technology with Applications in Life Sciences. *Journal of Nanobiotechnology* 2018, *16* (1), 75. https://doi.org/10.1186/s12951-018-0400-z.

(67) Wang, Y.; Li, Z.; Wang, J.; Li, J.; Lin, Y. Graphene and Graphene Oxide: Biofunctionalization and Applications in Biotechnology. *Trends in Biotechnology* 2011, *29* (5), 205–212. https://doi.org/10.1016/j.tibtech.2011.01.008.

(68) Björk, J.; Hanke, F.; Palma, C.-A.; Samori, P.; Cecchini, M.; Persson, M. Adsorption of Aromatic and Anti-Aromatic Systems on Graphene through Π−π Stacking. *The Journal of Physical Chemistry Letters* 2010, *1* (23), 3407–3412. https://doi.org/10.1021/jz101360k.

(69) Georgakilas, V.; Tiwari, J. N.; Kemp, K. C.; Perman, J. A.; Bourlinos, A. B.; Kim, K. S.; Zboril, R. Noncovalent Functionalization of Graphene and Graphene Oxide for Energy Materials, Biosensing, Catalytic, and Biomedical Applications. *Chemical Reviews* 2016, *116* (9), 5464–5519. https://doi.org/10.1021/acs.chemrev.5b00620.

(70) Muñoz, R.; Gómez-Aleixandre, C. Review of CVD Synthesis of Graphene. *Chemical Vapor Deposition* 2013, *19* (10-11–12), 297–322. https://doi.org/10.1002/cvde.201300051.

(71) Muratore, C.; Voevodin, A. A.; Glavin, N. R. Physical Vapor Deposition of 2D Van Der Waals Materials: A Review. *Thin Solid Films* 2019, *688*, 137500. https://doi.org/10.1016/j.tsf.2019.137500.

(72) Farmer, D. B.; Avouris, P.; Li, Y.; Heinz, T. F.; Han, S.-J. Ultrasensitive Plasmonic Detection of Molecules with Graphene. *ACS Photonics* 2016, *3* (4). https://doi.org/10.1021/acsphotonics.6b00143.

(73) Li, Y.; Yan, H.; Farmer, D. B.; Meng, X.; Zhu, W.; Osgood, R. M.; Heinz, T. F.; Avouris, P. Graphene Plasmon Enhanced Vibrational Sensing of Surface-Adsorbed Layers. *Nano Letters* 2014, *14* (3), 1573–1577. https://doi.org/10.1021/nl404824w.

(74) Hu, H.; Yang, X.; Zhai, F.; Hu, D.; Liu, R.; Liu, K.; Sun, Z.; Dai, Q. Far-Field Nanoscale Infrared Spectroscopy of Vibrational Fingerprints of Molecules with Graphene Plasmons. *Nature Communications* 2016, *7*, 1–8. https://doi.org/10.1038/ncomms12334.

(75) Autore, M.; Li, P.; Dolado, I.; Alfaro-Mozaz, F. J.; Esteban, R.; Atxabal, A.; Casanova, F.; Hueso, L. E.; Alonso-González, P.; Aizpurua, J.; Nikitin, A. Y.; Vélez, S.; Hillenbrand, R. Boron Nitride Nanoresonators for Phonon-Enhanced Molecular Vibrational Spectroscopy at the Strong Coupling Limit. *Light: Science and Applications* 2018. https://doi.org/10.1038/lsa.2017.172.

(76) das Sarma, S.; Adam, S.; Hwang, E. H.; Rossi, E. Electronic Transport in Two-Dimensional Graphene. *Reviews of Modern Physics* 2011, *83* (2), 407–470. https://doi.org/10.1103/RevModPhys.83.407.

(77) Gonçalves, P. A. D.; Peres, N. M. R. *An Introduction to Graphene Plasmonics*; 2016. https://doi.org/10.1142/9948.

(78) Avouris, P.; Chen, Z.; Perebeinos, V. Carbon-Based Electronics. *Nature Nanotechnology* 2007, *2* (10), 605–615. https://doi.org/10.1038/nnano.2007.300.

(79) Liu, H.; Liu, Y.; Zhu, D. Chemical Doping of Graphene. *Journal of Materials Chemistry* 2011. https://doi.org/10.1039/c0jm02922j.

(80) Falkovsky, L. A.; Varlamov, A. A. Space-Time Dispersion of Graphene Conductivity. *The European Physical Journal B* 2007, *56* (4), 281–284. https://doi.org/10.1140/epjb/e2007-00142-3.

(81) Falkovsky, L. A. Optical Properties of Graphene. *Journal of Physics: Conference Series* 2008, *129*. https://doi.org/10.1088/1742-6596/129/1/012004.

(82) Chen, J.; Badioli, M.; Alonso-González, P.; Thongrattanasiri, S.; Huth, F.; Osmond, J.; Spasenović, M.; Centeno, A.; Pesquera, A.; Godignon, P.; Zurutuza Elorza, A.; Camara, N.; de Abajo, F. J. G.; Hillenbrand, R.; Koppens, F. H. L. Optical Nano-Imaging of Gate-Tunable Graphene Plasmons. *Nature* 2012, *487* (7405), 77–81. https://doi.org/10.1038/nature11254.

(83) Christensen, J.; Manjavacas, A.; Thongrattanasiri, S.; Koppens, F. H. L.; García de Abajo, F. J. Graphene Plasmon Waveguiding and Hybridization in Individual and Paired Nanoribbons. *ACS Nano* 2012, *6* (1), 431–440. https://doi.org/10.1021/nn2037626.

(84) Wang, F.; Zhang, Y.; Tian, C.; Girit, C.; Zettl, A.; Crommie, M.; Shen, Y. R. Gate-Variable Optical Transitions in Graphene. *Science (1979)* 2008. https://doi.org/10.1126/science.1152793.

(85) Yan, H.; Low, T.; Zhu, W.; Wu, Y.; Freitag, M.; Li, X.; Guinea, F.; Avouris, P.; Xia, F. Damping Pathways of Mid-Infrared Plasmons in Graphene Nanostructures. *Nature Photonics* 2013, *7* (5), 394–399. https://doi.org/10.1038/nphoton.2013.57.

(86) Roy, S.; Zhang, X.; Puthirath, A. B.; Meiyazhagan, A.; Bhattacharyya, S.; Rahman, M. M.; Babu, G.; Susarla, S.; Saju, S. K.; Tran, M. K.; Sassi, L. M.; Saadi, M. A. S. R.; Lai, J.; Sahin, O.; Sajadi, S. M.; Dharmarajan, B.; Salpekar, D.; Chakingal, N.; Baburaj, A.; Shuai, X.; Adumbumkulath, A.; Miller, K. A.; Gayle, J. M.; Ajnsztajn, A.; Prasankumar, T.; Harikrishnan, V. V. J.; Ojha, V.; Kannan, H.; Khater, A. Z.; Zhu, Z.; Iyengar, S. A.; Autreto, P. A. da S.; Oliveira, E. F.; Gao, G.; Birdwell, A. G.; Neupane, M. R.; Ivanov, T. G.; Taha-Tijerina, J.; Yadav, R. M.; Arepalli, S.; Vajtai, R.; Ajayan, P. M. Structure, Properties and Applications of Two-Dimensional Hexagonal Boron Nitride. *Advanced Materials* 2021, *33* (44), 2101589. https://doi.org/10.1002/adma.202101589.

(87) Majety, S.; Cao, X. K.; Dahal, R.; Pantha, B. N.; Li, J.; Lin, J. Y.; Jiang, H. X. Semiconducting Hexagonal Boron Nitride for Deep Ultraviolet Photonics; Razeghi, M., Tournie, E., Brown, G. J., Eds.; 2012; p 82682R. https://doi.org/10.1117/12.914084.

(88) Caldwell, J. D.; Kretinin, A. v.; Chen, Y.; Giannini, V.; Fogler, M. M.; Francescato, Y.; Ellis, C. T.; Tischler, J. G.; Woods, C. R.; Giles, A. J.; Hong, M.; Watanabe, K.; Taniguchi, T.; Maier, S. A.; Novoselov, K. S. Sub-Diffractional Volume-Confined Polaritons in the Natural Hyperbolic Material Hexagonal Boron Nitride. *Nature Communications* 2014, *5* (1), 5221. https://doi.org/10.1038/ncomms6221.

(89) Dai, S.; Fei, Z.; Ma, Q.; Rodin, A. S.; Wagner, M.; McLeod, A. S.; Liu, M. K.; Gannett, W.; Regan, W.; Watanabe, K.; Taniguchi, T.; Thiemens, M.; Dominguez, G.; Neto, A. H. C.; Zettl, A.; Keilmann, F.; Jarillo-Herrero, P.; Fogler, M. M.; Basov, D. N. Tunable Phonon Polaritons in Atomically Thin van Der Waals Crystals of Boron Nitride. *Science (1979)* 2014, *343* (6175), 1125–1129. https://doi.org/10.1126/science.1246833.

(90) Dai, S.; Ma, Q.; Andersen, T.; Mcleod, A. S.; Fei, Z.; Liu, M. K.; Wagner, M.; Watanabe, K.; Taniguchi, T.; Thiemens, M.; Keilmann, F.; Jarillo-Herrero, P.; Fogler, M. M.; Basov, D. N. Subdiffractional Focusing and Guiding of Polaritonic Rays in a Natural Hyperbolic Material. *Nature Communications* 2015, *6* (1), 6963. https://doi.org/10.1038/ncomms7963.

(91) Li, P.; Dolado, I.; Alfaro-Mozaz, F. J.; Casanova, F.; Hueso, L. E.; Liu, S.; Edgar, J. H.; Nikitin, A. Y.; Vélez, S.; Hillenbrand, R. Infrared Hyperbolic Metasurface Based on Nanostructured van Der Waals Materials. *Science (1979)* 2018, *359* (6378), 892–896. https://doi.org/10.1126/science.aaq1704.

(92) Fine, G. F.; Cavanagh, L. M.; Afonja, A.; Binions, R. Metal Oxide Semi-Conductor Gas Sensors in Environmental Monitoring. *sensors* 2010, *10* (6), 5469–5502.

(93) A. Kumar, T.M.G. Kingson, R.P. Verma, A. Kumar, R. Mandal, S. Dutta, S. K. C. and G. M. P. Application of Gas Monitoring Sensors in Underground Coal Mines and Hazardous Areas. *International Journal of Computer Technology and Electronics Engineering (IJCTEE)* 2013.

(94) Murvay, P. S.; Silea, I. A Survey on Gas Leak Detection and Localization Techniques. *Journal of Loss Prevention in the Process Industries*. 2012. https://doi.org/10.1016/j.jlp.2012.05.010.

(95) di Natale, C.; Paolesse, R.; Martinelli, E.; Capuano, R. Solid-State Gas Sensors for Breath Analysis: A Review. *Analytica Chimica Acta*. 2014. https://doi.org/10.1016/j.aca.2014.03.014.

(96) Jaaniso, R.; Tan, O. K. *Semiconductor Gas Sensors*; 2013. https://doi.org/10.1533/9780857098665.

(97) Hodgkinson, J.; Tatam, R. P. Optical Gas Sensing: A Review. *Measurement Science and Technology*. 2013. https://doi.org/10.1088/0957-0233/24/1/012004.

(98) Bogue, R. Detecting Gases with Light: A Review of Optical Gas Sensor Technologies. *Sensor Review* 2015. https://doi.org/10.1108/SR-09-2014-696.

(99) Bandara, K. M. T. S.; Sakai, K.; Nakandakari, T.; Yuge, K. A Low-Cost NDIR-Based N2O Gas Detection Device for Agricultural Soils: Assembly, Calibration Model Validation, and Laboratory Testing. *Sensors* 2021, *21* (4), 1189. https://doi.org/10.3390/s21041189.

(100) CO2 and RH/T sensor module - Model SCD30 https://sensirion.com/products/catalog/SCD30/ (accessed 2022 -02 -22).
(101) Gasmet Technologies, Inc. - Model DX4040 Portable FTIR Gas Analyzer https://www.wmddetectorselector.army.mil/detectorPages/193.aspx (accessed 2022 -01 -31).
(102) Commoner, B.; Lipkin, D. The Application of the Beer-Lambert Law to Optically Anisotropic Systems. *Science (1979)* 1949, *110* (2845), 41–43. https://doi.org/10.1126/science.110.2845.41.b.
(103) Courtright, B. A. E.; Jenekhe, S. A. Polyethylenimine Interfacial Layers in Inverted Organic Photovoltaic Devices: Effects of Ethoxylation and Molecular Weight on Efficiency and Temporal Stability. *ACS Applied Materials & Interfaces* 2015, *7* (47), 26167–26175. https://doi.org/10.1021/acsami.5b08147.
(104) Kircheis, R.; Wightman, L.; Schreiber, A.; Robitza, B.; Rössler, V.; Kursa, M.; Wagner, E. Polyethylenimine/DNA Complexes Shielded by Transferrin Target Gene Expression to Tumors after Systemic Application. *Gene Therapy* 2001, *8* (1), 28–40. https://doi.org/10.1038/sj.gt.3301351.
(105) Urban-Klein, B.; Werth, S.; Abuharbeid, S.; Czubayko, F.; Aigner, A. RNAi-Mediated Gene-Targeting through Systemic Application of Polyethylenimine (PEI)-Complexed SiRNA in Vivo. *Gene Therapy* 2005, *12* (5), 461–466. https://doi.org/10.1038/sj.gt.3302425.
(106) Shen, X.; Du, H.; Mullins, R. H.; Kommalapati, R. R. Polyethylenimine Applications in Carbon Dioxide Capture and Separation: From Theoretical Study to Experimental Work. *Energy Technology* 2017, *5* (6), 822–833. https://doi.org/10.1002/ente.201600694.
(107) Chang, Y.; Hasan, D.; Dong, B.; Wei, J.; Ma, Y.; Zhou, G.; Ang, K. W.; Lee, C. All-Dielectric Surface-Enhanced Infrared Absorption-Based Gas Sensor Using Guided Resonance. *ACS Applied Materials and Interfaces* 2018, *10* (44), 38272–38279. https://doi.org/10.1021/acsami.8b16623.
(108) Littel, R. J.; Versteeg, G. F.; van Swaaij, W. P. M. Kinetics of CO2 with Primary and Secondary Amines in Aqueous Solutions-I. Zwitterion Deprotonation Kinetics for DEA and DIPA in Aqueous Blends of Alkanolamines. *Chemical Engineering Science* 1992. https://doi.org/10.1016/0009-2509(92)80319-8.
(109) Bai, H.; Shi, G. Gas Sensors Based on Conducting Polymers. *Sensors* 2007, *7* (3), 267–307. https://doi.org/10.3390/s7030267.
(110) Sharma, P.; Chakrabarty, S.; Roy, S.; Kumar, R. Molecular View of CO2 Capture by Polyethylenimine: Role of Structural and Dynamical Heterogeneity. *Langmuir* 2018, *34* (17). https://doi.org/10.1021/acs.langmuir.8b00204.
(111) Al-Marri, M. J.; Khader, M. M.; Tawfik, M.; Qi, G.; Giannelis, E. P. CO2 Sorption Kinetics of Scaled-up Polyethylenimine-Functionalized Mesoporous Silica Sorbent. *Langmuir* 2015, *31* (12). https://doi.org/10.1021/acs.langmuir.5b00189.
(112) Chowdhury, F. A.; Yamada, H.; Higashii, T.; Goto, K.; Onoda, M. CO2 Capture by Tertiary Amine Absorbents: A Performance Comparison Study. *Industrial and Engineering Chemistry Research* 2013. https://doi.org/10.1021/ie400825u.

(113) Park, H. S.; Jung, Y. M.; You, J. K.; Hong, W. H.; Kim, J. N. Analysis of the CO2 and NH3 Reaction in an Aqueous Solution by 2D IR COS: Formation of Bicarbonate and Carbamate. *Journal of Physical Chemistry A* 2008. https://doi.org/10.1021/jp800991d.

(114) Hiyoshi, N.; Yogo, K.; Yashima, T. Adsorption Characteristics of Carbon Dioxide on Organically Functionalized SBA-15. *Microporous and Mesoporous Materials* 2005. https://doi.org/10.1016/j.micromeso.2005.06.010.

(115) Bacsik, Z.; Zhang, P.; Hedin, N. Ammonium-Carbamate-Rich Organogels for the Preparation of Amorphous Calcium Carbonates. *Minerals* 2017. https://doi.org/10.3390/min7070110.

(116) Furer, V. L. The IR Spectra and Hydrogen Bonding of Toluene-2,6-Bis(Methyl) and 4,4'- Diphenylmethane-Bis(Methyl) Carbamates. *Journal of Molecular Structure* 2000. https://doi.org/10.1016/S0022-2860(99)00321-X.

(117) Wang, X.; Schwartz, V.; Clark, J. C.; Ma, X.; Overbury, S. H.; Xu, X.; Song, C. Infrared Study of CO 2 Sorption over "Molecular Basket" Sorbent Consisting of Polyethylenimine-Modified Mesoporous Molecular Sieve. *Journal of Physical Chemistry C* 2009. https://doi.org/10.1021/jp809946y.

(118) Schedin, F.; Geim, A. K.; Morozov, S. v.; Hill, E. W.; Blake, P.; Katsnelson, M. I.; Novoselov, K. S. Detection of Individual Gas Molecules Adsorbed on Graphene. *Nature Materials* 2007, *6* (9), 652–655. https://doi.org/10.1038/nmat1967.

(119) Al-Mashat, L.; Shin, K.; Kalantar-zadeh, K.; Plessis, J. D.; Han, S. H.; Kojima, R. W.; Kaner, R. B.; Li, D.; Gou, X.; Ippolito, S. J.; Wlodarski, W. Graphene/Polyaniline Nanocomposite for Hydrogen Sensing. *The Journal of Physical Chemistry C* 2010, *114* (39), 16168–16173. https://doi.org/10.1021/jp103134u.

(120) Son, M.; Pak, Y.; Chee, S.-S.; Auxilia, F. M.; Kim, K.; Lee, B.-K.; Lee, S.; Kang, S. K.; Lee, C.; Lee, J. S.; Kim, K. K.; Jang, Y. H.; Lee, B. H.; Jung, G.-Y.; Ham, M.-H. Charge Transfer in Graphene/Polymer Interfaces for CO2 Detection. *Nano Research* 2018, *11* (7), 3529–3536. https://doi.org/10.1007/s12274-017-1857-z.

(121) Cha, M.-J.; Song, W.; Kim, Y.; Jung, D. S.; Jung, M. W.; Lee, S. il; Adhikari, P. D.; An, K.-S.; Park, C.-Y. Long-Term Air-Stable n-Type Doped Graphene by Multiple Lamination with Polyethyleneimine. *RSC Advances* 2014, *4* (71), 37849. https://doi.org/10.1039/C4RA04518A.

(122) Sabri, S. S.; Guillemette, J.; Guermoune, A.; Siaj, M.; Szkopek, T. Enhancing Gas Induced Charge Doping in Graphene Field Effect Transistors by Non-Covalent Functionalization with Polyethyleneimine. *Applied Physics Letters* 2012, *100* (11), 113106. https://doi.org/10.1063/1.3694741.

(123) Jo, I.; Kim, Y.; Moon, J.; Park, S.; Moon, J. S.; Park, W. B.; Lee, J. S.; Hong, B. H. Stable N-Type Doping of Graphene via High-Molecular-Weight Ethylene Amines. *Physical Chemistry Chemical Physics* 2015, *17* (44), 29492–29495. https://doi.org/10.1039/C5CP03196F.

(124) Farmer, D. B.; Roksana, G. M.; Perebeinos, V.; Lin, Y. M.; Tuievski, G. S.; Tsang, J. C.; Avouris, P. Chemical Doping and Electron-Hole Conduction Asymmetry in

Graphene Devices. *Nano Letters* 2009, *9* (1), 388–392. https://doi.org/10.1021/nl803214a.

(125) Chen, C.; Wang, J. Optical Biosensors: An Exhaustive and Comprehensive Review. *Analyst* 2020, *145* (5), 1605–1628. https://doi.org/10.1039/C9AN01998G.

(126) Cooper, M. A. Optical Biosensors in Drug Discovery. *Nature Reviews Drug Discovery* 2002, *1* (7), 515–528. https://doi.org/10.1038/nrd838.

(127) Liedberg, B.; Nylander, C.; Lundström, I. Biosensing with Surface Plasmon Resonance — How It All Started. *Biosensors and Bioelectronics* 1995, *10* (8), i–ix. https://doi.org/10.1016/0956-5663(95)96965-2.

(128) Biacore T200 https://www.cytivalifesciences.com/en/us/shop/protein-analysis/spr-label-free-analysis/systems/biacore-t200-p-05644 (accessed 2022 -01 -30).

(129) Gerion, D.; Storer, R.; Takei, H. Enzymatic Assay for LSPR. USOO8426152B2, April 3, 2013.

(130) John-Herpin, A.; Tittl, A.; Altug, H. Quantifying the Limits of Detection of Surface-Enhanced Infrared Spectroscopy with Grating Order-Coupled Nanogap Antennas. *ACS Photonics* 2018, *5* (10), 4117–4124. https://doi.org/10.1021/acsphotonics.8b00847.

(131) Rodrigo, D.; Tittl, A.; Ait-Bouziad, N.; John-Herpin, A.; Limaj, O.; Kelly, C.; Yoo, D.; Wittenberg, N. J.; Oh, S.-H.; Lashuel, H. A.; Altug, H. Resolving Molecule-Specific Information in Dynamic Lipid Membrane Processes with Multi-Resonant Infrared Metasurfaces. *Nature Communications* 2018, *9* (1), 2160. https://doi.org/10.1038/s41467-018-04594-x.

(132) Syama, S.; Mohanan, P. V. Safety and Biocompatibility of Graphene: A New Generation Nanomaterial for Biomedical Application. *International Journal of Biological Macromolecules* 2016, *86*, 546–555. https://doi.org/10.1016/j.ijbiomac.2016.01.116.

(133) Banerjee, A. N. Graphene and Its Derivatives as Biomedical Materials: Future Prospects and Challenges. *Interface Focus* 2018, *8* (3), 20170056. https://doi.org/10.1098/rsfs.2017.0056.

(134) Seifert, M.; Vargas, J. E. B.; Bobinger, M.; Sachsenhauser, M.; Cummings, A. W.; Roche, S.; Garrido, J. A. Role of Grain Boundaries in Tailoring Electronic Properties of Polycrystalline Graphene by Chemical Functionalization. *2D Materials* 2015, *2* (2), 024008. https://doi.org/10.1088/2053-1583/2/2/024008.

(135) Li, D.; Zhang, W.; Yu, X.; Wang, Z.; Su, Z.; Wei, G. When Biomolecules Meet Graphene: From Molecular Level Interactions to Material Design and Applications. *Nanoscale* 2016, *8* (47), 19491–19509. https://doi.org/10.1039/C6NR07249F.

(136) Hine, J.; Sinha, A. Catalysis of .Alpha.-Hydrogen Exchange. Part 24. Bifunctional Catalysis of the Dedeuteration of Methoxyacetone-1,1,3,3,3-D5. *The Journal of Organic Chemistry* 1984. https://doi.org/10.1021/jo00186a021.

(137) Rodrigo, D.; Tittl, A.; Limaj, O.; Abajo, F. J. G. de; Pruneri, V.; Altug, H. Double-Layer Graphene for Enhanced Tunable Infrared Plasmonics. *Light: Science & Applications* 2017, *6* (6), e16277. https://doi.org/10.1038/lsa.2016.277.

(138) Mumma, S. a. Transient Occupancy Ventilation By Monitoring CO2. *IAQ Applications* 2004, *5* (1), 21–23.

(139) Jiang, L.; Gao, L. Carbon Nanotubes-Magnetite Nanocomposites from Solvothermal Processes: Formation, Characterization, and Enhanced Electrical Properties. *Chemistry of Materials* 2003. https://doi.org/10.1021/cm030007q.

(140) Zhang, S.; Kang, P.; Ubnoske, S.; Brennaman, M. K.; Song, N.; House, R. L.; Glass, J. T.; Meyer, T. J. Polyethylenimine-Enhanced Electrocatalytic Reduction of CO2 to Formate at Nitrogen-Doped Carbon Nanomaterials. *J Am Chem Soc* 2014. https://doi.org/10.1021/ja5031529.

(141) Ma, W.; Alonso-González, P.; Li, S.; Nikitin, A. Y.; Yuan, J.; Martín-Sánchez, J.; Taboada-Gutiérrez, J.; Amenabar, I.; Li, P.; Vélez, S.; Tollan, C.; Dai, Z.; Zhang, Y.; Sriram, S.; Kalantar-Zadeh, K.; Lee, S. T.; Hillenbrand, R.; Bao, Q. In-Plane Anisotropic and Ultra-Low-Loss Polaritons in a Natural van Der Waals Crystal. *Nature* 2018, *562* (7728). https://doi.org/10.1038/s41586-018-0618-9.

(142) Taboada-Gutiérrez, J.; Álvarez-Pérez, G.; Duan, J.; Ma, W.; Crowley, K.; Prieto, I.; Bylinkin, A.; Autore, M.; Volkova, H.; Kimura, K.; Kimura, T.; Berger, M. H.; Li, S.; Bao, Q.; Gao, X. P. A.; Errea, I.; Nikitin, A. Y.; Hillenbrand, R.; Martín-Sánchez, J.; Alonso-González, P. Broad Spectral Tuning of Ultra-Low-Loss Polaritons in a van Der Waals Crystal by Intercalation. *Nature Materials* 2020, *19* (9). https://doi.org/10.1038/s41563-020-0665-0.

(143) Li, P.; Dolado, I.; Alfaro-Mozaz, F. J.; Nikitin, A. Y.; Casanova, F.; Hueso, L. E.; Vélez, S.; Hillenbrand, R. Optical Nanoimaging of Hyperbolic Surface Polaritons at the Edges of van Der Waals Materials. *Nano Letters* 2017, *17* (1). https://doi.org/10.1021/acs.nanolett.6b03920.

(144) Pitarma, R.; Marques, G.; Ferreira, B. R. Monitoring Indoor Air Quality for Enhanced Occupational Health. *Journal of Medical Systems* 2017. https://doi.org/10.1007/s10916-016-0667-2.

(145) Liu, S.; He, R.; Xue, L.; Li, J.; Liu, B.; Edgar, J. H. Single Crystal Growth of Millimeter-Sized Monoisotopic Hexagonal Boron Nitride. *Chemistry of Materials* 2018, *30* (18). https://doi.org/10.1021/acs.chemmater.8b02589.

(146) Nong, J.; Tang, L.; Lan, G.; Luo, P.; Li, Z.; Huang, D.; Yi, J.; Shi, H.; Wei, W. Enhanced Graphene Plasmonic Mode Energy for Highly Sensitive Molecular Fingerprint Retrieval. *Laser & Photonics Reviews* 2021, *15* (1), 2000300. https://doi.org/10.1002/lpor.202000300.

(147) Zhu, Y.; Li, Z.; Hao, Z.; DiMarco, C.; Maturavongsadit, P.; Hao, Y.; Lu, M.; Stein, A.; Wang, Q.; Hone, J.; Yu, N.; Lin, Q. Optical Conductivity-Based Ultrasensitive Mid-Infrared Biosensing on a Hybrid Metasurface. *Light: Science & Applications* 2018, *7* (1), 67. https://doi.org/10.1038/s41377-018-0066-1.

(148) Kim, S.; Jang, M. S.; Brar, V. W.; Mauser, K. W.; Kim, L.; Atwater, H. A. Electronically Tunable Perfect Absorption in Graphene. *Nano Letters* 2018, *18* (2). https://doi.org/10.1021/acs.nanolett.7b04393.

(149) Taraszka, K. S.; Chen, E.; Metzger, T.; Chance, M. R. Identification of Structural Markers for Vitamin B12 and Other Corrinoid Derivatives in Solution Using FTIR Spectroscopy. *Biochemistry* 1991, *30* (5), 1222–1227. https://doi.org/10.1021/bi00219a009.

(150) Gharagozlou, M.; Naghibi, S. Sensitization of ZnO Nanoparticle by Vitamin B 12 : Investigation of Microstructure, FTIR and Optical Properties. *Materials Research Bulletin* 2016, *84*, 71–78. https://doi.org/10.1016/j.materresbull.2016.07.029.

(151) Mishyn, V.; Hugo, A.; Rodrigues, T.; Aspermair, P.; Happy, H.; Marques, L.; Hurot, C.; Othmen, R.; Bouchiat, V.; Boukherroub, R.; Knoll, W.; Szunerits, S. The Holy Grail of Pyrene-Based Surface Ligands on the Sensitivity of Graphene-Based Field Effect Transistors. *Sensors & Diagnostics* 2022, *1* (2), 235–244. https://doi.org/10.1039/D1SD00036E.

(152) Zhang, K.; Zhang, L.; Yap, F. L.; Song, P.; Qiu, C.-W.; Loh, K. P. Large-Area Graphene Nanodot Array for Plasmon-Enhanced Infrared Spectroscopy. *Small* 2016, *12* (10), 1302–1308. https://doi.org/10.1002/smll.201503016.

(153) Kumar, D.; Sharma, R. C. Advances in Conductive Polymers. *European Polymer Journal*. 1998. https://doi.org/10.1016/S0014-3057(97)00204-8.

(154) Liu, H.; You, C. Y.; Li, J.; Galligan, P. R.; You, J.; Liu, Z.; Cai, Y.; Luo, Z. Synthesis of Hexagonal Boron Nitrides by Chemical Vapor Deposition and Their Use as Single Photon Emitters. *Nano Materials Science* 2021, *3* (3), 291–312. https://doi.org/10.1016/j.nanoms.2021.03.002.

(155) Wang, P.; Lee, W.; Corbett, J. P.; Koll, W. H.; Vu, N. M.; Laleyan, D. A.; Wen, Q.; Wu, Y.; Pandey, A.; Gim, J.; Wang, D.; Qiu, D. Y.; Hovden, R.; Kira, M.; Heron, J. T.; Gupta, J. A.; Kioupakis, E.; Mi, Z. Scalable Synthesis of Monolayer Hexagonal Boron Nitride on Graphene with Giant Bandgap Renormalization. *Advanced Materials* 2022, 2201387. https://doi.org/10.1002/adma.202201387.

(156) Su, Z.; Sun, X.; Liu, X.; Zhang, J.; Sun, L.; Zhang, X.; Liu, Z.; Yu, F.; Li, Y.; Cheng, X.; Ding, Y.; Zhao, X. A Strategy To Prepare High-Quality Monocrystalline Graphene: Inducing Graphene Growth with Seeding Chemical Vapor Deposition and Its Mechanism. *ACS Applied Materials & Interfaces* 2020, *12* (1), 1306–1314. https://doi.org/10.1021/acsami.9b16549.